January 2015

Collective Phenomena in Active Systems

Xingbo Yang
Syracuse University

Abstract

This dissertation investigates collective phenomena in active systems of biological relavance across length scales, ranging from intracellular actin systems to bird flocks. The study has been conducted via theoretical modeling and computer simulations using tools from soft condensed matter physics and non-equilibrium statistical mechanics. The work has been organized into two parts through five chapters. In part one (chapter 2 to 3), continuum theories have been utilized to study pattern formation in bacteria suspensions, actomyosin systems and bird flocks, whose dynamics is described generically within the framework of polar active fluids. The continuum field equations have been written down phenomenogically and derived rigorously through explicit coarse-graining of corresponding microscopic equations of motion. We have investigated the effects of alignment interaction, active motility, non-conserved density, and rotational inertia on pattern formation in active systems. In part two (chapter 4 to 5), computer simulations have been performed to study the self-organization and mechanical properties of dense active systems. A minimal self-propelled particle (SPP) model has been utilized to understand the aggregation and segregation of active systems under confinement (Chapter 4), where an active pressure has been defined for the first time to characterize the mechanical state of the active system. The same model is utilized in Chapter 5 to understand the self-assembly of passive particles in an active bath.

Collective Phenomena in Active Systems

by

Xingbo Yang

B.A., Fudan University, 2010

Dissertation

Submitted in partial fulfillment of the requirements for the degree of
Doctor of Philosophy in Physics

in the graduate school of Syracuse University

August 2015

Acknowledgements

My most sincere gratitude goes to my research advisor Prof. Cristina Marchetti, who opened the door of soft condensed matter physics for me. I cherish the mentorship from all the professors in Syracuse University with whom I have studied and worked, and my special thanks goes to Prof. Lisa Manning, who has contributed significantly to Chapter 4. I am indebted to Prof. Davide Marenduzzo from the University of Edinburgh for his valuable contribution to Chapter 2 and for allowing me to use the PDE solver he developed. I also owe my gratitude to Yaouen Fily, whose MD simulation code led to the work in Chapter 4, Adam Patch and David Yllanes, whose work enriches Chapter 4. I enjoyed the collaboration with Dapeng (Max) Bi on the study of the mechanics of confluent tissue, which is an ongoing project not included in this dissertation. Finally, I would like to thank all the members of my defense committee for devoting their valuable time to read this manuscript and for their support at this special time of my academic career.

To my mother and father

Contents

List of Figures

Chapter 1

Introduction

1.1 Scope

Active systems, composed of self-driven units each capable of converting stored or ambient free energy into systematic motion [14], are highly non-equilibrium systems that display a zoo of novel behaviors as compared to their equilibrium counterparts. Physical and biological realizations span length scales orders of magnitude apart, from subcellular systems to animal flocks. Although the individual units can be very different, active systems share generic collective behaviors that often transcend the physical or biological details, with dynamics governed by conservation laws, symmetry, activity and nature of interactions. This potential universality provides opportunities for physicists to be involved in the study of living systems using quantitative tools developed in the traditional fields of condensed matter physics and non-equilibrium statistical mechanics.

The perspective that active systems can be treated as pieces of material yields the emergence of the subfield of active matter [15]. Active systems may behave as fluids, solids or viscoelastic material with both liquid-like and solid-like behaviors. The diversity in the mechanical properties and relaxation time scales in active matter usually blurs the boundary between states of matter in a traditional sense, and the treatment depends very much on the context. For example, actomysin systems can be treated as elastic solids and modeled as cross-linked active gels when describing cellular contraction [16], but as liquid suspensions when modeling treadmilling that regulates cellular motility [9, 17]. Phase transitions from one material state to another also occur in active matter, such as glass transition in confluent cell monolayers [18].

While the endeavor to approach biology from a physics perspective can be a daunting one given the complexity of living systems with many experimentally uncontrollable degrees of freedom, the scope of the problem can be defined in such a way that only a

minimal number of ingredients is required to capture the essential features at a collective level. The problems amenable to physical treatment are usually of a dynamical and mechanical nature, involving the cooperative motion of interacting active units driven by the interplay of activity, dissipation and noise. This is a paradigm familiar to condensed matter physicists, for example in the context of diffusion and phase transition in thermal systems. Similar principles can be implemented in the study of active systems, but great care should be taken given the fact that the highly non-equilibrium active systems can no longer be characterized by a thermodynamic temperature. As a result, activity, dissipation and noise are generally independent variables that keep the active system out of equilibrium, or equivalently, break detailed balance and violate the fluctuation-dissipation theorem. Thus we cannot rely on the general framework provided by equilibrium thermodynamics developed over the course of the past two centuries. A new framework is needed where we attempt to classify active systems on the basis of activity, symmetry, respected conservation laws and nature of interactions.

I hereby present five non-exclusive and non-exhaustive classifications of active systems on the basis of the following properties:

i) The nature of activity. Active processes are cyclical ones that convert chemical energy into mechanical work generating forces on the environment. Such forces can be classified as contractile as in epithelium cell monolayers [19] and extensile as in motor-driven microtubule bundles [20, 21]. When the environment is inert providing just friction, we can model the active components as self-propelled entities, where the propulsive force is effectively a monopole. Examples include bird flocks [1, 2, 22–25], migrating cell layers [12, 26, 27], bacterial swarms [5, 6, 17] and treadmilling cytoskeletal filaments [9, 17, 28, 29]. Growth is another form of activity which not only yields active forces, but also breaks the conservation of number density, important for bacterial colony pattern formation and *Drosophila melanogaster* (fruit fly) wing development [30], for example.

ii) The presence/absence of momentum conservation. Active systems can be divided into momentum-conserving "wet system" and momentum-dissipating "dry system". Examples of the former are active suspensions [31], such as swimming bacteria [3, 32, 33] and cytoskeletal extract in bulk suspensions [20, 34], where viscous flow damps the relative motion of neighboring regions, and the description of the dynamics must include the total conserved momentum of the suspension. "Dry systems" are those that can be described as collections of self-propelled particles in an inert medium that only provides friction, such as bacteria gliding on a substrate [5, 6], swimming between two closely spaced walls, or moving through a porous medium. In all these cases, dissipation is dominated by a drag force and one can consider only the dynamics of the active units,

whose momentum is not conserved [15]. Examples include animal flocks [22], migrating cell layers [12] and vibrated granular particles [35].

iii) Symmetry. We can categorize active systems into isotropic, polar and nematic kinds based on the shape of the particles and the symmetry of the interactions. Isotropic particles (disks in 2D or spheres in 3D) with isotropic interactions do not exhibit orientational order on macroscopic scales, but still show a host of novel non-equilibrium phenomena due to activity [10, 36, 37]. Spherical self-propelled particles with repulsive interaction are among one of the most studied model systems owing to their simplicity in capturing collective behaviors such as clustering in bacterial colonies [13, 38], wall accumulation of swimming bacteria [39], and collective cell migration [26]. Elongated active units can self-organize into phases of orientational order with either polar or nematic broken symmetry. The polar order is described by a vector order parameter $\boldsymbol{p}$, known as the polarization, while the nematic order is described by a tensor order parameter, $\boldsymbol{Q}$, known as the alignment tensor. They are related to a unit vector along the longer axis of the active unit $\hat{n}_i$ by $\boldsymbol{p} = \frac{1}{N}\sum_i \hat{n}_i$ and $Q_{\alpha\beta} = \frac{1}{N}\sum_i \left(\hat{n}_{i\alpha}\hat{n}_{j\beta} - \frac{1}{2}\delta_{\alpha\beta}\right)$ in 2D. Active units themselves may be polar, i.e., have distinct head and tail, such as bacteria [3], or apolar, such as melanocytes and vibrated granular rods [40]. Polar active particles in the presence of polar interactions that tend to align themselves head-to-head and tail-to-tail can organize in a polar phase, characterized by non-zero global mean motion. Examples are animal flocks [2] and bacterial swarms [6]. Nematic phase can be obtained in two ways, either in systems where polar self-propelled objects are parallel but with random head-tail orientations due to apolar interaction, such as self-propelled rods [41], or in systems where the self-propelled particles are themselves head-tail symmetric, such as vibrated granular rods [40] and fibroblast cell monolayer [42]. A particular case is myxobacteria *Myxococcus xanthus* gliding on a substrate with reversal dynamics, i.e. they self-propel in a polar manner before reverse their polarity and move backwards periodically, therefore display nematic order over large time scales [43, 44].

iv) The nature of the interactions. These can be direct inter-particle interactions and medium-mediated interactions. Additionally, direct interactions may be short or long-ranged. Medium-mediated interactions are generally long-ranged, but may be screened by confinement or other effects. Birds in a flock, are an example of a system that can be modeled with short-range interactions, where each bird tends to align only with its immediate neighbors, yet displays large scale flocking behavior [2]. Interactions can become long-range through medium-mediated hydrodynamic effects, as in the case of light-activated colloidal particles [11] or electrically powered roller colloids in solutions [45].

v) Coupling to external fields. Active systems can be coupled to external fields through sensory mechanisms, many of which have been termed according to the nature of the

fields the active units respond to. Among the most well-known is chemotaxis, the movement of an organism, such as bacteria, in response to chemical gradient in the environment [46]. A much more recent discovery is durotaxis, a form of cell migration guided by rigidity gradients in the substrate or extracellular matrix [47, 48]. Beyond migratory responses, in developmental biology, cell differentiation depends heavily on the signaling of morphogens, whose concentration affects the morphogenesis in tissues by triggering coordinated cell differentiation [49, 50].

Given the framework, I now ask the question: *are there generic laws governing the collective dynamics of seemingly different active systems arising from the interplay among activity, dissipation, and noise?* To make progress towards answering this question in this dissertation, I propose minimal models to study pattern formation and mechanics of self-propelled units in a dissipative medium with distinct symmetries and interactions. The model systems considered have specific relevance to actomyosin networks, bacterial suspensions, epithelium cell layers and animal flocks. The study is performed in two complementary ways: analytical and numerical exploration of continuum hydrodynamic theories and computer simulations based on microscopic equations of motion. A bridge connecting the two is constructed systematically as well.

1.2 Pattern formation in active systems

One of the prominent features of active systems is the emergence of non-equilibrium dynamical patterns as a result of the self-organization among interacting active constituents. Examples are abundant in living systems and range from subcellular process, such as actomyosin waves in the cell interior, to coordinated animal behaviors like the flocking of birds. The concept of pattern formation is certainly not exclusive to active systems, but a general concept concerning the development of structure in dynamical systems [51]. The science of pattern formation aims to establish general principles governing the formation of similar patterns observed in nature as a result of self-organization. Pattern formation may arise either from equilibrium symmetry breaking or from a non-equilibrium loss of stability that replaces a disordered or homogeneous state with a structured one. An example of the former is the formation of snowflakes upon the breaking of continuous translational symmetry going from a liquid state to a crystalline state. An example of the latter is the Turing instability in reaction-diffusion systems, where a homogeneous steady state is replaced by a temporally oscillating or spatially periodic state that results from the unstable growth of fluctuations, a mechanism with potential general applicabilities to a wide range of dynamical problems from non-equilibrium chemical reactions to morphogenesis in embryonic development [52].

Pattern formation in biological systems is a collective phenomenon that usually serves a functional purpose that reflects living organisms' adaptivity to a dynamical environment. Flocks of starlings or pilchard schools are robust structures that serve a defensive purpose against predators [2]. Colonies of bacteria such as, *Escherichia coli* and *Myxococcus xanthus*, adjust their morphologies to adapt to the chemical or mechanical environment [5, 6]. Slime molds, such as *Dictyostelium discoideum*, alter their life cycles switching from vegetative state in the abundance of nutrients to social aggregates or fruiting bodies in the deficiency of food. At a subcellular level, the emergence of actin waves in the same organism is responsible for triggering the mobilization of vegetative cells [28].

The detailed biological mechanisms that drive each of these phenomena are certainly different. However, the general principles we are after require a minimal modeling that captures the essential features based on their dynamical nature as outlined in the framework introduced in the previous section. Within this scope, we model the relevant active systems as composed of self-propelled objects with distinct interactions, symmetries and conservation laws respecting underlying biological features, and describe the dynamics in terms of microscopic equations of motion as well as macroscopic hydrodynamic field theories. Concretely, flocking of birds or treadmilling of actin filaments have been interpreted as a consequence of the interplay between local alignment interactions and self-propulsion of polar active units, while the polymerization of actin filaments and bacteria proliferation have been modeled as logistic effects that break the conservation of density, resembling a reaction effect in chemical systems.

Efforts to model pattern formation in biological systems based on these principles have seen success in the aforementioned biological systems, but a generic framework to unify various descriptions and to identify minimal ingredients is still lacking [9, 13, 53]. A challenging and open question is: *how does activity, generated at an individual level, regulate the dynamical pattern formation in living systems?*

Below, I survey pattern formation in three biological systems of vastly different length scales to set up the stage.

1.2.1 Bird Flock

Groups of starlings self-organize into coherent flocking patterns involving hundreds to thousands of individuals (Fig.1.1). Similar phenomena are shoaling of fish, swarming of insects, and herding of land animals, collective phenomena related to feeding, defense and migration. While the biological origin and purpose of collective animal behavior are of primary interest to ethologists, the polarized pattern itself reminds physicists of

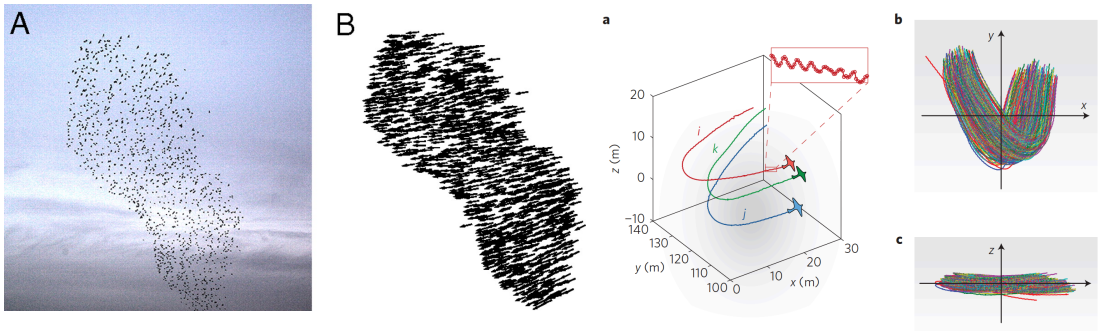

FIGURE 1.1: Left: A. Snapshot from a flocking of 1246 starlings. B. Normalized instantaneous velocity vectors of all the individuals in the snapshot. [1] Right: a. reconstructed 3D trajectories of three birds belonging to a flock performing a collective turn. b, c, trajectories of N=176 birds in a flock. Each trajectory lies approximately on a plane. [2]

condensed matter systems such as magnets, where spins line up to generate magnetic fields. In flocking models, magnetic spins are replaced by "flying spins", each represented by a velocity vector. Both physicists and computer graphic scientists [54] have come up with models for flocking, among which the most well-known is the Vicsek model [22]. It represents each bird as a self-propelled point particle with a constant speed that tries to align its velocity vector with the average velocity set by its neighbors but makes errors modeled as a white noise. The equations of motion for a single particle are given as follows:

$$\boldsymbol{x}_i(t+1) = \boldsymbol{x}_i(t) + \boldsymbol{v}_i(t)\Delta t, \quad \theta_i(t+1) = < \theta(t) >_r + \Delta\theta_i, \tag{1.1}$$

where $\boldsymbol{x}_i(t)$, $\boldsymbol{v}_i(t)$ and $\theta_i(t)$ denote the position, velocity and orientation of the ith particle at time t, respectively. $< \theta(t) >_r$ denotes the average direction of the velocities of the particles (including particle i) that are within a circle of radius r surrounding the given particle. $\Delta\theta_i$ is a random number chosen from a uniform probability distribution within the interval $[-\eta/2, \eta/2]$. The tuning parameters in this model are the number density and the noise strength η. Computer simulations reveal a phase transition upon the increase of number density or decrease of noise from a disordered state to a flocking state with a non-zero value of the average particle velocity. This microscopic model has inspired the development of a continuum theory treating the flock as an active fluid described by the dynamical fields of density and velocity, known as the Toner-Tu model [23]. This model incorporates local alignment interactions as a non-linear friction in the velocity dynamics resembling that of the Landau theory dealing with continuous phase transition in condensed matter systems. It also resembles the Navier-Stokes equations of fluid dynamics, but with extra non-linear terms due to the breaking of Galilean invariance. In the absence of activity, in this case the self-propulsion, the model reduces to the classical XY model in magnetism. The presence of activity has been shown

analytically by Toner and Tu to be responsible for the stable spontaneous symmetry broken state even in two dimensions, which is forbidden in the equilibrium XY model due to spin wave fluctuations. This feature allows the model to describe a large class of non-equilibrium systems, not limited to bird flocks, but including systems with similar large-scale dynamics such as treadmilling actomyosin network [29] and motile colloids [45]. Variants of Vicsek and Toner-Tu models have been proposed to accommodate specific features in different active systems, including hydrodynamic interaction [45] and motility suppression due to crowding [25].

It was not until recently that field experiments have been performed on flocks of starlings [2]. Three dimensional particle tracking has made quantitative analysis of the flock dynamics possible. New models have been proposed to accommodate observed features in experiments, among which are the maximum entropy model [1] that captures the velocity correlation in agreement with the experiments and the inertial spin model that captures the collective turning behavior observed in natural flocks (Fig.1.1) [55]. The latter is a significant update of the Vicsek model that incorporates inertia in the dynamics of spin angular momentum, which is neglected in the Vicsek model. This inertial effect leads to the propagation of turning information via spin-wave-like excitations throughout the flock to generate collective turning behaviors in defense of predators.

The microscopic "inertial spin" model calls for a corresponding continuum theory analog to the Toner-Tu model. I have taken up the task to construct such a continuum theory by explicitly coarse-graining the microscopic model to yield field equations characterizing the dynamics of spin angular momentum in addition to density and translational velocity. The explicit coarse-graining yields a limited number of parameters in the continuum equations and opens up doors for quantitative analytical analysis. Open questions emerge following the development of new models: *How is the stability of the flock determined by the interplay between inertia, activity and alignment interaction? What are the characteristics of the spin wave in the presence of an underlined broken symmetry, activity and density/velocity fluctuations? What is the difference between a turning flock and a system of equilibrium rotors?*

1.2.2 Bacterial swarm

Bacteria sense their environment through chemical or mechanical cues and form intriguing patterns (Fig.1.3). Individual bacteria differ in morphology, but many share similar propulsion mechanisms in viscous fluids (Fig. 1.2). The run-and-tumble motion, where ballistic runs are segmented by tumbles to result in a long-time diffusive motion, is exploited by many flagellated bacteria to explore the environment. Bacteria such as *E.*

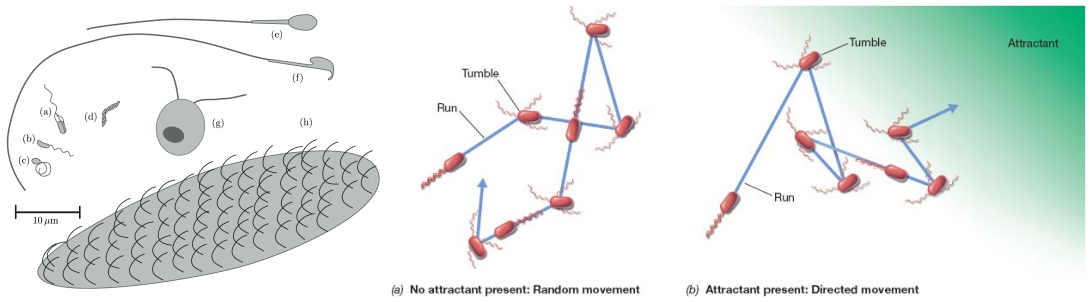

FIGURE 1.2: Left: Sketches of microscopic swimmers, to scale. (a) *E. coli*. (b) *C. crescentus*. (c) *R. sphaeroides*, with flagellar filament in the coiled state. (d) *Spiroplasma*, with a single kink separating regions of right-handed and left-handed coiling. (e) *Human spermatozoon*. (f) *Mouse spermatozoon*. (g) *Chlamydomonas*. (h) A smallish *Paramecium*. [3] Right: Run-and-tumble motion of flagellated *Escherichia coli*. (a) random runs segmented by tumbles in the absence of chemical attractant. (b) biased runs up the gradient of the attractant through chemotaxis. [4].

coli can sense the gradient of chemical attractant through the transmembrane chemical receptors and perform a biased run-and-tumble motion up such a gradient, a mechanism known as chemotaxis (Fig. 1.2) [46].

Chemotaxis has been proposed as the mechanism responsible for pattern formation observed in a variety of bacterial systems, including *E. coli* and *S. typhimurium* in soft agar (Fig.1.3) [5, 6]. In the experiments, the agar is prepared with carbon source, which serves as nutrients for the bacteria, before the inoculation of bacteria suspensions. In the case of *E. coli* (top two rows in Fig. 1.3), a swarming ring propagates from the inoculated spot radially outward upon the consumption of the nutrients and leaves dense bacteria aggregates along its wake. Remarkably, the aggregates form stable lattice patterns whose morphology depend on the concentration of carbon source in the agar. In the case of *S. typhimurium* (bottom row in Fig. 1.3), the bacteria first spread radially and form an unstructured lawn, with the density decreases away from the center. After 40 hours of growth, rings with dense concentration of bacteria start to emerge from the center and spread sequentially outward at a fixed distance from one another. At lower concentration of carbon source, each ring becomes perforated and breaks into dense spots. At larger concentration, the ring is intact and stable. Bacteria tracking reveals that cells are highly motile in the unstructured lawn and in newly formed rings, but nonmotile in older rings. On the other hand, if the bacteria is grown in a liquid medium, randomly distributed dense aggregates emerge from a homogeneous bacteria suspension.

In both cases, pattern formation can be suppressed by the addition of the chemoattractant aspartate that saturates the bacteria transmembrane receptors, thus suppressing chemotaxis. Both *E. coli* and *S. typhimurium* are known to secrete chemoattractant, therefore respond to the attractant gradients generated by themselves. This is the

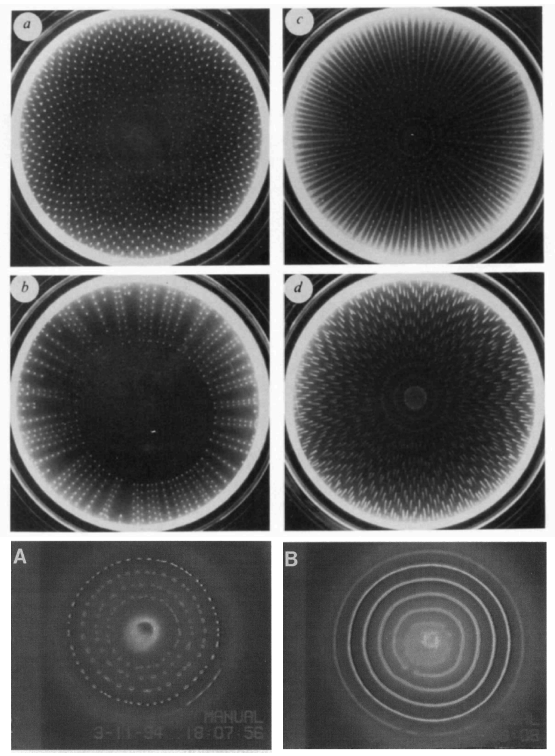

FIGURE 1.3: Top two rows: Stationary patterns formed by *E. coli* growing in semi-solid agar with different concentrations of carbon source. Bright spots indicate higher concentration of bacteria aggregates a. Sunflower-like arrays of spots. b. Radial arrays of spots. c. Radial arrays of spots and stripes. d. Spots with radial tails arrayed in chevrons. [5] Bottom row: Stationary patterns formed by *Salmonella typhimurium* in soft agar with different concentrations of carbon source, in this case succinate. A. perforated rings at lower concentration of succinate. B. stable rings at higher concentration of succinate. [6]

mechanism proposed to explain the geometrical patterns observed in both cases: density fluctuations in the bacteria colony is amplified by the chemotactic response where dense aggregates produce more attractants than depleted regions. This mechanism has been modeled via a number of coupled reaction-diffusion equations describing the interplay between cell concentration, carbon source and chemoattractants to determine the pattern [53, 56].

The multi-component reaction-diffusion models are capable of reproducing the observed patterns, but contain many fitting parameters that are model-dependent. In recent years, generic models with minimal ingredients have been proposed by Cates et al. [13]. Under this framework, a single component theory with only the dynamics of cell concentration is sufficient to capture the chemotactic patterns formed by *S. typhimurium*. The model involves a density-dependent motility that captures the effect of chemotaxis, a logistic growth/death term that breaks the conservation of density and an effective surface tension that stabilizes the aggregates. The density-dependent motility induces phase separation through spinodal decomposition that is arrested by the growth/death

of the bacteria, which sets a characteristic length scale for the lattice patterns not unlike the one formed by *S. typhimurium* [13].

While the model is successful in reproducing density patterns in certain bacteria system such as *S. typhimurium*, it fails to account for more complex patterns such as those observed in *E. coli*. A short-coming of the model is that it ignores the internal degrees of freedom of the bacteria, such as the polarization. Many bacteria, including *E. coli* and *S. typhimurium*, have a rod-like shape, which induces polar structures through quorum sensing or static effects in the swarm that favors the collective motion. Given the large density of the bacteria aggregates, it is not unreasonable to assume an important role of the polarization dynamics. Toner-Tu model is an example that couples density to polarization, but assumes a constant motility and neglect proliferation. In bacteria colonies, cell motility can be strongly suppressed either by steric effects at high density or by chemotactic mechanisms, and cell division/death is important within the time scale of pattern formation. To study the interplay of all these factors, we have constructed a minimal variant of Toner-Tu model with a density-dependent velocity and a logistic growth/death term. The resulting equations not only reproduce the *S. typhimurium* patterns, but predict non-trivial internal structures within the aggregates as a result of the polarization dynamics. While the model is powerful in generating rich patterns, more work is needed for a quantitative comparison with the patterns observed in situations where the alignment interaction is significant. One of the open questions for future exploration is: *can we harness the simplicity and power of the model to account for more complicated patterns formed, for example, by E. coli and P. Mirabilis and make quantitatively testable results?*

1.2.3 Actomyosin wave

The actomyosin network is a dynamic protein-based structure made of actin filaments, motor proteins and branching/binding proteins that constantly undergoes assembly, reassembly and reorganization. It is a key component of the cytoskeleton of eukaryotic cells, where it facilitates the transport of cargo, generates forces and provides structural support for the cell. The locomotion of many cells is driven by the polymerization of actin filaments that generate protrusive forces on the plasma membrane to form lamellipodia that anchor to the substrate through focal adhesions to pull the cell forward (Fig. 1.4). This process requires the formation of branched actin filament networks near the cell membrane as initialized by membrane-bounded proteins WASP/WAVE. Actin filaments have a polar structure characterized by a pointed (-) and a barbed end (+). The latter is oriented towards the cell membrane. ATP hydrolysis elongates actin filament in the direction of the barbed end by adding actin monomers, therefore generate protrusive

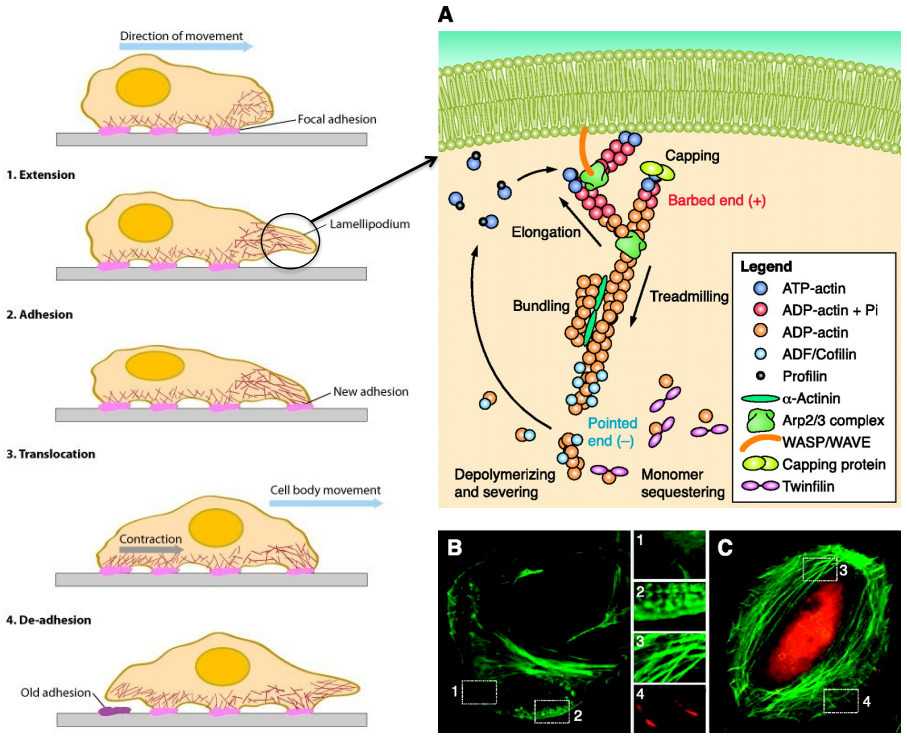

FIGURE 1.4: Left: Cell spreading and movement through protrusion of the lamellipodium driven by the polymerization of actin filaments and subsequent contraction by stress fibers coupled to the substrate through focal adhesions. (reproduced from Ref. [7]) Right: A. Dynamics at the molecular level of actin polymerization in cell motility. The treadmilling and elongation of nucleated actin network induced by actin polymerization generate protrusive forces on the plasma membrane to form lamellipodia. B. motile B16F1 mouse *melanoma* cell stained with fluorescently labeled phalloidin (green) to visualize actin filaments. Filopodia (1) is utilized to probe the environment and Lamellipodium (2) to generate locomotion. C: Fluorescently labeled stationary human *osteosarcoma* (U2OS) cell with stress fibers (3) in green and focal adhesions in red (4). [8]

force on the membrane to form lamellipodia. Branching proteins Arp2/3 complex and binding proteins α-Actinin add to the integrity of filament bundles. The polymerization also promotes treadmilling, an effective propulsion of actin filaments (Fig. 1.4).

Experiments with cellular slime molds *Dictyostelium Discoideum* have shown that the onset of cell motility is associated with propagating actin waves generated by actin polymerization [28]. In the experiments, the substrate-attached cells are rendered immobile by the addition of latrunculin that depolymerizes F-actin. Upon the reduction of latrunculin concentration, the polymerization of F-actin is restored in the cortex signaled by the formation of stationary actin spots. The spots proliferate and soon become motile while merging into spiral waves that propagate towards the cell periphery. When the actin wave hits the boundary, it expands the cell border and mobilizes the cell (Fig. 1.5).

This highly dynamical phenomenon has previously been modeled, again, via reaction-diffusion equations with activator and inhibitor playing the role of latrunculin that

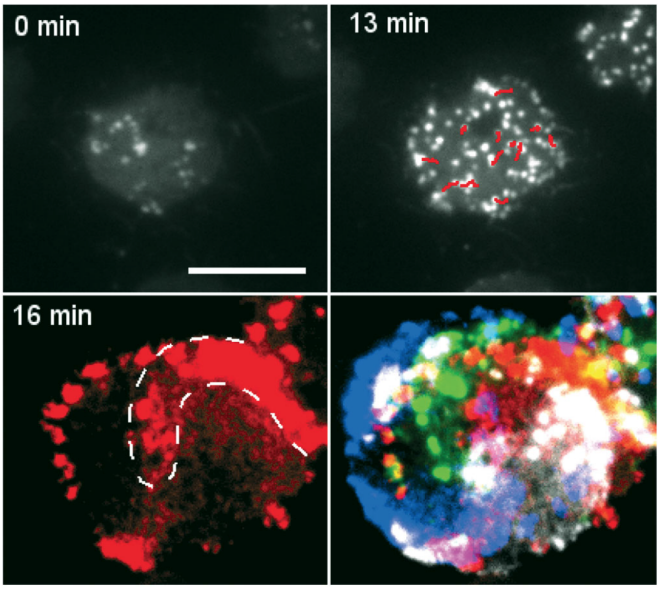

FIGURE 1.5: Dynamical actin structures during the recovery of actin polymerization in the substrate-attached cortex of a *Dictyostelium* cell. Stationary actin spots emerge and proliferate to become mobile before a prominent spiral wave appears after 16 minutes of the recovery of polymerization. The counterclockwise-rotating spiral wave propagates towards the cell periphery to expand the cell border by producing protrusions that mobilize the cell. [9]

regulates the polymerization of actin filaments [9]. In chapter 2, I show that this emergent phenomenon is also captured by the physical model introduced in the previous section. Here, the density corresponds to the concentration of actin filaments, and the polarization dynamics naturally captures the treadmilling. The polymerization of actin is incorporated as a logistic term and the combined effect from the regulation of membrane-bounded protein and latrunculin is incorporated into the density-dependent motility. Given that the polymerization timescale is comparable with the alignment induced by excluded volume interaction, the dynamics of the polarization is strongly coupled to that of the concentration, which leads to the formation of dynamical wave patterns not unlike the ones observed experimentally.

Given the qualitative success of the model, we are left with the challenge to make quantitative predictions regarding the complex pattern formation. Our model is potentially capable to extract characteristic scales and periodicity of the pattern that are susceptible to experimental verification.

1.3 Mechanics of dense active systems

Newtonian mechanics and Brownian dynamics are powerful tools in microscopic modeling provided that stochastic effects are carefully considered. In this language, Langevin

equations serve as the foundation for dynamical simulations of stochastic systems [57]. A simple example is the overdamped motion of a thermal Brownian particle described by the following Langevin equation:

$$\frac{dx}{dt} = \eta(t), \tag{1.2}$$

where x is the position of the particle and $\eta(t)$ is the thermal noise with $< \eta(t) >= 0$ and $< \eta(t)\eta(t') >= 2D\delta(t - t')$. The mean-squared displacement (MSD) of the particle is given by $< \Delta x(t)^2 >= 2Dt$, where D is the translational diffusion coefficient, related to the frictional coefficient ξ through temperature T by the fluctuation-dissipation theorem as $D = k_b T/\xi$. This is the foundation of equilibrium Brownian dynamics.

The athermal nature of active systems rule out the applicability of the fluctuation-dissipation theorem. Alternatively, an individual-based energy source, damping, and an athermal noise have to be incorporated independently for active systems. These non-equilibrium features have a simple but general representation in the self-propelled particle model (SPP), which proves to be powerful in the study of mechanical properties of dense active systems.

1.3.1 Self-propelled particle model

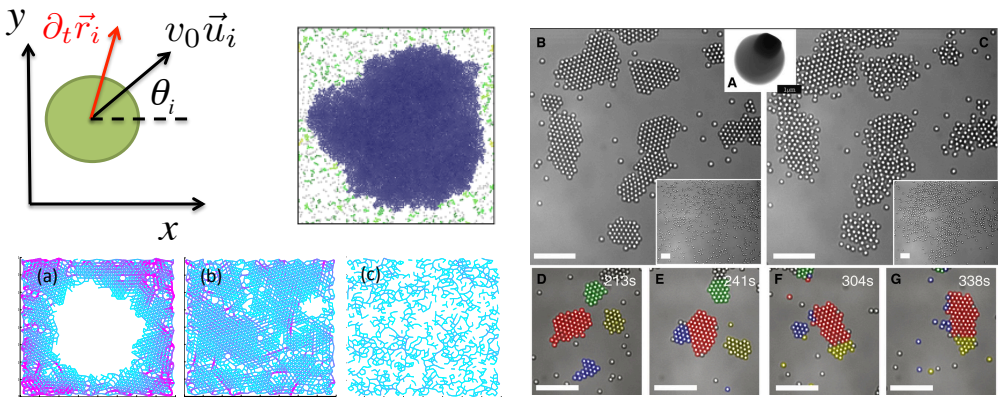

FIGURE 1.6: Top left: model of self-propelled particle (SPP). Top right: phase separation of repulsive SPPs with periodic boundary condition (simulation) [10]. Bottow: force chains of confined SPPs (simulation). (a) wall-aggregated state (b) jammed state (c) gas state. Right: Experiments of light-activated self-propelled colloidal particles with phoretic attraction [11].

The SPP model describes interacting particles with self-propulsion forces along directions independently associated with each particle's orientation. The position and orientation of every particle is subject to athermal noise characterizing the biological or chemical fluctuations. Dissipation with the surrounding medium is incorporated through a frictional drag (Fig.1.6). When the time scales of interest are beyond that of the friction,

we can neglect inertia to simplify the dynamics. This assumption is reasonable over a wide range of active systems with constituents in a viscous environment whose inertial effect is negligible, such as swimming bacteria at low Reynolds number [58] and cells crawling in extracellular matrix [12].

The simplest model of SPP consists of isotropic self-propelled disks (in 2D) or spheres (in 3D) with short-ranged repulsive interaction [10] (Fig.1.6). Their positions and orientations are subject to white Gaussian noise. The equations of motion in 2D are given by

$$\frac{d\boldsymbol{r}_i}{dt} = v_0\boldsymbol{u}_i + \mu\sum_j \boldsymbol{F}_{ij} + \boldsymbol{\eta}_i(t), \quad \frac{d\theta_i}{dt} = \eta_i^r(t), \tag{1.3}$$

where $\boldsymbol{r}_i$ is the position of particle i, v_0 is the constant self-propulsion speed, $\boldsymbol{u}_i$ is the polarization vector for particle i with the orientation denoted by an angle θ_i. $\boldsymbol{F}_{ij}$ is the repulsive force between particle i and j. Finally, $\boldsymbol{\eta}(t)$ and $\eta_i^r(t)$ are translational and rotational noise with zero mean and variance $< \eta(t)_i^\alpha \eta(t')_j^\beta >= 2D\delta_{ij}\delta_{\alpha\beta}\delta(t-t')$, $< \eta_i^r(t)\eta_j^r >= 2D_r\delta_{ij}\delta(t-t')$, respectively. In equilibrium, D_r and D are related by $D_r = D/a^2$, where a is the particle size. In active systems, this is generally not the case as the source of translational and rotational noise may not be the same. In a non-interacting SPP system, the MSD of the self-propelled particle is given by $< [\Delta\boldsymbol{r}(t)]^2 >= 4D_0\left[t + \frac{1}{D_r}(e^{-D_r t}-1)\right]$, where $D_0 = D + \frac{v_0^2}{2D_r}$ is the effective long-time diffusion coefficient. The particle behaves ballistically for $t \ll 1/D_r$ with $< [\Delta\boldsymbol{r}(t)]^2 >= v_0^2t^2$ and diffusively for $t \gg 1/D_r$ with $< [\Delta\boldsymbol{r}(t)]^2 >= 4D_0t$. The crossover time scale is $1/D_r$. The dynamics of a single self-propelled particle can be characterized by a dimensionless Péclet number, defined as $Pe = \frac{v_0}{aD_r}$, which measures the persistence of the particle as compared to its size. With interaction, the dynamics of the system is also controlled by packing fraction $\phi = N\pi a^2/V$. Minimal as it is, the model displays rich collective behaviors reminiscent of those observed in biological and robotic systems. One of the prominent phenomena is the motility induced phase separation (MIPS), where a homogeneous state spontaneously phase separates into a coexistence of a dense liquid phase and a dilute gas phase above a critical packing fraction and Péclet number (Fig.1.6) [10]. This phenomenon is reminiscent of the phase separation in a Van der Waals system, but without any attractive interaction.

An interesting questions therefore arises: *is there a connection between the repulsive SPP system and the attractive thermal Van der Waals system? Is it possible to map an active system to a thermal equilibrium system, if so, under what condition?* If the answer is positive, we will be making significant progress towards understanding the dynamics of highly non-equilibrium systems.

To address this question, I have studied the repulsive SPP system under confinement, an ideal configuration to measure mechanical quantities such as pressure, an important step towards writing down an equation of state, if it exists, for the active system. We were the first to discover the existence of a non-equilibrium pressure in active systems, which we termed the active pressure. Our discovery has sparkled immense interest into the research of mechanical properties of SPP system in the community. Significant progress on the interpretation of the pressure [59, 60], existence of the equation of state [60] and mapping to thermal systems have been made [61, 62].

However, there are still many open questions for future exploration. *What determines the mechanical properties of active systems reflected in the relaxation of the pressure? Can we go beyond pressure and compute the full stress tensor that contains all the mechanical information of the system? If so, what can we learn from it? Can we apply the model to quantitatively describe experimentally accessible systems such as migrating cell layers?*

1.3.2 Mechanics of confluent tissue

Recent *in vitro* experiments have shed light on the mechanics of collective cell migration, a process relevant to many biological processes, including wound healing, cancer metastasis and morphogenesis [12, 26, 27]. Traction Force Microscopy (TFM) is utilized to measure the traction forces cells exert onto the substrate. In this experiment, cells are plated onto a soft substrate in which fluorescent beads have been embedded. By measuring the bead displacements due to the traction forces exerted by the cells on the substrate, and assuming that the substrate is a linear elastic medium, one can calculate the traction forces. An inverse problem is then solved to obtain the intercellular stress (σ) within the tissue from the traction forces ($\boldsymbol{T}$) (Fig. 1.7) using the mechanical relations in 2D

$$h(\partial_x \sigma_{xx} + \partial_y \sigma_{xy}) = T_x \tag{1.4}$$

$$h(\partial_x \sigma_{yx} + \partial_y \sigma_{yy}) = T_y, \tag{1.5}$$

where h is the average height of the cell layer, and the compatibility condition

$$\partial_x^2 \sigma_{yy} + \partial_y^2 \sigma_{xx} - \nu(\partial_x^2 \sigma_{xx} + \partial_y^2 \sigma_{yy}) - 2(1+\nu)\partial_x \partial_y \sigma_{xy} = 0, \tag{1.6}$$

where ν is the poisson ratio. The experimentally observed traction forces arise predominately many cell rows behind the front edge in a migrating cell layer and extend across enormous distances in the bulk through a global tug-of-war [26], which are contrary to the hypothesis that the driving forces are localized in the 'leader cells' at the front edge.

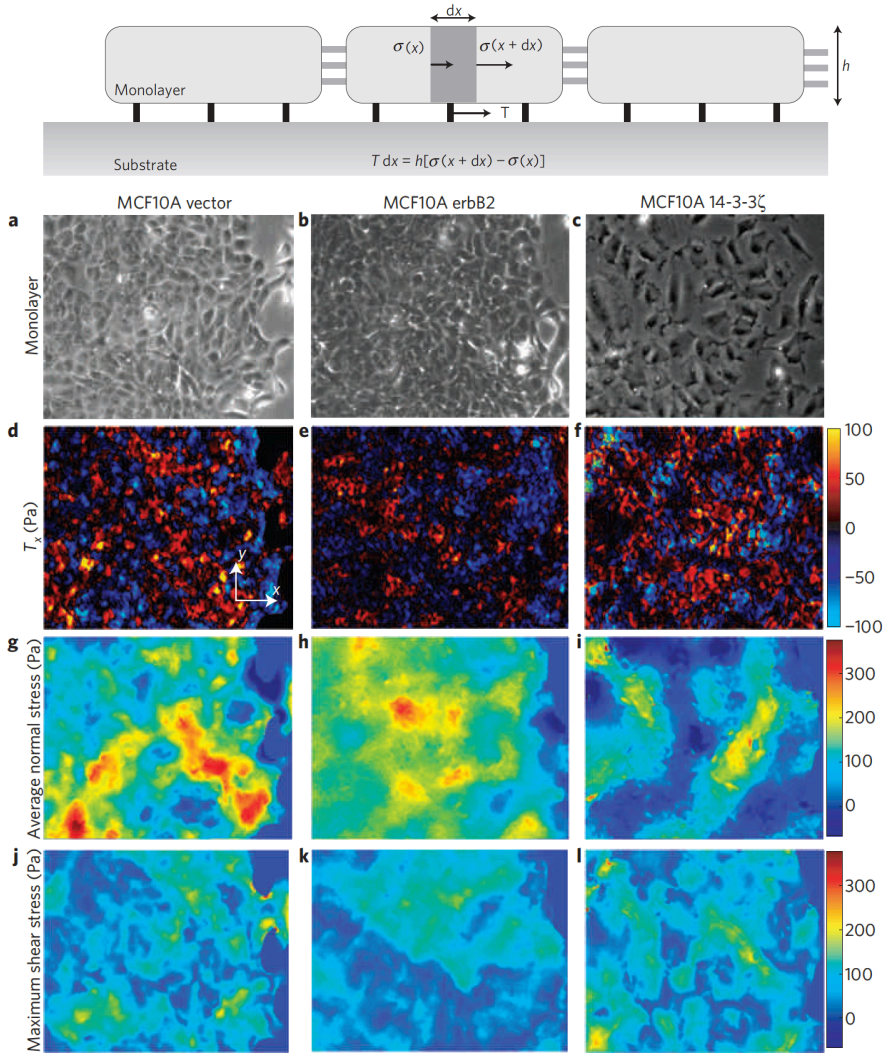

FIGURE 1.7: Top: one dimensional representation of the relationship between traction force T and intercellular stress σ. Bottom: stress maps and migration in monolayers of breast-cancer model systems. a-c: phase contrast images. d-f: cell-substrate tractions T_x. g-i: average normal stress. j-l: maximum shear stress [12].

The resulting stress maps also reveal a highly dynamical and heterogeneous mechanical landscape, characterized by large spatial and temporal fluctuations in the normal/shear stress (Fig. 1.7). The correlation between stress and cell velocities suggests an active mechanical feedback where the cells adjust their local velocities in the direction of minimal shear [12].

Theoretical progress has been made on the modeling of collective cell migration using SPP models [63] and continuum theories [64]. Meanwhile, models for confluent tissues have been developed in the context of morphogenesis [30]. One of a well-accepted model for confluent tissue is the vertex model, which represents the tissue as a collection of vertices outlining shapes of connected polygons corresponding to adherent cells [30].

The model captures active cellular contractility, intercellular adhesion and bulk elasticity with an effective mechanical energy functional depending on cell shapes. This energy functional is minimized to find stable mechanical configurations assuming the corresponding biological process is near equilibrium, an assumption reasonable in certain stages of morphogenesis which span time scales of days and weeks [65, 66]. This model has seen both qualitative and quantitative successes in developmental biology with process such as *drosophila* wing development [30]. Recent study with this model has also revealed a density-independent glass transition in a confluent tissue controlled by the competition between cellular contractility and cell-cell adhesion associated with a change in cell shape. This may be relevent to epithelial-mesenchymal transition in cancer invasion and cell sorting during embryonic development [18].

1.4 Outline

This dissertation investigates collective phenomena in active systems of biological relevance across length scales, ranging from intracellular actin systems to bird flocks. The study has been conducted via theoretical modeling and computer simulations using tools from soft condensed matter physics and non-equilibrium statistical mechanics. The work has been organized into two parts through five chapters. In part one (chapter 2 to 3), continuum theories have been utilized to study pattern formation in bacteria suspensions, actomyosin systems and bird flocks, whose dynamics is described generically within the framework of polar active fluids. The continuum field equations have been written down phenomenogically and derived rigorously through explicit coarse-graining of corresponding microscopic equations of motion. We have investigated the effects of alignment interaction, active motility, non-conserved density, and rotational inertia on pattern formation in active systems. In part two (chapter 4 to 6), computer simulations have been performed to study the self-organization and mechanical properties of dense active systems. A minimal self-propelled particle (SPP) model has been utilized to understand the aggregation and segregation of active systems under confinement (Chapter 4), where an active pressure has been defined for the first time to characterize the mechanical state of the active system. The same model is utilized in Chapter 5 to understand the self-assembly of passive particles in an active bath.

Chapter 2

Pattern Formation in Active Suspensions

2.1 Introduction

Active systems, such as bacterial suspensions and cell extracts of cytoskeletal filaments and associated molecular motors, self-organize into a variety of intriguing patterns visible under the microscope [6, 29, 67–71]. *Escherichia coli* and *Salmonella typhimurium* colonies growing on soft agar, for instance, form crystalline or amorphous arrangements of high-density bacterial clumps [6, 67, 68], as well as stripes [72]; while biofilms exhibit even more elaborate patterns [73]. In motility assays at high density actin filaments self-organize into coherently moving structures, such as clusters, swirls and traveling band [29, 69]. The formation of plane and spiral actin waves has been predicted in models of actin cytoskeletal dynamics [74–76]. The organization of actin in clumps and spiral waves has also been reported *in vivo* in the actomyosin cytoskeleton of immobilized *Dictyostelium* cells [9, 77]. The qualitative similarities between the patterns seen in these systems suggest that common principles may underlie such an organization.

A large amount of theoretical work has been devoted to understanding the role of external chemical cues in driving pattern formation in active systems by modeling them via coupled nonlinear diffusion-reaction equations [9, 67, 78]. The model described here belongs, in contrast, to a new class of effective descriptions of active systems that can lead to pattern formation on the basis of a *minimal* set of physically motivated ingredients [13, 79, 80]. Specifically, cell reproduction and death in bacterial suspensions [81] or polymerization in actin gels and solutions [9] are described by a reactive logistic term. Also included are motility suppression due to cells crowding and cell alignment, as it may be induced by medium-mediated hydrodynamic interaction, biochemical signaling

and quorum sensing [72, 82], or polarization of the actin cytoskeleton. Previous work summarized below has separately explored the role of some of the physical mechanisms included here, but has not considered their combined effect. By proposing an effective model with no reference to specific biochemical signaling, we offer a unified minimal description of the emergence of complex structures in a variety of active systems. In particular, we here discuss the application of our theory to pattern formation in bacterial and actin system.

2.2 Minimal continuum model

Our model is formulated in terms of two continuum fields, the cell or actin filament density, $\rho(\mathbf{r},t)$, and the polarization density, $\mathbf{w}(\mathbf{r},t)$. The vector field $\mathbf{w}$ plays the dual role of orientational order parameter describing the local polar alignment of active units traveling in the same direction and of current density. The continuum equations are

$$\partial_t \rho = -\boldsymbol{\nabla}\cdot(v\mathbf{w} - D\boldsymbol{\nabla}\rho) + \alpha\rho\,(1-\rho/\rho_s)\ , \tag{2.1a}$$

$$\partial_t \mathbf{w} + \frac{\gamma}{8\epsilon}\mathbf{w}\cdot\boldsymbol{\nabla}(v\mathbf{w}) = -\,(\epsilon-\gamma\rho)\,\mathbf{w} - \frac{\gamma^2}{2\epsilon}|\mathbf{w}|^2\mathbf{w} - \frac{1}{2}\boldsymbol{\nabla}\left(v\rho - \frac{3\gamma}{4\epsilon}vw^2\right) + D_w\nabla^2\mathbf{w}\ , \tag{2.1b}$$

where $v = v_0 e^{-\lambda\rho}$ is the density-dependent self propulsion speed, with λ a parameter controlling the decay of motility with increasing density. The density equation is a convection-diffusion equation, augmented by the logistic term describing growth/decay at rate α, with a saturation density ρ_s. The polarization equation has the same structure as the well-known Toner-Tu model of flocking [23, 83], but with additional nonlinearities arising from the density-dependent propulsion speed (for another generic equation of polar order in active systems see also [84]). It includes a convective term on the left hand side, and active corrections to the effective pressure proportional to w^2. Here, ϵ is a rotational diffusion rate determined by the strength of rotational noise and γ is the strength of the alignment interaction. The diffusion coefficients D and D_w control gradients in the bacterial density and polarization. For simplicity we assume $D_w = D$. In the absence of the logistic reactive term, Eqs. (2.1) are a simplified version of those derived recently by coarse graining a Vicsek model with density-dependent self propulsion speed [85]. The nonlinear advective terms which are here neglected do not change the physics (see Appendix 2.C). In the following we measure times in units of ϵ^{-1} and lengths in units of v_0/ϵ. We also define dimensionless fields $\tilde{\rho} = \rho/\rho_s$ and $\tilde{\mathbf{w}} = \mathbf{w}/\rho_s$. The model described by Eqs. (2.1) is then characterized by four dimensionless parameters, three of which are crucial to determine the physics: $\tilde{\lambda} = \lambda\rho_s$, $\tilde{\gamma} = \gamma\rho_s/\epsilon$, and $\tilde{\alpha} = \alpha/\epsilon$. These measure respectively the importance of density-dependent motility,

of alignment and of the reaction term. The fourth parameter, $\tilde{D} = D\epsilon/v_0^2$ denotes the scaled magnitude of the diffusion coefficient and elastic constant in the polarization equation.

When both motility suppression and the reaction term are neglected ($\tilde{\lambda} = \tilde{\alpha} = 0$), the equations describe the familiar Vicsek model. This has a mean field transition from a homogeneous isotropic ($\mathbf{w} = 0$) state to a homogeneous polar (moving) state ($\mathbf{w} = w_0\hat{\mathbf{x}}$) when alignment $\gamma\rho_s$ exceeds noise ϵ ($\tilde{\gamma} > 1$). In this model, emergent structures arise only in the polar state from the growth of fluctuations in the magnitude of polarization due to the $\gamma\rho_s$ term. Motility suppression qualitatively alters this well known scenario. In models with density conservation ($\tilde{\alpha} = 0$) and no alignment ($\tilde{\gamma} = 0$), it can yield macroscopic phase separation, with large pretransitional density fluctuations, when $\tilde{\lambda} > 1$ [10, 36]. Breaking density conservation is essential to yield the length selection seen in experiments, as shown in [13] for non-aligning systems, where a finite growth/death rate arrests phase separation yielding concentric rings and high density spots not unlike the bacterial "dots" observed in *Salmonella typhimurium*. The combined effect of alignment and motility suppression has only been considered in systems with density conservation ($\tilde{\gamma} \neq 0$, but $\tilde{\alpha} = 0$) [85]. In this case the interplay of self-trapping and alignment destabilizes both the homogeneous disordered and ordered states, yielding a rich collection of macroscopically separated traveling states, including bands, clumps and lanes [85], but with no length selection. The minimal model proposed in this paper incorporates alignment, density growth/decay and motility suppression and demonstrates that in different parameter regions these physical mechanisms can account qualitatively for the patterns seen in very diverse active systems. In particular, as we discuss more below, the patterns formed for small $\tilde{\alpha}$ are naturally associated to those seen in bacterial fluids, where growth is much slower than motion; whereas those observed for large $\tilde{\alpha}$ and $\tilde{\gamma}$ apply to polymerizing actin systems, where reaction rates vary depending on monomeric actin concentration, and the local density of actin fibers can promote their orientational order. In what follows, the language used to describe the dynamics in these parameter ranges will reflect that of the biophysical system they apply to.

2.2.1 Isotropic-Polar phase transition

The continuum equations for the density $\rho(\mathbf{r}, t)$ and polarization density $\mathbf{w}(\mathbf{r}, t)$ given in Eqs. (2.1) have two homogeneous, stationary solutions:

- a homogeneous isotropic state, with $\rho = \rho_s$ and $\mathbf{w} = 0$, for $\gamma\rho < \epsilon$ ($\tilde{\gamma} < 1$);
- a uniform polarized state, with $\rho = \rho_s$ and $\mathbf{w} \neq 0$ for $\gamma\rho > \epsilon$ ($\tilde{\gamma} > 1$),

Choosing the x axis along the direction of mean polarization, we find $\mathbf{w} = \hat{\mathbf{x}} w_0$, with $w_0 = \sqrt{2\epsilon(\gamma\rho_s - \epsilon)}/\gamma$, in the polarized state, which is also a uniformly moving state. Next we examine the linear stability of each of these two states with respect to small fluctuations in both fields from their uniform values. Quantities with tilde below are dimensionless, as defined in the main text.

2.3 Chemotactic bacterial droplets

To examine the linear stability of the isotropic state for $\tilde{\gamma} < 1$, we study the dynamics of fluctuations $\delta\tilde{\rho} = \tilde{\rho} - 1$ and $\Theta = \boldsymbol{\nabla} \cdot \tilde{\mathbf{w}}$. For clarity of discussion, it is useful to restore dimensional parameters. Working in Fourier space, we let $(\delta\tilde{\rho}, \Theta) = \sum_{\mathbf{q}} (\rho_{\mathbf{q}}, \Theta_{\mathbf{q}}) e^{i\mathbf{q}\cdot\mathbf{r}}$. The time evolution of $\rho_{\mathbf{q}}$ and $\Theta_{\mathbf{q}}$ is then governed by

$$\partial_t \rho_{\mathbf{q}} = -v\Theta_{\mathbf{q}} - Dq^2\rho_{\mathbf{q}} - \alpha\rho_{\mathbf{q}} \,, \tag{2.2a}$$

$$\partial_t \Theta_{\mathbf{q}} = -\epsilon_r \Theta_{\mathbf{q}} + \frac{1}{2}(v + \rho_s v')q^2\rho_{\mathbf{q}} - Dq^2\Theta_{\mathbf{q}} \,, \tag{2.2b}$$

where $\epsilon_r = \epsilon - \gamma\rho_s$ is the rotational diffusion rate renormalized by alignment and the prime denotes a derivative with respect to density. The decay/growth of fluctuations is governed by the eigenvalues of Eqs. (2.2). The stability is controlled by the rate $s_+(q)$, given by

$$s_+(q) = -\frac{\alpha + \epsilon_r + 2Dq^2}{2} + \frac{\sqrt{(\alpha - \epsilon_r)^2 - 4\epsilon D_{sp} q^2}}{2} \,, \tag{2.3}$$

where we have introduced an effective diffusivity $D_{sp}(\rho) = \left(1 + \frac{1}{2}\frac{d}{d\rho}\right)\frac{v^2(\rho)}{2\epsilon}$, with $v^2(\rho)/(2\epsilon)$ the diffusivity of a single particle performing a persistent random walk with run speed $v(\rho)$ and diffusion (tumble) rate ϵ. In Eq. (2.3) all quantities are evaluated at ρ_s. For the chosen form of $v(\rho)$, the effective diffusivity $D_{sp} = \frac{v_0^2}{2\epsilon} e^{-2\tilde{\lambda}}(1 - \tilde{\lambda})$ can change sign when $\tilde{\lambda} > 1$. The rate s_+ becomes positive for $D_{sp} < -D\left(\sqrt{\frac{\alpha}{\epsilon}} + \sqrt{\frac{\epsilon_r}{\epsilon}}\right)^2$. Motility suppression then promotes phase separation in regions of high and low density [10], which is in turn arrested by the density growth/decay. Active particles (here representing bacteria) tend to grow in low density regions and die/decay in high density regions, hence must migrate from high density to low density regions to obtain a steady state. The interplay of these two mechanisms ultimately yields a stable pattern. The linear stability analysis also yields the wave vector $q_c \sim D^{-1/2}\left[\alpha\epsilon_r\right]^{1/4}$ of the most unstable mode: the length scale q_c^{-1} decreases with increasing α and ϵ_r, consistent with the behavior shown in the density maps of Fig. 2.1. For very large $\tilde{\lambda}$ the active contribution to the effective diffusivity vanishes as $D_{sp} \to 0$, and the homogeneous state is again stable. The 'knee' in the curves at $\tilde{\lambda} = 1.5$ corresponds to the minimum of D_{sp} (Fig. 2.2). Finally, the instability exists even for $\alpha = 0$, although in this case the system coarsens into macroscopic phase

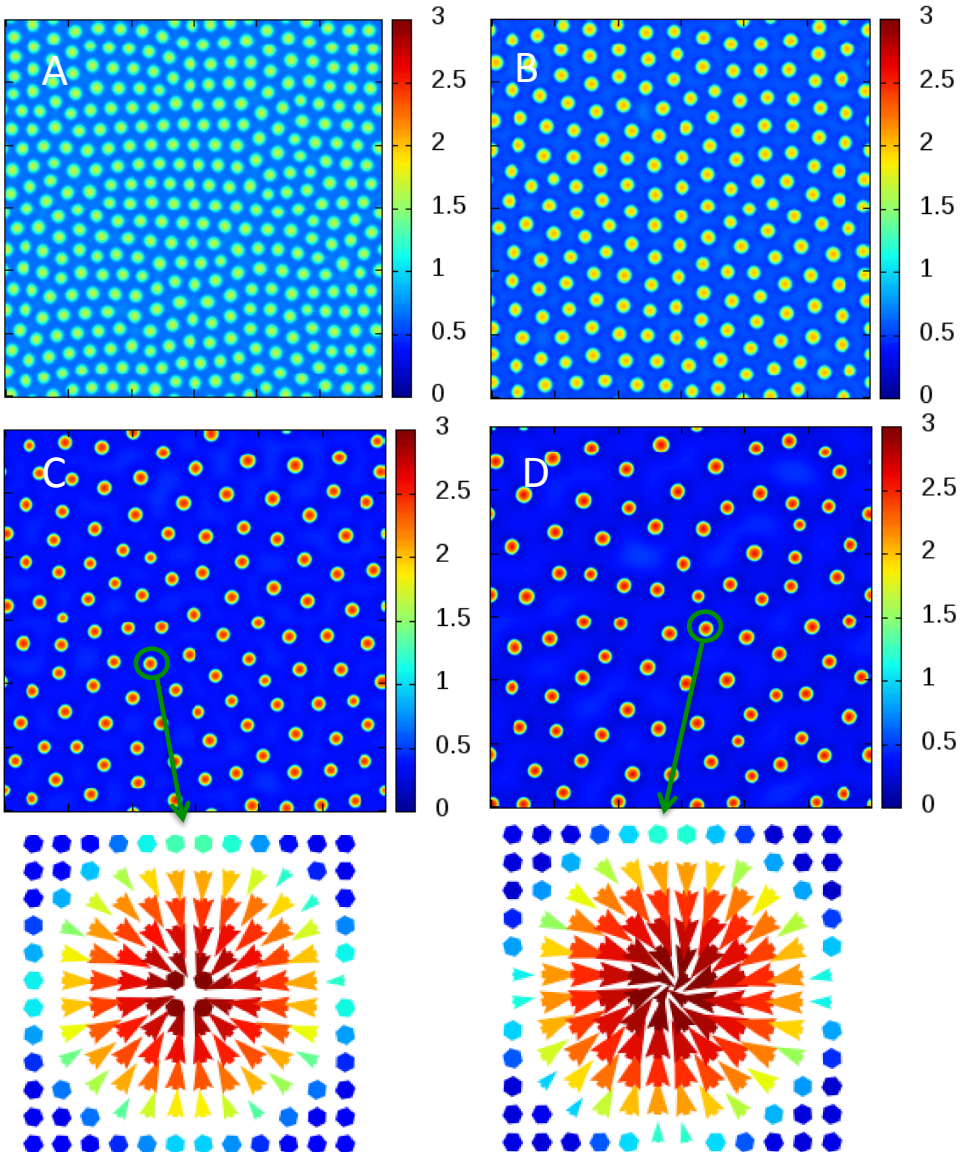

FIGURE 2.1: (color online) Color maps of the density obtained by numerical integration of Eqs. (2.29) in a box with periodic boundary conditions and an initial isotropic state ($\mathbf{w} = 0$) of uniform mean density $\rho_0 = \rho_s$, with small random fluctuations. The color bars give the values of the local density $\tilde{\rho} = \rho/\rho_s$. All images are for $\tilde{\lambda} = 1.4$, $\tilde{D} = 0.01$, $\tilde{\alpha} = 0.083$ and (from A to D) $\tilde{\gamma} = 0.50,\ 0.58,\ 0.75,\ 0.95$. The high density static bacterial dots in A and B have zero or very small local polar order, as in [13]. In C and D polar order builds up in each dot, as highlighted by the blow ups of individual dots shown in the bottom row. Here the polarization is displayed as an arrow of length proportional to its magnitude. The color refers to the density, with the same color scheme as indicated in the side bars (see also Supplementary Movies 1 and 2).

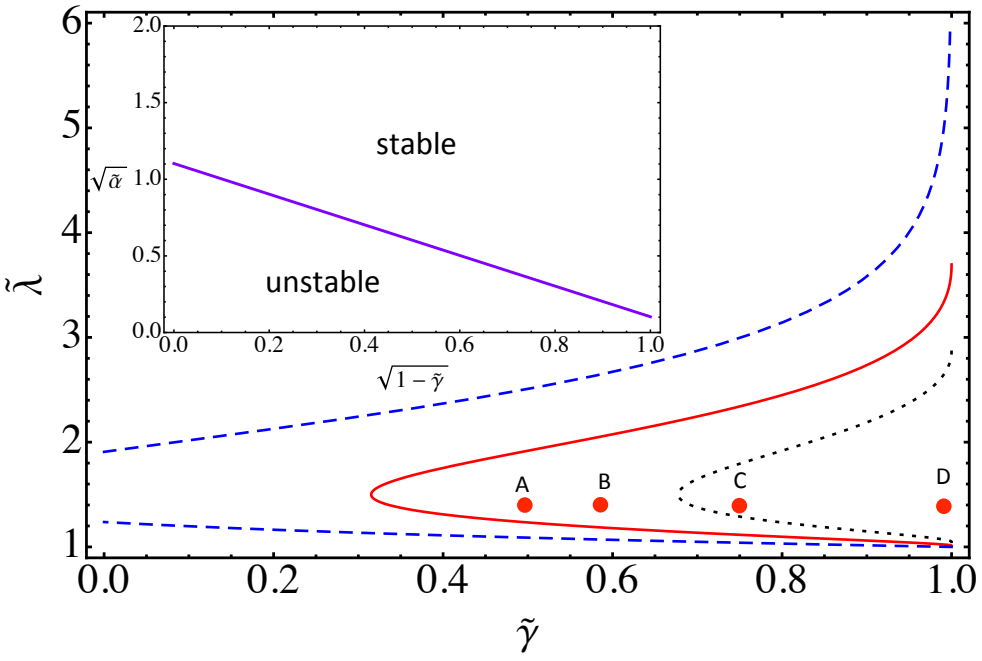

FIGURE 2.2: (color online) The boundary of linear stability of the homogeneous state ($\tilde{\gamma} < 1$) in the $(\tilde{\lambda}, \tilde{\gamma})$ plane for $\tilde{\alpha} = 0$ (dashed curve, blue online), $\tilde{\alpha} = 0.083$ (solid curve, red online) and $\tilde{\alpha} = 0.30$ (dotted curve, black online). The homogeneous state is unstable in the region to the right of each curve, up to the vertical axis $\tilde{\gamma} = 1$. The calculation is described in Appendix B. The dots labeled A, B, C, D show the location in parameter space of the images shown in Fig. 2.1 and refer to $\alpha = 0.083$. For a fixed value of $\tilde{\alpha}$, the region of $\tilde{\lambda}$ where the system is unstable grows as alignment increases. Conversely, increasing the birth/death rate for fixed $\tilde{\gamma}$ stabilizes the homogeneous state. This is highlighted in the inset that shows the linear stability boundary in the $(\tilde{\alpha}, \tilde{\gamma})$ plane for $\tilde{\lambda} = 1.4$. Note that in the inset the horizontal axis is $\sqrt{1-\tilde{\gamma}}$, i.e., alignment increases to the left.

separated regions, rather than forming a stable pattern (see Supplementary Movies 6 and 7). Increasing α for fixed alignment strength tends to stabilize the uniform state.

2.3.1 Bacterial clusters with internal structure

In bacteria the birth/death rate α is of the order of inverse hours and the run length v_0/ϵ is typically $\sim 10-30\mu m$, with $\epsilon \sim 1\text{s}^{-1}$. In this case, and provided $\gamma\rho_s < \epsilon$, the dynamics of the polarization is much faster that that of the density. One can exploit this separation of time scales by neglecting $\partial_t \mathbf{w}$ in Eq. (3.3) and eliminating polarization in terms of density in Eq. (2.1a). At large length scales, this yields an effective diffusion equation of the type studied in [13], with a diffusivity that changes sign, signaling the onset of phase separation. In this range of parameters, incorporating polarization dynamics yields polar structure within the high density static dots found in [13], with the dots turning into

asters and spirals, but does not change the structure of the overall pattern. The polar structure of the dots shown in Fig. 2.1 arises when the density $\rho > \rho_s$ inside an individual dot is large enough that $\gamma\rho > \epsilon$, i.e., the system acquires polar order. To our knowledge, such static asters and spirals have not yet been reported in bacterial suspension, but they should be visible by electron microscopy in experiments with self-chemotactic bacterial strains in semi-solid agar [86], as the density in the resulting clusters has been estimated to be 100 times larger than in uniform cultures [87]. As $\tilde{\gamma} = \gamma\rho_s/\epsilon \to 1^-$, the polar structure becomes more pronounced. When all nonlinearities are taken into account (see Appendix 2.C), close to the transition and for a large value of the reproduction rate, the model yields 'blinking' dot patterns.

2.3.2 Spreading bacterial droplets

Finally, Fig. 2.3 shows the patterns obtained from the spreading of a bacterial drop inoculated at the center of the sample.

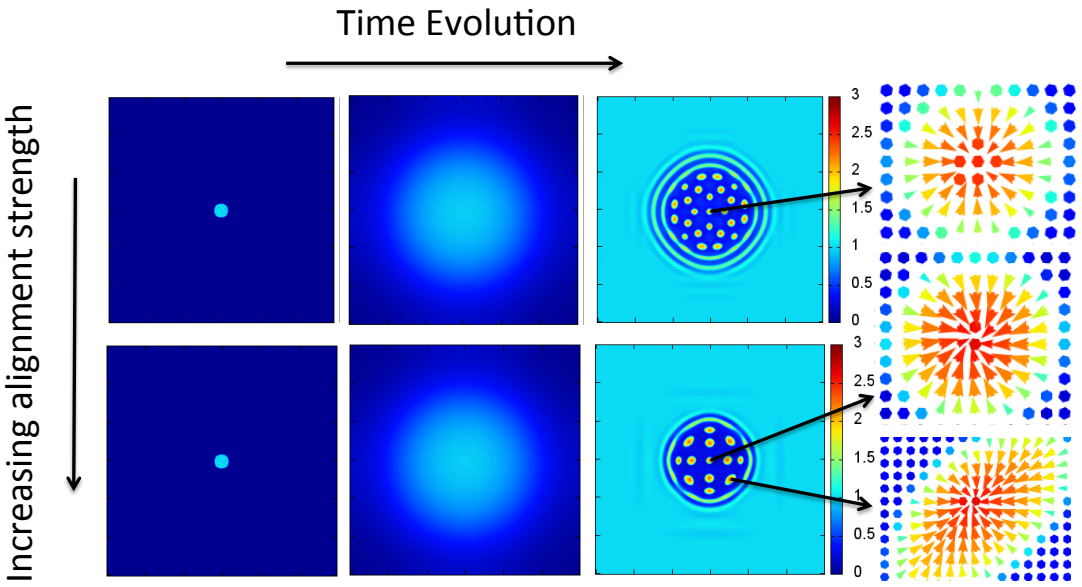

FIGURE 2.3: (color online) Snapshots of the spreading of a droplet inoculated at the center of the simulation sample for $\tilde{\gamma} = 0.83$ (top row) and $\tilde{\gamma} = 0.98$ (bottom row), with $\tilde{\alpha} = 0.167$, $\tilde{\lambda} = 1.40$ and $\tilde{D} = 0.01$. The simulation times are $1, 4000, 22000$ and $1, 4000, 14000$ from left to right in the unit of ϵ^{-1} respectively. The blow-ups to the right show the internal structure of the dots, as described in the caption of Fig. 2.1.

2.4 Intracellular actin waves

In the uniform polar state ($\mathbf{w} = w_0\hat{\mathbf{x}}$), instabilities exist even for $\lambda = 0$ and $\alpha = 0$ and these have been studied before [88, 89]. The reactive logistic term provides a mechanism

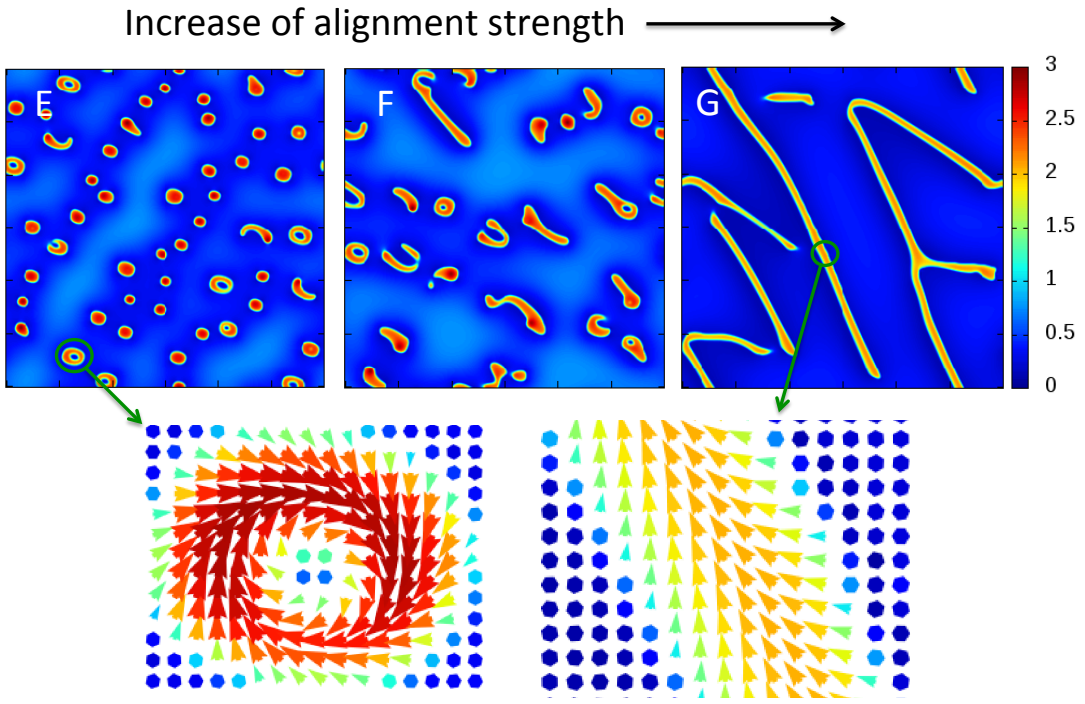

FIGURE 2.4: (color online) Patterns in the polar state obtained from a uniform initial state with small random fluctuations around $\tilde{\rho} = 1$ and $\tilde{\mathbf{w}} = \mathbf{0}$ for $\tilde{\alpha} = 0.08$, $\tilde{D} = 0.01$ and $\tilde{\lambda} = 1.10$. Rings/lanes emerge in (E) (F) (G) at $\tilde{\gamma} = 1.11, 1.25, 2.00$, respectively. We stress that the net total polarization of the lanes shown in frame G is directed at an angle to the long direction of the lanes, resulting in a transverse drifting motion (See Supplementary Movie 4).

for pattern scale selection. The study of the dynamics in the polarized state for variable values of $\tilde{\alpha}$ may not apply to usual bacterial suspensions, where growth is slow with respect to motion, and aligning effects are insufficient to yield an overall orientationally ordered phase (one exception might be provided by swarms). This study is however highly relevant to actomyosin systems, where (i) immobilized motors (*in vitro*, e.g., in motility assays [29]) or treadmilling (*in vivo*) lead to propulsion; (ii) steric effects may cause motility suppression; (iii) polymerization (limited by actin crowding) occurs on time scales comparable to rotational diffusion and (iv) the density can easily become large enough to induce local polar order [29].

For the parameters used in our model, when $\lambda = \alpha = 0$ fluctuations in the magnitude of polarization of wave vector $\mathbf{q} \| x$ destabilize the uniform state for $1 \leq \tilde{\gamma} \leq \frac{v_0}{4}\sqrt{\frac{\epsilon}{D}}$, while splay fluctuations with $\mathbf{q} \perp x$ are always unstable. Both these longitudinal and transverse instabilities have been discussed extensively. In particular, the longitudinal instability has been argued to signal the onset of high density ordered bands normal to the direction of mean polarization traveling in a disordered low density background [88, 89]. The suppression of motility induced by a finite λ yields a host of complex structures, including traveling dots, stripes and lanes that coarsen at long times into anisotropic

phase separated states [85]. A finite value of $\tilde{\alpha}$ arrests the phase separation and yields patterns with a characteristic length scale, as shown in Fig. 2.4. In the region $\tilde{\gamma} > 1$ the patterns are always dynamical, with the spirals rings continuously breaking up and reconnecting, as displayed in Supplementary Movies 3 and 4. Such never-settling states are, interestingly, virtually absent (except for simple traveling waves) in previous versions of the model, neglecting either alignment or reaction.

The dynamical patterns featuring ever-evolving spirals and lanes in Fig. 2.4 bear a striking qualitative similarity to the actin waves and dynamical spiral patterns observed in the cytoskeleton of Dictyostelium [9, 28]. In this system polymerization/depolymerization rates are of order $1 - 100$ s^{-1}, hence comparable to the rotational diffusions rates $\epsilon \sim 1 - 20$ s^{-1} for a 1 μm filament [90]. Here individual cells were first immobilized by depolymerizing actin with latrunculin. Upon latrunculin reduction, static spots of actin were seen to form in the cortex. At later times, the spots become dynamical and eventually turn into spiral waves that closely resemble our ever-evolving rings, and allow the cell to eventually resume motility. The experimental observation was modeled in [9] by a reaction-diffusion model where actin density and orientation growth are controlled by a chemical inhibitor. Our model provides a simpler physical interpretation of the self-organization where chemical signaling does not need to be explicitly incorporated in the dynamics, but only enters through effective parameters: λ that captures the aggregation of actin driven by membrane-bound protein complexes [28], and α representing the (crowding-limited) actin polymerization rate. The transition from actin clusters to spirals and finally to traveling waves as observed in Supplementary Movies 1 and 4 of Ref [28] is obtained in our model by increasing $\tilde{\gamma}$, as shown in Fig. 2.4, which corresponds to increased alignment of the actin filaments *in vivo* due to the increase of density through polymerization.

2.5 Appendix 2.A: Linear stability of the isotropic state

We consider the dynamics of fluctuations $\delta\tilde{\rho}(\mathbf{r},t) = \tilde{\rho}(\mathbf{r},t) - 1$ and $\delta\tilde{\mathbf{w}}(\mathbf{r},t) = \tilde{\mathbf{w}}(\mathbf{r},t)$ to linear order. We let $\Theta = \boldsymbol{\nabla}\cdot\delta\tilde{\mathbf{w}}$ and denote by $\delta\tilde{\mathbf{w}}^{\perp}$ the transverse part of the polarization. The linearized equations for the fluctuations are then given by

$$\partial_t\delta\tilde{\rho} = -v\Theta + D\nabla^2\delta\tilde{\rho} - \alpha\delta\tilde{\rho}\,, \tag{2.4a}$$

$$\partial_t\Theta = -\epsilon_r\Theta - \frac{1}{2}(v+\rho_s v')\nabla^2\delta\tilde{\rho} + D\nabla^2\Theta\,, \tag{2.4b}$$

$$\partial_t\delta\tilde{\mathbf{w}}^{\perp} = -\epsilon_r\delta\tilde{\mathbf{w}}^{\perp} + D\nabla^2\delta\tilde{\mathbf{w}}^{\perp}\,, \tag{2.4c}$$

where $\epsilon_r = \epsilon - \gamma\rho_s > 0$, $v = v_0 e^{-\tilde{\lambda}}$ and $\rho_s v' = -\tilde{\lambda} v_0 e^{-\tilde{\lambda}}$. The transverse part of the polarization is decoupled to linear order and always decays. It will be ignored in the rest of this section. Working in Fourier space, we let $(\delta\tilde{\rho}, \Theta) = \Sigma_{\boldsymbol{q}}(\rho_{\boldsymbol{q}}, \Theta_{\boldsymbol{q}}) e^{i\boldsymbol{q}\cdot\boldsymbol{r}}$. The time evolution of the Fourier amplitudes $\rho_{\boldsymbol{q}}$ and $\Theta_{\boldsymbol{q}}$ is then governed by the equations

$$\partial_t \rho_{\boldsymbol{q}} = -v\Theta_{\boldsymbol{q}} - Dq^2\rho_{\boldsymbol{q}} - \alpha\rho_{\boldsymbol{q}} \,, \tag{2.5a}$$

$$\partial_t \Theta_{\boldsymbol{q}} = -\epsilon_r \Theta_{\boldsymbol{q}} + \frac{1}{2}(v + \rho_s v')q^2\rho_{\boldsymbol{q}} - Dq^2\Theta_{\boldsymbol{q}} \,. \tag{2.5b}$$

We seek solution of the form $\rho_{\boldsymbol{q}}, \Theta_{\boldsymbol{q}} \sim e^{s(q)t}$. The eigenvalues are then given by

$$\begin{aligned} s_\pm(q) &= -\frac{1}{2}\left(\alpha + \epsilon_r + 2Dq^2\right) \\ &\quad \pm \frac{1}{2}\sqrt{(\alpha - \epsilon_r)^2 - 4\epsilon\mathcal{D}_{sp}q^2} \,, \end{aligned} \tag{2.6}$$

where we have introduced the effective diffusivity

$$\mathcal{D}_{sp} = (1 + \frac{\rho}{2}\frac{d}{d\rho})D_s = \frac{v_0^2}{2\epsilon} e^{-2\tilde{\lambda}}(1 - \tilde{\lambda}) \,, \tag{2.7}$$

with $D_s = v^2/(2\epsilon)$. The diffusivity $\mathcal{D}_{sp}$ is negative for $\tilde{\lambda} > 1$ and has a negative minimum value at $\tilde{\lambda} = 1.5$. For $\tilde{\lambda} > 1.5$ it approaches zero from below. The eigenvalues $s_\pm(q)$ describe the time evolution of linear combinations of fluctuations in the density and the longitudinal part of the polarization density, which to linear order is proportional to the magnitude of the polarization field. When $\alpha = 0$, the mode $s_+(q)$ is hydrodynamic as $Re[s_+(q \to 0)] = 0$, as required by density conservation, and describes the decay of density fluctuations. The mode $s_-(q)$ mainly describes the dynamics of polarization which decays at finite rate ϵ_r when $q = 0$ and becomes long lived at the transition where $\epsilon_r = 0$. This is highlighted by expanding the dispersion relations for small q, with the result

$$s_+(q, \alpha = 0) = -q^2\left(D + \mathcal{D}_{sp}\frac{\epsilon}{\epsilon_r}\right) + \mathcal{O}(q^4) \,, \tag{2.8a}$$

$$s_-(q, \alpha = 0) = -\epsilon_r - q^2\left(D - \mathcal{D}_{sp}\frac{\epsilon}{\epsilon_r}\right) + \mathcal{O}(q^4) \,, \tag{2.8b}$$

where the expansion can be carried out only away from the transition, where ϵ_r remains finite. When α is finite both modes are non-hydrodynamic. The s_+ mode is unstable when $Re[s_+] > 0$, which gives the instability condition

$$\mathcal{D}_{sp} < \mathcal{D}_{sp}^c = -D\left(\sqrt{\frac{\alpha}{\epsilon}} + \sqrt{\frac{\epsilon_r}{\epsilon}}\right)^2 < 0 \,. \tag{2.9}$$

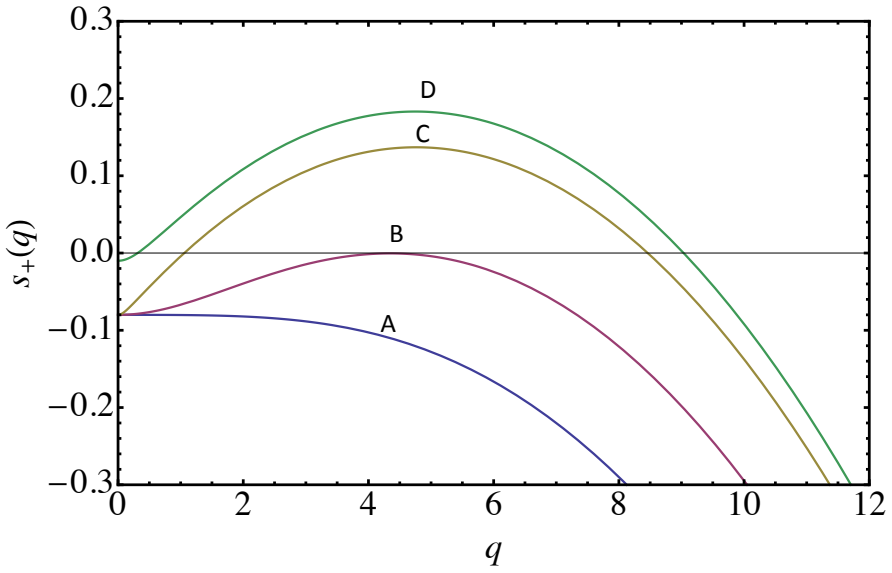

FIGURE 2.5: (color online) The dispersion relation of the mode $s_+(q)$ is plotted as a function of the wave vector q for $\tilde{\alpha} = 0.08$, $\tilde{D} = 0.01$ and $\tilde{\lambda} = 1.2$. The curves from A to D correspond to $\tilde{\gamma} = 0, 0.55, 0.9$ and 0.99. The homogeneous isotropic state is unstable for $s_+(q) > 0$ and stable for $s_+(q) < 0$. The instability is enhanced upon increasing the alignment strength $\tilde{\gamma}$ due to the decrease of the decay rate ϵ_r of the polarization as the mean field transition at $\tilde{\gamma} = 1$ is approached from below. The instability exists in a band of wave vectors $q_1 < q < q_2$. When $\alpha < \epsilon_r$, as in typical bacterial suspensions, the decay rate at zero wave vector is controlled by α (curves A to C), while when $\alpha > \epsilon_r$, it is controlled by ϵ_r (curve D).

The linear stability boundary $\mathcal{D}_{sp}^c$ defined by Eq. (2.9) is shown in Fig. 2 of the paper for $v = v_0 e^{-\tilde{\lambda}}$. Clearly the specific form of the stability boundary depends on the form chosen for $v(\rho)$. At large λ the diffusivity $\mathcal{D}_{sp}$ vanishes and the uniform state is stable, as obtained in Ref. [13]. As γ is increased for a fixed α, the region of instability widens. The instability occurs even for $\alpha = 0$, where $\mathcal{D}_{sp}^c = -D\frac{\epsilon}{\epsilon_r}$. In this case, however, the uniform state is unstable on all scales, corresponding to macroscopic phase separation [10], as shown in Fig. 2.6. The dispersion relation of the mode $s_+(q)$ is shown in Fig. 2.5 for various values of the alignment strength. The instability occurs in a band of wave vectors $q_1 < q < q_2$, with

$$q_{1,2} = \sqrt{\frac{1}{2D^2}\left\{-\left[\mathcal{D}_{sp}\epsilon + D\left(\alpha + \epsilon_r\right)\right] \mp \sqrt{\left[\mathcal{D}_{sp}\epsilon + D\left(\alpha + \epsilon_r\right)\right]^2 - 4D^2\alpha\epsilon_r}\right\}} \tag{2.10}$$

When $\alpha = 0$, $q_1 = 0$ and $q_2 = \sqrt{-(\mathcal{D}_{sp}\epsilon + \epsilon_r D)}/D$. Conversely, at the mean field transition where $\epsilon_r = 0$, $\mathcal{D}_{sp}^c = -D\alpha/\epsilon$ and we find $q_1 = 0$, $q_2 = \sqrt{-(\mathcal{D}_{sp}\epsilon + \alpha D)}/D$. To examine the behavior as the mean-field order-disorder transition is approached form

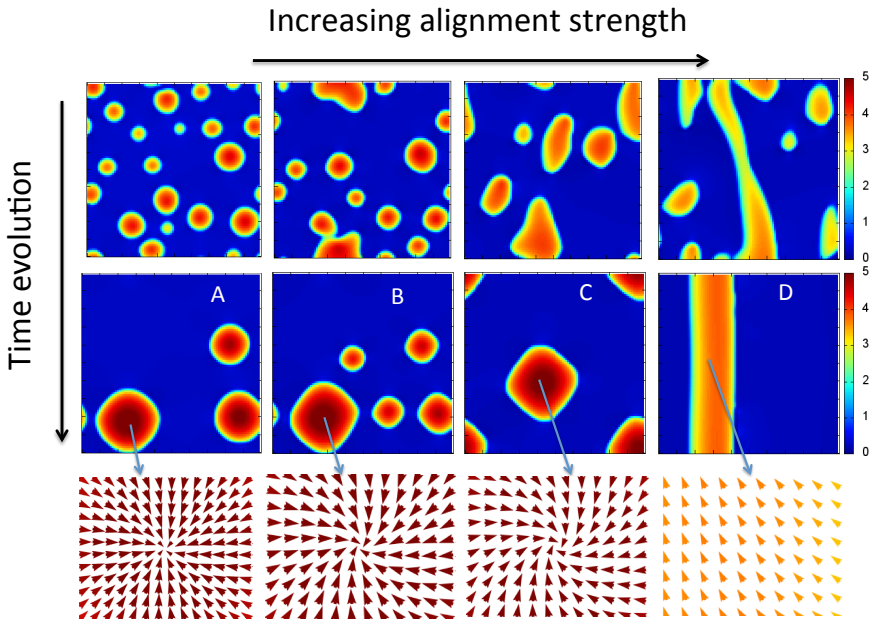

FIGURE 2.6: Density heat maps for $\tilde{D} = 0.01$, $\tilde{\lambda} = 1.2$ and $\tilde{\alpha} = 0$. showing macroscopic phase separation. The color scale is indicated to the right, and the values refer to $\tilde{\rho} = \rho/\rho_s$. From A to D, $\tilde{\gamma} = 0.50, 0.75, 0.96$ and 1.11. The time evolution shows the coarsening of the structures into a single large cluster. Upon increasing the alignment strength, the cluster starts to display polar order, as highlighted in the blowups in the bottom row showing maps of the polarization field.

below, we let we let $\mathcal{D}_{sp} = \mathcal{D}_{sp}^c - \delta$, with $\delta > 0$. To leading order in δ we obtain

$$q_{1,2} \simeq \frac{(\alpha\epsilon_r)^{1/4}}{D^{1/2}} \left[1 \mp \frac{\delta^{1/2}}{2} \left(\frac{\epsilon}{D\sqrt{\alpha\epsilon_r}} \right)^{1/2} + \mathcal{O}(\delta) \right] \tag{2.11}$$

At the onset of the instability, where $\delta = 0$, the wave vector of the unstable mode is $q_c = q_1 = q_2$, with

$$q_c = \frac{(\alpha\epsilon_r)^{1/4}}{D^{1/2}} \, . \tag{2.12}$$

The wavelength of the pattern then scales as $\ell_c \sim q_c^{-1} = D^{1/2}(\alpha\epsilon_r)^{-1/4}$. Finally, when $D = 0$, the isotropic state is unstable for $\mathcal{D}_{sp} < 0$, i.e., $\tilde{\lambda} > 1$ and $q > \sqrt{\frac{\alpha\epsilon_r}{|\mathcal{D}_{sp}\epsilon|}}$. In other words, a finite value of D is needed to stabilize the system at small scales.

To make contact with the model of bacterial suspensions studied in Ref. [13] that neglect polarization, we assume $\alpha << \epsilon$, which is generally true for bacteria and let $\tilde{\gamma} = 0$. In this case the fluctuations in polarization decay at the fast rate ϵ. On times large compared to ϵ^{-1}, we can neglect the time derivative on the left hand side of Eq. (2.5b), solve for $\Theta_{\mathbf{q}}$ to low order in $\mathbf{q}$, and eliminate the polarization from Eq. (2.5a) to obtain a closed equation for the density, given by

$$\partial_t \rho_{\mathbf{q}} = -\left(D + \mathcal{D}_{sp}\right) q^2 \rho_{\mathbf{q}} - \alpha\rho_{\mathbf{q}} + \frac{D\mathcal{D}_{sp}}{\epsilon} q^4 \rho_{\mathbf{q}} \, . \tag{2.13}$$

In the region $\tilde{\lambda} > 1$ where $\mathcal{D}_{sp} < 0$, we can define an effective surface tension $\kappa_{eff} = D|\mathcal{D}_{sp}|/\epsilon$ and Eq. (2.13) is then formally identical to the linearized form of the density equation proposed in Ref. [13]. This effective surface tension vanishes, however, at large λ, when $\mathcal{D}_{sp} \to 0$. In this limit the approximation used to obtain Eq. (2.13) no longer applies.

Finally, we summarize a few key points:

- As discussed by Cates *et al* [13], pattern formation in the isotropic state is the result of the interplay of motility suppression that drives the effective diffusivity $\mathcal{D}_{sp}$ negative triggering macroscopic phase separation, and birth/death that arrests phase separation.
- Deep in the isotropic state ($\tilde{\gamma} << 1$), the polarization decays on microscopic times $\sim (\epsilon - \gamma\rho_s)^{-1} \sim \epsilon^{-1}$ and can be neglected. The instability is then controlled entirely by the dynamics of density fluctuations, as in the model of Ref. [13].
- When $\tilde{\gamma}$ approaches 1 from below, the decay of polarization fluctuations slows down. In this case if $\alpha >> \epsilon_r$ there is a range of time scales where one can neglect density fluctuations and describe the dynamics entirely in terms of $\Theta = \boldsymbol{\nabla} \cdot \mathbf{w}$. One obtains again bacterial dots that display, however, polar structure.

2.6 Appendix 2.B: Linear stability of the polarized state

To examine the linear stability of the polarized state, we linearize Eqs.2.1 in fluctuations about a uniform polar state by letting

$$\delta\tilde{\rho}(\mathbf{r},t) = \tilde{\rho}(\mathbf{r},t) - 1 \,, \tag{2.14}$$

$$\delta\tilde{\mathbf{w}}(\mathbf{r},t) = \tilde{\mathbf{w}}(\mathbf{r},t) - \mathbf{w}_0/\rho_s \,, \tag{2.15}$$

where $\mathbf{w}_0 = \hat{\mathbf{x}} w_0$ and $w_0 = \sqrt{2\epsilon(\gamma\rho_s - \epsilon)}/\gamma$. Since the polarized state exists for $\gamma\rho_s > \epsilon$, to simplify the notation below we introduce the dimensionless parameter $\eta = \gamma w_0/\epsilon = \sqrt{2(\gamma\rho_s - \epsilon)/\epsilon}$ that is positive in the polar state and vanishes at the mean-field transition. The linearized equations are then given by

$$\partial_t \delta\tilde{\rho} = -v\boldsymbol{\nabla} \cdot \delta\tilde{\mathbf{w}} - \frac{\epsilon\eta}{\gamma} v' \partial_x \delta\tilde{\rho} + D\nabla^2 \delta\tilde{\rho} - \alpha\delta\tilde{\rho} \,, \tag{2.16a}$$

$$\begin{aligned}\partial_t \delta\tilde{\mathbf{w}} = -\epsilon\eta^2 \delta\tilde{w}_x \hat{\mathbf{x}} + \epsilon\eta\delta\tilde{\rho}\hat{\mathbf{x}} - \frac{1}{2}\left[(v + \rho_s v')\boldsymbol{\nabla} - \frac{3}{4}\frac{\epsilon\eta^2}{\gamma} v' \boldsymbol{\nabla} + \frac{\epsilon\eta^2}{4\gamma} v' \hat{\mathbf{x}}\partial_x\right]\delta\tilde{\rho} \\ + \frac{3}{4}\eta v \; \boldsymbol{\nabla}\delta\tilde{w}_x - \frac{1}{8}\eta v \; \partial_x \delta\tilde{\mathbf{w}} + D\nabla^2 \delta\tilde{\mathbf{w}} \,.\end{aligned} \tag{2.16b}$$

Introducing spatial Fourier transforms $(\delta\tilde{\rho}, \delta\tilde{\mathbf{w}}) = \Sigma_{\boldsymbol{q}}(\rho_{\boldsymbol{q}}, \mathbf{w}_{\boldsymbol{q}})e^{i\boldsymbol{q}\cdot\boldsymbol{r}}$, the equations for the Fourier amplitudes are given by

$$\partial_t \rho_{\boldsymbol{q}} = -vi\mathbf{q}\cdot\mathbf{w}_{\mathbf{q}} - \frac{\epsilon\eta}{\gamma}v' iq_x\rho_{\boldsymbol{q}} - Dq^2\delta\tilde{\rho} - \alpha\rho_{\boldsymbol{q}} \,, \tag{2.17a}$$

$$\partial_t \mathbf{w}_{\mathbf{q}} = -\epsilon\eta^2 w^x_{\mathbf{q}}\hat{\mathbf{x}} + \epsilon\eta\ \rho_{\mathbf{q}}\hat{\mathbf{x}} - \frac{1}{2}\left[(v+\rho_s v')i\mathbf{q} - \frac{3}{4}\frac{\epsilon\eta^2}{\gamma}v' i\mathbf{q} + \frac{\epsilon\eta^2}{4\gamma}v'\hat{\mathbf{x}}iq_x\right]\rho_{\boldsymbol{q}} + \frac{3}{4}\eta v\ i\mathbf{q}w^x_{\mathbf{q}} - \frac{1}{8}\eta v\ iq_x\mathbf{w}_{\mathbf{q}} - Dq^2\mathbf{w}_{\mathbf{q}} \,. \tag{2.17b}$$

For finite α, the dispersion relations of all the modes are finite at $q = 0$. A proper analysis of the linear stability of the fluctuations then requires examining the modes up to order q^4. This is cumbersome and not very enlightening. For this reason we simply present here the analysis of the case $\lambda = 0$ and $\alpha = 0$ that serves to make contact with the existing literature.

For the following discussions, we focus on the simplified case of no proliferation and constant active speed ($\alpha = 0$ and $\lambda = 0$). It is convenient to apportion the polarization in components along the direction $\hat{\mathbf{x}}$ of mean order and perpendicular to it. In addition, we only consider for simplicity wavectors $\mathbf{q}$ along these two special directions.

Longitudinal mode When $\mathbf{q} = q\hat{\mathbf{x}}$, $w^x_{\mathbf{q}}$ and $w^y_{\mathbf{q}}$ describe splay and bend deformations of the order parameter, respectively. The linearized equations are given by

$$\partial_t \rho_{\boldsymbol{q}} = -iqvw^x_{\mathbf{q}} - Dq^2\rho_{\boldsymbol{q}} \,, \tag{2.18a}$$

$$\partial_t w^x_{\mathbf{q}} = -\epsilon\eta^2 w^x_{\mathbf{q}} + \epsilon\eta\rho_{\mathbf{q}} - \frac{1}{2}iqv\rho_{\mathbf{q}} + \frac{5}{8}\eta v\ iqw^x_{\mathbf{q}} - Dq^2 w^x_{\mathbf{q}} \,, \tag{2.18b}$$

$$\partial_t w^y_{\mathbf{q}} = -\frac{1}{8}\eta v\ iqw^y_{\mathbf{q}} - Dq^2 w^y_{\mathbf{q}} \,. \tag{2.18c}$$

Bend fluctuations are decoupled and always stable. The decay of coupled density and splay fluctuations is governed by modes with dispersion relation $s_\pm(q)$,

$$s_\pm(q) = \frac{1}{2}\left(-\epsilon\eta^2 + \frac{5}{8}\eta v iq - 2Dq^2\right) \pm \frac{1}{2}\sqrt{\left(\epsilon\eta^2 - \frac{5}{8}\eta v iq\right)^2 - 4iqv\left(\epsilon\eta - \frac{1}{2}iqv\right)} \tag{2.19}$$

Notice that in the limit $\alpha = 0$, $s_-(0) = -\epsilon\eta^2$, which is non-hydrodynamic hence ignored. The linear stability of the longitudinal mode to splay fluctuations is then determined by the hydrodynamic mode $s_+(q)$, and it is sufficient to expand it to second order in q,

$$s_+(q) = -\frac{ivq}{\eta} + \left(-D + \frac{v^2}{\epsilon\eta^4} + \frac{v^2}{8\epsilon\eta^2}\right)q^2 + \mathcal{O}(q^4) \,. \tag{2.20}$$

The system is unstable when $Re[s_+] > 0$. When $D \to 0$, this condition is always satisfied. A finite D sets an upper limit for the instability

$$1 < \gamma\rho_s < \frac{v}{4}\sqrt{\frac{\epsilon}{D}} \tag{2.21}$$

Notice that the mode $s_+(q)$ has a finite imaginary part, which suggests the emergence traveling patterns in the unstable region. This longitudinal instability of splay and density fluctuations is simply the banding instability studied by Bertin *et al* [88] and by Mishra *et al* [89], although the parameters in our model have a different dependence on v_0 - in particular the alignment parameter γ does not depend on v_0.

Transverse mode If $\mathbf{q} = q\hat{\mathbf{y}}$, $\alpha = 0$ and $\lambda = 0$, then the linearized equations for the fluctuations are given by

$$\partial_t \rho_{\mathbf{q}} = -viqw^y_{\mathbf{q}} - Dq^2\rho_{\mathbf{q}} \,, \tag{2.22a}$$

$$\partial_t w^x_{\mathbf{q}} = -\epsilon\eta^2 w^x_{\mathbf{q}} + \epsilon\eta\rho_{\mathbf{q}} - Dq^2 w^x_{\mathbf{q}} \,, \tag{2.22b}$$

$$\partial_t w^y_{\mathbf{q}} = -\frac{1}{2}viq\rho_{\mathbf{q}} + \frac{3}{4}v\eta\ iqw^x_{\mathbf{q}} - Dq^2 w^y_{\mathbf{q}} \,. \tag{2.22c}$$

We first consider the region $\epsilon\eta >> 1$, deep in the ordered state. In this case we can eliminate $w^x_{\mathbf{q}}$ by neglecting the time derivative in Eq. (2.22b) to obtain

$$w^x_{\mathbf{q}} \simeq \frac{1}{\eta}\rho_{\mathbf{q}} \tag{2.23}$$

Substituting in Eqs. (2.24) and (2.24b), we obtain coupled equations for density and bend fluctuations, given by

$$\partial_t \rho_{\mathbf{q}} = -viqw^y_{\mathbf{q}} - Dq^2\rho_{\mathbf{q}} \,, \tag{2.24a}$$

$$\partial_t w^y_{\mathbf{q}} = \frac{1}{4}viq\rho_{\mathbf{q}} - Dq^2 w^y_{\mathbf{q}} \tag{2.24b}$$

The dispersion relation $s_\pm(q)$ of the eigenvalues of these equations are given by

$$s_\pm(q) = \pm\frac{vq}{2} - \frac{Dq^2}{2} \tag{2.25}$$

We see that $Re[s_-]$ is always negative. The linear stability of the polarized state to fluctuations with wave vector along y is determined by the s_+ mode, which is always unstable for $0 < q < \frac{v}{2D}$. Therefore deep in the ordered region, the polarized state is always unstable to bend fluctuations. This arises from the pressure-like term proportional to w^2 term that yields a change in sign of the effective compressibility, as discussed in Ref. [89]. It leads to patterns as shown in Fig. 2.7.

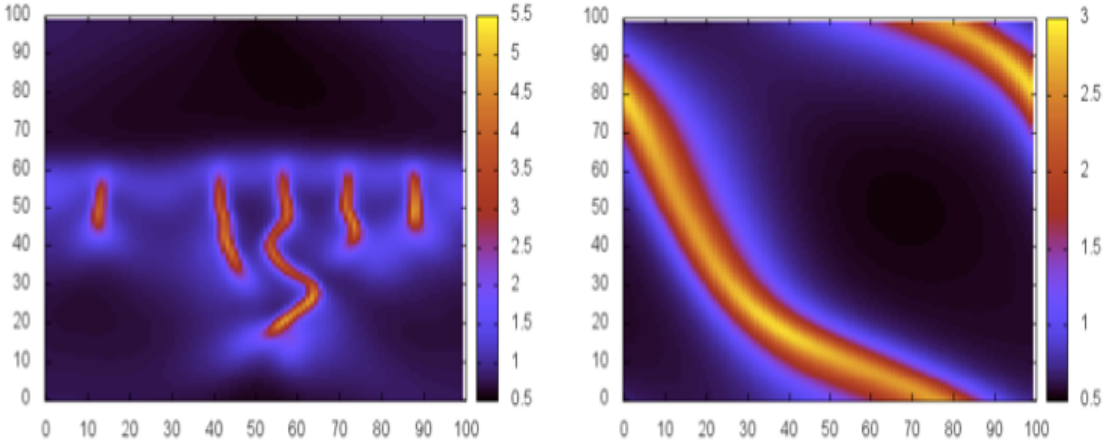

FIGURE 2.7: Patterns from transverse instability as a result of negative compressibility. Left: $\gamma = 1.025$, $D = D_w = 0.05$. Right: $\gamma = 1.67$, $D = D_w = 0.2$.

2.7 Appendix 2.C: Effect of additional nonlinearities

The continuum model considered here is a simplified version of the model obtained in Ref. [85] by coarse graining a microscopic Vicsek model with a density dependent self-propulsion speed. In Eqs. 2.1 we have neglected a number of additional advective nonlinearities that are obtained from the exact coarse graining. In this section we show that these additional nonlinear terms do not change the nature of the patterns, but simply yield small shifts in the values of parameters where each type of pattern is obtained.

Farrell *et al.* [85] considered a Vicsek-type model of point particles with density-dependent self-propulsion speed $v(\rho)$, The microscopic dynamics is governed by coupled Langevin equations of the form

$$\dot{\mathbf{r}}_i = v\hat{\mathbf{e}}_i + \boldsymbol{\eta}_i(t) \,, \tag{2.26a}$$

$$\dot{\theta}_i = -\gamma \frac{\partial U}{\partial \theta_i} + \eta_i^R(t) \tag{2.26b}$$

where $v(\rho) = v_0 \exp(-\lambda\rho)$, $\mathbf{r}_i$ is the position of active particle and $\hat{\mathbf{e}}_i$ a unit vector along the direction of self-propulsion. The microscopic dynamics includes white and Gaussian thermal and rotational noise terms, with correlations

$$\langle \eta_{i\alpha}(t)\eta_{j\beta}(t')\rangle = 2D\delta_{ij}\delta_{\alpha\beta}\delta(t-t') \,, \tag{2.27}$$

$$\langle \eta_i^R(t)\eta_j^R(t')\rangle = 2\epsilon\delta_{ij}\delta(t-t') \,. \tag{2.28}$$

the paper for $\tilde{\lambda} = 1.4$,

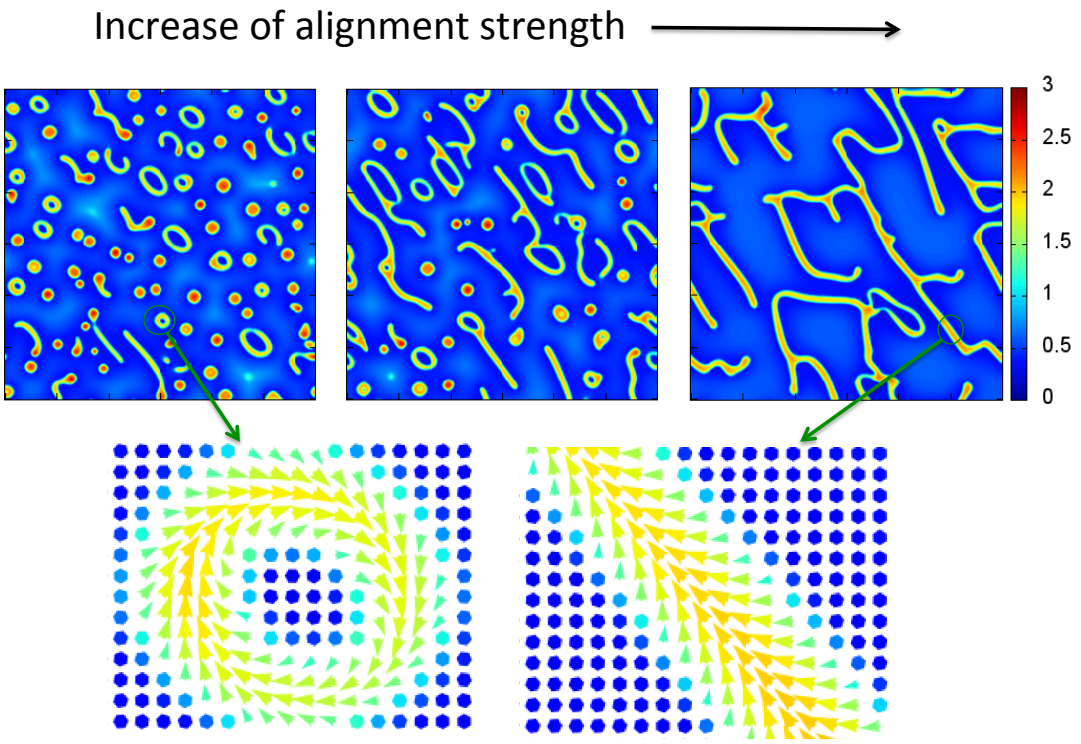

FIGURE 2.8: Heat maps of density in the polar region obtained by numerical integration of Eqs. (2.29) for $\tilde{\lambda} = 1.4$, $\tilde{\alpha} = 0.08$, $\tilde{D} = 0.01$ and (from left to right) $\tilde{\gamma} = 1.11, 1.25$ and 1.67.

Finally, $U = -\sum_{|\mathbf{r}_j - \mathbf{r}_i| \leq R} \cos(\theta_j - \theta_i)$ is the polar alignment interaction. Using standard coarse-graining, these authors derived continuum equations for density and polarization, given by (with our parameter notation)

$$\partial_t \rho = -\boldsymbol{\nabla} \cdot (v\mathbf{w} - D\boldsymbol{\nabla}\rho) + \alpha\rho\,(1 - \rho/\rho_s)\ , \tag{2.29a}$$

$$\partial_t \mathbf{w} = -\,(\epsilon - \gamma\rho)\,\mathbf{w} - \frac{\gamma^2}{2\epsilon}|\mathbf{w}|^2\mathbf{w} - \frac{\gamma}{4\epsilon}\mathbf{F}[\mathbf{w}, \boldsymbol{\nabla}\mathbf{w}] \quad -\frac{1}{2}\boldsymbol{\nabla}\left(v\rho - \frac{3\gamma}{4\epsilon}vw^2\right) + D_w\nabla^2\mathbf{w}\ , \tag{2.29b}$$

Compared to the simplified model described by Eqs. 2.1, Eqs. (2.29) contain a more complicated form for the advective nonlinearities $\mathbf{F}[\mathbf{w}, \boldsymbol{\nabla}\mathbf{w}]$, given by $\mathbf{F} = \frac{1}{2}\mathbf{w}\cdot\boldsymbol{\nabla}(v\mathbf{w}) + \frac{1}{4}v\boldsymbol{\nabla}w^2 + \frac{3}{2}\mathbf{w}\boldsymbol{\nabla}\cdot(v\mathbf{w}) + v\mathbf{w}(\nabla\cdot\mathbf{w}) + v(\mathbf{w}\cdot\boldsymbol{\nabla})\mathbf{w}$ (only the first term is included in Eqs. (1) of the paper). These additional terms have, however, little effect on the nature of the emergent patterns, but only shift the parameters where the patterns emerge, as illustrated by Fig. 2.8. The only exception is that the full form of $\mathbf{F}[\mathbf{w}, \boldsymbol{\nabla}\mathbf{w}]$ must be included to obtain the blinking dots pattern in the isotropic state.

2.8 Appendix 2.D: Amplitude equations in the isotropic state

To estimate the amplitude of the fluctuations in density and polarization near the instability boundary of the homogeneous isotropic state, we need to go beyond linear stability analysis and solve for the fluctuations perturbatively. To proceed, we neglect all the convective terms which do not play a significant role in the droplet formation in the isotropic state. The simplified equations read

$$\partial_t \rho = -\boldsymbol{\nabla} \cdot [v(\rho)\mathbf{w}] + D\boldsymbol{\nabla}^2\rho + \alpha\rho\left(1 - \frac{\rho}{\rho_0}\right), \tag{2.30a}$$

$$\partial_t \mathbf{w} = -(\epsilon - \gamma\rho)\mathbf{w} - \frac{1}{2}\boldsymbol{\nabla}\left[v(\rho)\rho\right] + D_w\boldsymbol{\nabla}^2\mathbf{w}. \tag{2.30b}$$

For this section, we use an alternative scaling similar to the one used in Ref. [13] to introduce a new set of dimensionless variables. We scale time using $1/\alpha$, length using $(D/\alpha)^{1/2}$ and hydrodynamic variables using ρ_0. This yields the following dimensionless quantities

$$\Phi = \lambda\rho_0, \qquad \tilde{v}_0 = v_0/\sqrt{D\alpha}, \qquad \tilde{\epsilon} = (\epsilon - \gamma\rho_0)/\alpha, \qquad \tilde{\gamma} = \gamma\rho_0/\alpha.$$

We drop the tildes in the following discussion for simplicity of notation. All quantities are dimensionless unless otherwise noted. We introduce perturbations $\delta\boldsymbol{u} = (\delta\rho, \delta\boldsymbol{w})$ around the homogeneous isotropic state. We then scale $\delta\boldsymbol{u}$ using Φ as

$$\hat{\Omega} = \boldsymbol{u}_p\Phi = (\Omega_\rho, \boldsymbol{\Omega}). \tag{2.31}$$

The dynamic equations for the perturbation can now be written in matrix form

$$\partial_t\hat{\boldsymbol{\Omega}} = \hat{\boldsymbol{L}}\hat{\boldsymbol{\Omega}} + \boldsymbol{N}(\hat{\boldsymbol{\Omega}}), \tag{2.32}$$

where $\hat{\boldsymbol{L}}$ is the linear operator

$$\boldsymbol{L} = \begin{pmatrix} \boldsymbol{\nabla}^2 - 1 & 0 \\ 0 & \boldsymbol{\nabla}^2 - \epsilon \end{pmatrix}, \tag{2.33}$$

and $\boldsymbol{N}(\hat{\Omega})$ is the Non-linear operator

$$\boldsymbol{N} = \begin{pmatrix} -v_0 e^{-\Phi}\boldsymbol{\nabla}\cdot\left[e^{-\Omega_\rho}\boldsymbol{\Omega}\right] - \frac{1}{\Phi}\Omega_\rho^2 \\ -\frac{v_0}{2}e^{-\Phi}\boldsymbol{\nabla}\left[e^{-\Omega_\rho}\left(1 + \frac{\Omega_\rho}{\Phi}\right)\right] + \frac{1}{\Phi}\gamma\Omega_\rho\boldsymbol{\Omega} \end{pmatrix}. \tag{2.34}$$

The instability condition in terms of the new dimensionless variables can be written as

$$\frac{v_0}{\sqrt{2}} e^{-\Phi} \sqrt{\Phi - 1} > 1 + \sqrt{\epsilon}. \tag{2.35}$$

Close to the onset of the instability, we define a small parameter that measures the distance to the transition

$$\frac{v_0 - v_c}{v_c} = x, \tag{2.36}$$

with which we rewrite the instability condition

$$\frac{v_0}{\sqrt{2}} e^{-\Phi} \sqrt{\Phi - 1} = \left(1 + \sqrt{\epsilon}\right)(x + 1). \tag{2.37}$$

Now the non-linear operator can be written as

$$\boldsymbol{N} = \begin{pmatrix} -(x+1)(1+\sqrt{\epsilon}) \sqrt{\frac{2}{\Phi - 1}} \boldsymbol{\nabla} \cdot \left[e^{-\Omega_\rho} \boldsymbol{\Omega} \right] - \frac{1}{\Phi} \Omega_\rho^2 \\ (x+1)(1+\sqrt{\epsilon}) \sqrt{\frac{1}{2\Phi - 2}} \boldsymbol{\nabla} \left[e^{-\Omega_\rho} \left(1 + \frac{\Omega_\rho}{\Phi} \right) \right] + \frac{1}{\Phi} \gamma \Omega_\rho \boldsymbol{\Omega} \end{pmatrix}. \tag{2.38}$$

Next, we expand the perturbation in terms of x

$$\hat{\Omega} = \hat{\boldsymbol{U}}_0 x^{\frac{1}{2}} + \hat{\boldsymbol{U}}_1 x + \hat{\boldsymbol{U}}_2 x^{\frac{3}{2}}, \tag{2.39}$$

where $\hat{\boldsymbol{U}}_i = (U_{i\rho}, \boldsymbol{U}_i)$. We expand $\boldsymbol{N}(\hat{\boldsymbol{\Omega}})$ up to $o(x^{\frac{3}{2}})$ and obtain

$$\boldsymbol{N}_c(\hat{\boldsymbol{\Omega}}) = \begin{pmatrix} -\hat{\epsilon} \nabla \cdot \left[A_1 x^{\frac{1}{2}} + A_2 x + (A_1 + A_3) x^{\frac{3}{2}} \right] - \frac{1}{\Phi} \left(B_2 x + B_3 x^{\frac{3}{2}} \right) \\ -\frac{\hat{\epsilon}}{2} \nabla \cdot \left[D_1 x^{\frac{1}{2}} + D_2 x + (D_1 + D_3) x^{\frac{3}{2}} \right] - \frac{1}{\Phi} \gamma \left(E_2 x + E_3 x^{\frac{3}{2}} \right) \end{pmatrix}, \tag{2.40}$$

Where $\hat{\epsilon} = 1 + \sqrt{\epsilon}$ and

$$\begin{pmatrix} 0 & A_1 & A_2 & A_3 \\ 0 & 0 & B_2 & B_3 \\ 1 & C_1 & C_2 & C_3 \\ 0 & D_1 & D_2 & D_3 \\ 0 & 0 & E_2 & E_3 \end{pmatrix}$$

$$= \begin{pmatrix} 0 & \boldsymbol{U}_0 & \boldsymbol{U}_1 - U_{0\rho}\boldsymbol{U}_0 & \boldsymbol{U}_2 - \boldsymbol{U}_{0\rho}\boldsymbol{U}_1 + \frac{U_{0\rho}^2}{2} - U_{1\rho}\boldsymbol{U}_0 \\ 0 & 0 & U_{0\rho}^2 & 2U_{0\rho}U_{1\rho} \\ 1 & U_{0\rho} & \frac{U_{0\rho}^2}{2} - U_{1\rho} & U_{0\rho}U_{1\rho} - U_{2\rho} - \frac{U_{0\rho}^3}{6} \\ 0 & \frac{U_{0\rho}}{\Phi} - U_{0\rho} & \frac{U_{1\rho} - U_{0\rho}^2}{\Phi} + \frac{U_{0\rho}^2}{2} - U_{1\rho} & \frac{U_{2\rho} - 2U_{0\rho}U_{1\rho} + \frac{U_{0\rho}^3}{2}}{\Phi} + U_{0\rho}U_{1\rho} - U_{2\rho} - \frac{U_{0\rho}^3}{6} \\ 0 & 0 & U_{0\rho}\boldsymbol{U}_0 & U_{0\rho}\boldsymbol{U}_1 + U_{1\rho}\boldsymbol{U}_0 \end{pmatrix}. \tag{2.41}$$

We are interested in the saturated time-independent amplitude of the perturbation, therefore we set the time derivatives to be zero. Now we solve the dynamic equations

perturbatively. To order $o(x^{\frac{1}{2}})$

$$\boldsymbol{L}_c\hat{\Omega} = 0, \tag{2.42}$$

where

$$L_c = \begin{pmatrix} \boldsymbol{\nabla}^2 - 1 & -\hat{\epsilon}\boldsymbol{\nabla} \\ -\frac{\hat{\epsilon}}{2}\left(\frac{1}{\Phi}\boldsymbol{\nabla} - 1\right) & \boldsymbol{\nabla}^2 - \epsilon \end{pmatrix} \tag{2.43}$$

is the linear operator near transition, which leads to the solution

$$U_{0\rho} = A_{0\rho}e^{i\boldsymbol{q}_c\cdot\boldsymbol{x}} + A^*_{0\rho}e^{-i\boldsymbol{q}_c\cdot\boldsymbol{x}} \tag{2.44a}$$

$$\boldsymbol{U}_0 = \boldsymbol{A}_0e^{i\boldsymbol{q}_c\cdot\boldsymbol{x}} + \boldsymbol{A}^*_0e^{-i\boldsymbol{q}_c\cdot\boldsymbol{x}} \tag{2.44b}$$

with

$$\boldsymbol{q}_c^2 = \sqrt{\epsilon} \qquad \boldsymbol{A}_0 = i\frac{\left(1\frac{1}{\Phi}\right)\frac{\hat{\epsilon}}{2}\boldsymbol{q}_c}{\boldsymbol{q}_c^2 + \epsilon}A_{0\rho}, \tag{2.45}$$

where $\boldsymbol{q}_c$ is the wavelength of the unstable mode right at the onset of the instability. The same relation holds for the conjugated amplitude by symmetry. Notice that the amplitude is not determined from this linear equation, thus we need to go to higher orders in the perturbation to obtain a constraint that determines the solution for the amplitude of the perturbation. In this case, we need to refer to the equations to the order of $o(x)$

$$\boldsymbol{L}_c\hat{\boldsymbol{U}}_1 = \begin{pmatrix} \frac{1}{\Phi}U_{0\rho}^2 - \hat{\epsilon}\boldsymbol{\nabla}\cdot U_{0\rho}\boldsymbol{U}_0 \\ -\frac{\hat{\epsilon}}{2}\boldsymbol{\nabla}\cdot\left(\frac{U_{0\rho}^2}{\Phi} - \frac{U_{0\rho}^2}{2}\right) - \frac{\gamma}{\Phi}U_{0\rho}\boldsymbol{U}_0 \end{pmatrix} \tag{2.46}$$

and $o(x^{3/2})$

$$\boldsymbol{L}_c\hat{\boldsymbol{U}}_2 = \begin{pmatrix} \hat{\epsilon}\boldsymbol{\nabla}\cdot\left(\boldsymbol{U}_0 - U_{0\rho}\boldsymbol{U}_1 + \frac{U_{0\rho}^2\boldsymbol{U}_0}{2} - U_{1\rho}\boldsymbol{U}_0\right) + \frac{2}{\Phi}U_{0\rho}U_{1\rho} \\ \frac{\hat{\epsilon}}{2}\boldsymbol{\nabla}\cdot\left(\frac{U_{0\rho}}{\Phi} - U_{0\rho} + \frac{\frac{U_{0\rho}^3}{2} - 2U_{0\rho}I_{1\rho}}{\Phi} + U_{0\rho}U_{1\rho} - \frac{U_{0\rho}^3}{6}\right) - \frac{\gamma}{\Phi}\left(U_{0\rho}\boldsymbol{U}_1 + U_{1\rho}\boldsymbol{U}_0\right) \end{pmatrix}. \tag{2.47}$$

Eqn. 2.46 has solution of the form

$$U_{1\rho} = B_{1\rho}e^{i\boldsymbol{q}_c\cdot\boldsymbol{x}} + B^*_{1\rho}e^{-i\boldsymbol{q}_c\cdot\boldsymbol{x}} + C_{1\rho} + D_{1\rho}e^{2i\boldsymbol{q}_c\cdot\boldsymbol{x}} + D^*_{1\rho}e^{-2i\boldsymbol{q}_c\cdot\boldsymbol{x}} \tag{2.48a}$$

$$\boldsymbol{U}_1 = \boldsymbol{B}_1e^{i\boldsymbol{q}_c\cdot\boldsymbol{x}} + \boldsymbol{B}^*_1e^{-i\boldsymbol{q}_c\cdot\boldsymbol{x}} + \boldsymbol{C}_1 + \boldsymbol{D}_1e^{2i\boldsymbol{q}_c\cdot\boldsymbol{x}} + \boldsymbol{D}^*_1e^{-2i\boldsymbol{q}_c\cdot\boldsymbol{x}}, \tag{2.48b}$$

while the solvability condition is obtained by imposing that the r.h.s of Eqn. 2.47 is orthogonal to $e^{\pm i\boldsymbol{q}_c\cdot\boldsymbol{x}}$, therefore the coefficient of $e^{\pm i\boldsymbol{q}_c\cdot\boldsymbol{x}}$ should be zero. From symmetry, we only need to consider the coefficient of $e^{i\boldsymbol{q}_c\cdot\boldsymbol{x}}$. This solvability condition yields the

amplitude equations

$$\boldsymbol{A}_0 + |A_{0\rho}|^2 \boldsymbol{A}_0 + \frac{A_{2\rho}^2 \boldsymbol{A}_0^*}{2} - \left(\boldsymbol{C}_1 A_{0\rho} + \boldsymbol{D}_1 A_{0\rho}^* + C_{1\rho}\boldsymbol{A}_0 + D_{1\rho}\boldsymbol{A}_0 *\right) = 0 \tag{2.49a}$$

$$C_{1\rho} A_{0\rho} + D_{1\rho} A_{0\rho}^* = 0 \tag{2.49b}$$

$$\left(\frac{1}{\Phi} - 1\right) A_{0\rho} + (\frac{3}{2\Phi} - \frac{1}{2})|A_{0\rho}|^2 A_{0\rho} + \left(1 - \frac{2}{\Phi}\right)\left(C_{1\rho} A_{0\rho} + D_{1\rho} A_{0\rho}^*\right) = 0 \tag{2.49c}$$

$$\boldsymbol{C}_1 A_{0\rho} + \boldsymbol{D}_1 A_{0\rho}^* + C_{1\rho}\boldsymbol{A}_0 + D_{1\rho}\boldsymbol{A}_0 * = 0 \tag{2.49d}$$

Notice we have ignored the spatial dependence of the amplitude for simplicity, and for a saturated isotropic system, this assumption is reasonable. We arrive at the final result for the saturated magnitude of the amplitude

$$|A_{0\rho}|^2 = \frac{2\left(\Phi - 1\right)}{\left(3 - \Phi\right)} \tag{2.50a}$$

$$|\boldsymbol{A}_0|^2 = \frac{\left(\Phi + 1\right)\left(1 - \frac{1}{\Phi}\right)}{\left(3 - \Phi\right)\sqrt{\epsilon}} \tag{2.50b}$$

Notice that the amplitude here is for the scaled fields, to get the amplitudes for the original fields, we need to divide the square of the amplitudes by Φ^2 following from Eqn. 2.31. Several results follow from the expression

- The squared amplitude for the density field depends only on Φ, and for Φ smaller than 1 or greater than 3 the amplitude finally decays. The former is in agreement with the linear stability analysis, and the latter is due to the restabilization at large velocity suppression.
- The squared amplitude for the polarization field depend on both Φ and ϵ, and scales as $\epsilon^{-1/2}$, which is physically reasonable, as the greater the noise, the smaller the polarization.

Chapter 3

Hydrodynamics of Turning Flocks

3.1 Introduction

The Vicsek model [22, 54] and related continuous-time variations [91] have been used to model flocking in a variety of systems, from birds [92] to cells [93] to *in vitro* cellular components [29] and synthetic swimmers [45]. These are examples of active systems, consisting of individually driven, dissipative units that exhibit coordinated motion (flocking) at large scales [15, 94]. In the Vicsek model the active units are described as point particles with overdamped dynamics carrying a velocity vector of fixed magnitude, hence "flying spins". Each spin tends to align with its neighbors, but makes errors, modeled as angular noise. Vicsek pointed out that, like magnetic spins in a material, "flying spins" exhibit a phase transition from a disordered state to a coherent moving flock as the noise is decreased or the number density is increased [22]. The existence of the transition has been put on firm grounds by a large number of numerical studies [95]. Concurrently to the original work by Vicsek, Toner and Tu proposed a continuum version of the model inspired by dynamical field theories of condensed matter systems [23, 83]. Over the past two decades both models have been applied broadly to describe self-organization and pattern formation in active systems.

Recent work [2] has suggested that the description of the observed collective turning of coherent flocks requires a modification of the Vicsek model to include angular inertia in the dynamics. This allows propagation of angular correlations through the flock on large scales via spin-wave-like excitations [55]. Such an "inertial spin model" can account for the correlated turns of large polarized groups [2]. In this paper we present a derivation of the continuum equations for a collection of inertial flying spins that generalize the Toner-Tu model to account for turning modes by incorporating the dynamics of the spin angular momentum of the flock. These equations, given in Eqs. (3.12-3.14) below, are

the first important result of our work. We note that the spin angular momentum is not a hydrodynamic field and relaxes on a finite time scale. Hence the continuum equations derived here reduce to the Toner-Tu model in the hydrodynamic limit. On the other hand, in a polarized flock the time scale over which angular momentum is dissipated due to interaction with the medium can be slower than the time over which rotational noise disrupts the order of the flock. In this case, angular inertia is important and the system can support spin waves that propagate turning information through the flock.

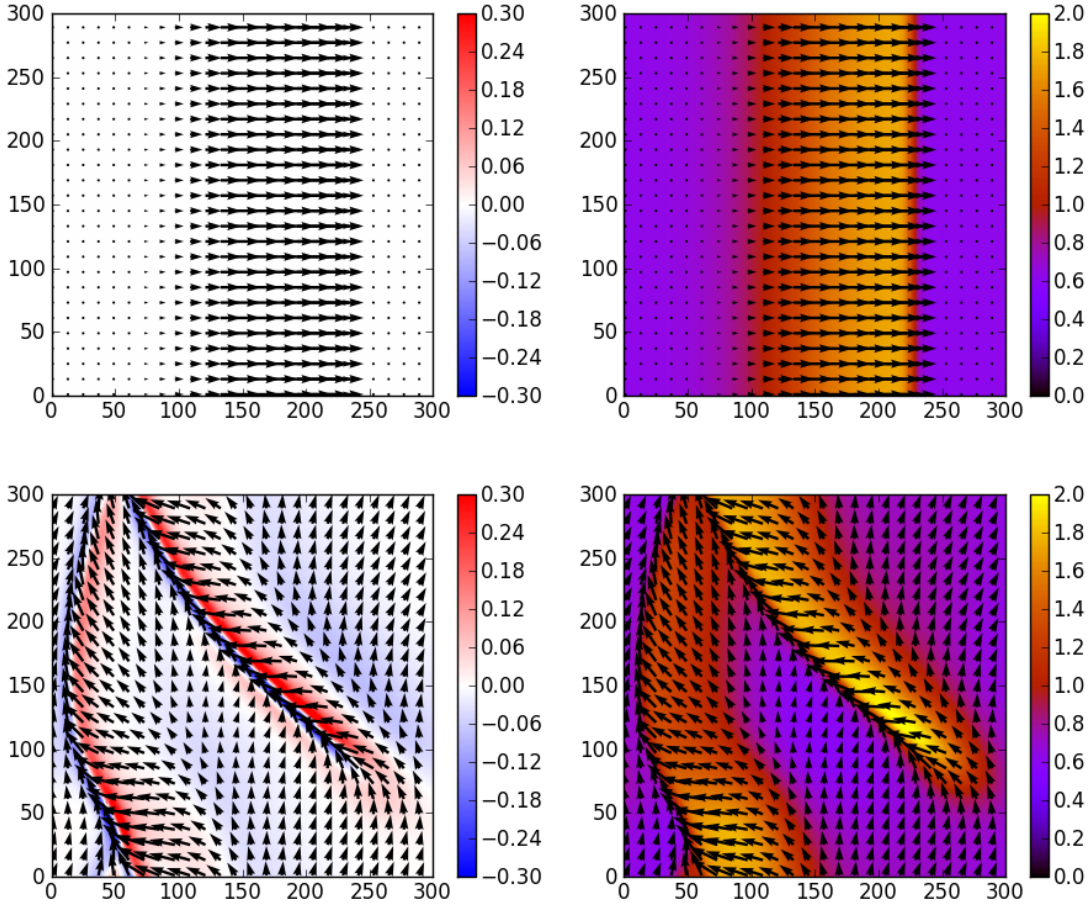

FIGURE 3.1: Emergent structures obtained via numerical solutions of Eqs. 3.12 -3.14. Left column: The color indicates the spin current density, with red (blue) corresponding to positive (negative) values and white being zero. Right column: The color indicates number density, with orange being high. The arrows represent the local polarization, with length proportional to the polarization strength. The banding state displayed in the top row lies in region B in the phase diagram Fig.3.2a, while the bottom row displays the spin-wave instability in region D, with complex spatial-temporal patterns consisting of continuously turning and swirling flocks.

By studying the continuum equations analytically and numerically, we predict a new instability of the polarized state associated with large density and spin current fluctuations that leads to complex spatio-temporal dynamics, with continuously swirling and rotating flocks. This long-wavelength instability is associated with the growth of anisotropic spin waves and is referred to as *spin-wave instability*. It arises from the growth of bend and

splay deformation augmented by the spin wave. In an equilibrium assembly of rotating particles in a fluid the damping of the local spin current is controlled by a frictional force proportional to the difference between the angular spin rate and the local vorticity of the flow [96]. In the present system the friction with the substrate breaks Galilean invariance and allows for two distinct frictional couplings, separately proportional to the spin current and to the local vorticity of the velocity/polarization field. The latter leads to the bend deformation augmented by spin wave and drives the instability. Additionally, the speed of the associated propagating spin waves is anisotropic, with faster propagation along the direction of broken symmetry than in the direction transverse to it. This leads to a new type of dynamical pattern consisting of spontaneously polarized, coherently spinning bands and flocks characterized by large fluctuations in the spin current. These structures, shown in Fig. 3.1 bottow row, are distinct from the well studied polarized bands traveling in a low density disordered background that are found ubiquitously in the Vicsek model (Fig. 3.1 top row).

The derivation of the continuum equations from a generalized Vicsek-type model yields a continuum theory that contains only two dimensionless parameters, measuring the strength of angular inertia and of alignment relative to rotational noise. This provides a great simplification over phenomenological models [24] that contain a large number of unknown parameters. The equations are studied analytically and numerically. The numerical onset of emergent patterns agrees quantitatively with the results of the linear stability analysis (Fig. 3.2a).

3.2 Active inertial spin model

Our starting point is the continuous-time model of inertial spins proposed by Cavagna *et al.* [55], where N point particles in a two-dimensional box of area L^2, with average number density $\rho_0 = N/L^2$, interact via a pairwise aligning interaction. Each particle is described by its position $\boldsymbol{r}_i$ and the direction of its velocity, identified by an angle θ_i (or a unit vector $\hat{\boldsymbol{e}}_{\theta_i} = (\cos\theta_i, \sin\theta_i)$) in 2D. The dynamics of the i-th spin is described by

$$\frac{d\boldsymbol{r}_i}{dt} = v_0 \hat{\boldsymbol{e}}_{\theta_i} \,, \qquad \frac{d\theta_i}{dt} = \frac{1}{\chi} s_i \,, \tag{3.1}$$

$$\frac{ds_i}{dt} = \gamma \sum_j F(\theta_j - \theta_i, \boldsymbol{r}_{ji}) - \frac{\eta}{\chi} s_i + \sqrt{2\epsilon}\xi_i(t) \,, \tag{3.2}$$

with $\boldsymbol{r}_{ji} = \boldsymbol{r}_j - \boldsymbol{r}_i$, v_0 the self-propulsion speed, s_i the spin angular momentum and χ the spin moment of inertia. The polar aligning coupling of strength γ is given by $F(\theta, \boldsymbol{r}) = \sin(\theta)/(\pi R^2)$ if $|\boldsymbol{r}| \leq R$ and zero otherwise, with R the range of interaction. This form of the interaction used before in the literature [85] allows us to make analytical

progress in the derivation of the continuum equations. The form of the latter is not, however, expected to depend on the specific form of the interaction. Finally, η is a friction and ϵ describes the strength of the angular noise, with $\xi_i(t)$ a Gaussian white noise with zero mean and unit variance.

On time scales large compared to the relaxation time $\tau_\eta = \chi/\eta$, one can neglect the time derivative on the left hand side of Eq. (3.2) and eliminate the spin angular momentum, s_i, from the angular dynamics. This yields a continuous-time version of the Vicsek model, with effective alignment strength γ/η and effective angular noise ϵ/η^2. We identify the spin as an internal angular momentum that generates the self-rotation, and is distinct from the angular momentum of the center of mass. A key difference between the present model and the Vicsek model [22] is that the alignment interaction and noise enter through the dynamics of the spin rather than act directly on the orientation θ.

Two additional time scales govern the dynamics of the system: the effective rotational diffusion time, $\tau_\epsilon = \frac{\eta^2}{\epsilon}$, and the alignment time, $\tau_\gamma = \frac{\eta}{\gamma\rho_0}$ with ρ_0 the average number density. Although the spin angular momentum is not conserved due to friction with the medium and relaxes on time scales τ_η, in a polarized flock with $\tau_\eta \gg \tau_\epsilon > \tau_\gamma$ such a dissipation is much slower than the time scale over which alignment is disrupted by orientational noise. A generalized hydrodynamic theory incorporating spin dynamics is therefore relevant in this regime [55].

We first examine the one-particle behavior by ignoring the alignment interaction. The spin correlation function is $< s(t)s(t') >= \frac{\chi\epsilon}{\eta} e^{-\frac{\eta}{\chi}|t-t'|}$, from which we can calculate the angular mean square displacement (MSD),

$$< \Delta\theta(t)^2 >= 2\frac{\epsilon}{\eta^2}\left[t + \frac{\chi}{\eta}e^{-\frac{\eta}{\chi}t} - \frac{\chi}{\eta}\right] , \tag{3.3}$$

that describes a damped Brownian rotor of moment of inertia χ. The angular MSD is diffusive at long times, with $< \Delta\theta(t)^2 >= 2\frac{\epsilon}{\eta^2}t$, and describes spinning particles at short times, with $< \Delta\theta(t)^2 >= \frac{\epsilon}{\chi\eta}t^2$. The translational MSD is also diffusive at long times, $< \Delta r(t)^2 >= 2\frac{v_0^2}{\epsilon/\eta^2}t$.

3.3 Derivation of continuum equations

Following standard methods [57, 97] (see Appendix 3.A), one obtain the noise-averaged Fokker-Planck equation associated with the microscopic dynamics described by Eqs. (3.1)

and (3.2), as

$$\left(\mathcal{D}_t + \frac{s}{\chi}\partial_\theta\right) P = \partial_s \left[(\eta\frac{s}{\chi} + \tau[P])P\right] + \epsilon\partial_s^2 P \,, \tag{3.4}$$

where $\mathcal{D}_t = \partial_t + v_0 \boldsymbol{e}_\theta \cdot \boldsymbol{\nabla}$ is the material derivative, $P(\boldsymbol{r}, \theta, s, t)$ is the probability density of particles at position $\boldsymbol{r}$, with velocity in direction θ and spin s at time t, and $\tau[P]$ is the aligning torque, with

$$\tau[P] = -\gamma \int_{\theta'} \int_{s'} F(\theta' - \theta) P(\boldsymbol{r}, \theta', s', t) \,. \tag{3.5}$$

For simplicity we have assumed $F(\theta, \boldsymbol{r}) = \delta(\boldsymbol{r}) \sin(\theta)$, neglecting the difference in position of the interacting pair.

We describe the large-scale dynamics of a few coarse-grained fields that vary slowly relative to microscopic time scales. For polarized flocks in addition to the density, $\rho(\boldsymbol{r}, t)$, of active units and their polarization current density, $\boldsymbol{w}(\boldsymbol{r}, t)$, we include the spin angular momentum density, $S(\boldsymbol{r}, t)$. These are obtained from the probability density P as

$$\begin{pmatrix} \rho(\boldsymbol{r}, t) \\ \boldsymbol{w}(\boldsymbol{r}, t) \\ S(\boldsymbol{r}, t) \end{pmatrix} = \int_\theta \int_s \begin{pmatrix} 1 \\ \hat{\boldsymbol{e}}_\theta \\ s \end{pmatrix} P(\boldsymbol{r}, \theta, s, t) \,. \tag{3.6}$$

To derive the continuum equations, we note that in the absence of interactions and self-propulsion, the steady state solution of Eq. (3.4) has the form of a Maxwell-like distribution $P_0(s) = (2\pi\chi k_B T_{eff})^{-1/2} \exp[-s^2/(2\chi k_B T_{eff})]$, with an effective temperature $k_B T_{eff} = \epsilon/\eta$. In a thermal system the rotational noise ϵ and the friction η would be related via the fluctuation-dissipation theorem, with $\epsilon = \eta k_B T$. Following established methods [98], we then expand the probability distribution function in terms of a set of orthonormal functions $\phi_n(s)$ as

$$P(\boldsymbol{r}, \theta, s, t) = \phi_0(s) \sum_{n=0}^{\infty} p_n(\boldsymbol{r}, \theta, t) \phi_n(s) \,, \tag{3.7}$$

where $\{\phi_n(s)\}$ are related to Hermite polynomials $H_n(x) = \left(2x - \frac{d}{dx}\right)^n \cdot 1$ as

$$\phi_n(s) = H_n(s/\sqrt{2}s_0)[P_0(s)]^{1/2}/\sqrt{n!2^n} \,, \tag{3.8}$$

with $s_0 = \sqrt{\epsilon\chi/\eta}$. This yields a hierarchy of equations for $p_n(\boldsymbol{r}, \theta, t)$, given by

$$\mathcal{D}_t p_n = -\frac{\eta}{\chi} n p_n - \sqrt{n+1}\mathcal{D}_\theta p_{n+1} - \sqrt{n}\hat{\mathcal{D}}_\theta p_{n-1}, \tag{3.9}$$

where $\mathcal{D}_\theta = (s_0/\chi)\partial_\theta$ and $\hat{\mathcal{D}}_\theta = (s_0/\chi)\partial_\theta + \tau[p_0]/s_0$ are differential operators. The torque τ only depends on the zero-th order moment, with $\tau[p_0] = -\gamma \int_{\theta'} F(\theta' - \theta) p_0(\boldsymbol{r}, \theta', t)$. Again, for times long compared to χ/η, a closed equation is obtained by retaining only the zero-th order moment. To include the effect of angular inertia, we construct closed equations for the angular probability distribution density $c(\boldsymbol{r}, \theta, t) = p_0(\boldsymbol{r}, \theta, t)$ and the associated rotational current density $j(\boldsymbol{r}, \theta, t) = p_1(\boldsymbol{r}, \theta, t)$, by neglecting $\partial_t p_2$ in the equation for p_2 and assuming $p_n = 0$ for all $n \geq 3$. The equations for the Fourier amplitudes of the first two moments, $c_k(\boldsymbol{r}, t) = \int_{-\pi}^{\pi} c(\boldsymbol{r}, \theta, t) e^{ik\theta} d\theta$ and $j_k(\boldsymbol{r}, t) = \int_{-\pi}^{\pi} j(\boldsymbol{r}, \theta, t) e^{ik\theta} d\theta$, are given by

$$\partial_t c_k + \frac{v_0}{2}\nabla^* c_{k+1} + \frac{v_0}{2}\nabla c_{k-1} = \frac{ik}{\chi} j_k \,, \tag{3.10}$$

$$\begin{aligned} \partial_t j_k + \frac{v_0}{2}\nabla^* j_{k+1} + \frac{v_0}{2}\nabla j_{k-1} &= -\frac{\eta_k}{\chi} j_k + \frac{ik\epsilon}{\eta} c_k \\ + \frac{ik\gamma}{2\pi\eta} \sum_m j_{k-m} F_{-m} c_m &+ \frac{\gamma}{2\pi} \sum_m c_{k-m} F_{-m} c_m \,, \end{aligned} \tag{3.11}$$

where $\nabla = \partial_x + i\partial_y$, $\nabla^* = \partial_x - i\partial_y$ and we have introduced an effective friction $\eta_k = \eta + k^2\epsilon\chi/\eta^2 = \eta\left(1 + k^2\tau_\eta/\tau_\epsilon\right)$. The only nonzero amplitude of the chosen interactions are $F_{\pm 1} = \pm i\pi$. The low order Fourier coefficients are simply related to the hydrodynamic fields defined in Eq. (3.6), with $c_0(\boldsymbol{r}, t) = \rho(\boldsymbol{r}, t)$, $c_1(\boldsymbol{r}, t) = w_x(\boldsymbol{r}, t) + i w_y(\boldsymbol{r}, t)$ and $j_0(\boldsymbol{r}, t) = S(\boldsymbol{r}, t)$.

Finally, we generalize the closure described in Refs. [88, 95] to neglect higher order moments and express j_1 and c_2 in terms of c_0, c_1 and j_0 up to the first order in χ/η (see Appendix 3.B), to obtain a closed set of hydrodynamic equations for ρ, $\boldsymbol{w}$ and $\boldsymbol{S} = S\hat{\boldsymbol{z}}$. To minimize the number of parameters, we nondimensionalize the equations by scaling time with $\tau_\epsilon = \eta^2/\epsilon$, length with v_0/τ_ϵ and density with ρ_0. The resulting equations are controlled by only two dimensionless parameters $\tilde{\chi} = \tau_\eta/\tau_\epsilon$ and $\tilde{\gamma} = \tau_\epsilon/\tau_\gamma$. For simplicity, we drop the tildes and all parameters are dimensionless in the following discussion unless otherwise noted [1].

$$\frac{\partial \rho}{\partial t} = -\boldsymbol{\nabla} \cdot \boldsymbol{w} \,, \tag{3.12}$$

$$\begin{aligned} \mathcal{D}_t^w \boldsymbol{w} = &-\left[\alpha(\rho) + \beta|\boldsymbol{w}|^2\right]\boldsymbol{w} - \frac{1}{2}\boldsymbol{\nabla}\rho + \lambda_2 \boldsymbol{w}(\boldsymbol{\nabla}\cdot\boldsymbol{w}) \\ &+\Omega_1 \boldsymbol{S}\times\boldsymbol{w} + \Omega_2 \boldsymbol{\nabla}\times\boldsymbol{S} + D_w\nabla^2\boldsymbol{w} \,, \end{aligned} \tag{3.13}$$

$$\begin{aligned} \mathcal{D}_t^s \boldsymbol{S} = &-\boldsymbol{\nabla}\times\left[\left(\alpha(\rho) + \beta|w|^2\right)\boldsymbol{w}\right] + \Omega_3 \boldsymbol{w}\times\nabla^2\boldsymbol{w} \\ &-\lambda_s(\boldsymbol{\nabla}\cdot\boldsymbol{w})\boldsymbol{S} - \xi\boldsymbol{S} + D_s\nabla^2\boldsymbol{S} \,, \end{aligned} \tag{3.14}$$

[1] An alternative closure proposed in [45] yields continuum equations with the same structure as those obtained here, but with $\beta = \gamma/(2\eta\rho_0)$.

where $\mathcal{D}_t^w = \partial_t + \lambda_1 \boldsymbol{w}\cdot\boldsymbol{\nabla}$ and $\mathcal{D}_t^s = \partial_t + \lambda_s \boldsymbol{w}\cdot\boldsymbol{\nabla}$ are convective derivatives. The term $\nabla|w|^2$ has been neglected here because it leads to an spurious instability through the fluctuations in the magnitude of polarization as discussed in Ref.[89]. This instability has not been observed in the particle simulations we performed. The various dimensionless parameters are

$$\alpha(\rho) = \frac{1}{1+\chi}(1-\frac{\gamma\rho}{2}), \beta = \frac{1}{1+\chi}\frac{\gamma^2}{8},$$
$$\Omega_1 = \frac{\chi\gamma}{2(1+\chi)}, \Omega_2 = \frac{\chi}{2(1+\chi)}, \Omega_3 = \frac{\gamma}{16}(\frac{1+4\chi}{1+\chi}),$$
$$\lambda_1 = \frac{\gamma}{4} - \frac{\gamma}{16}(\frac{1+4\chi}{1+\chi}), \lambda_2 = -\left[\frac{\gamma}{4} + \frac{\gamma}{16}(\frac{1+4\chi}{1+\chi})\right],$$
$$\lambda_s = \frac{\chi\gamma}{2(1+\chi)}, \xi = \frac{1}{\chi}, D_w = \frac{1+4\chi}{16}, D_s = \frac{\chi}{2(1+\chi)}.$$

As in the Toner-Tu model, the vector field $\boldsymbol{w}$ plays the dual role of polarization density and flow velocity. In equilibrium systems of rotors both the equations for the spin and the velocity field $v_0\boldsymbol{w}$ would contain dissipative couplings describing friction with the substrate proportional to the combination $\boldsymbol{S}/\chi - \frac{v_0}{2}\boldsymbol{\nabla}\times\boldsymbol{w}$, describing the fact that the angular velocity $\boldsymbol{S}/\chi$ and the vorticity $\frac{v_0}{2}\boldsymbol{\nabla}\times\boldsymbol{w}$ must be equal when the whole system is rotating as a rigid body [96, 99]. In the nonequilibrium system considered here, in contrast, frictional terms proportional to angular velocity and vorticity will in general appear with different coefficients. The first term on the right hand side of Eq. (3.14) has in fact a natural interpretation of a nonlinear, velocity-dependent vortical friction. We show in Appendix 3.C that the present equations, with the exception of the advective terms, can also be written in terms of an effective free energy. This procedure yields, however, artificial constraints on the various parameters.

Equations (3.12-3.14) augment the flocking model of Toner and Tu [23] by incorporating the dynamics of the spin current. The most important coupling between polarization $\boldsymbol{w}$ and spin current $\boldsymbol{S}$ is provided by a "self-spinning" term $\boldsymbol{S}\times\boldsymbol{w}$ that couples the center-of-mass motion to the turning dynamics. In contrast to more familiar systems of passive rotors [99, 100], in the self-propelled particle model considered here, these two degrees of freedom are coupled because the spinning angle also controls the direction of translational motion [55]. This self-spinning term, when combined with the elasticity term $\boldsymbol{w}\times\nabla^2\boldsymbol{w}$, gives rise to traveling spin waves. Finally, when $\boldsymbol{S}$ is neglected, Eqs. (3.12-3.14) reduce to the Toner-Tu equations as derived by Farrell *et al.* [85] (but in the case of constant self-propulsion speed) [2]. We expect these equations will provide useful

[2] If we neglect $\partial_t\boldsymbol{S}$ in Eq. (3.14) and use the resulting equations to eliminate $\boldsymbol{S}$ in favor of ρ and $\boldsymbol{w}$, the resulting continuum equations have the same structure as those obtained in [85], with $\mathcal{O}(\tau_\eta/\tau_\epsilon)$ corrections to various coefficients.

to describe a number of active systems where collective turning controls the large-scale dynamics.

3.4 Steady states and linear stabilities

The homogeneous steady states of the continuum equations have uniform density, $\rho = 1$, and zero mean value of the spin, $\boldsymbol{S} = 0$. As in the Vicsek model with no angular inertia, there are two such states: an isotropic state, with $\boldsymbol{w} = 0$, and a polarized or flocking state, with $\boldsymbol{w} = w_0\hat{\boldsymbol{x}}$ and $w_0 = \sqrt{-\alpha_0/\beta}$, where $\alpha_0 = \alpha(\rho = 1)$ and we have chosen the $\hat{\boldsymbol{x}}$ axis along the direction of spontaneously broken symmetry. The isotropic state is always stable. We examine below the linear stability of the polarized state by considering the dynamics of fluctuations. We let $\boldsymbol{w} = w_0\hat{\boldsymbol{x}} + \delta\boldsymbol{w}$, $\rho = 1 + \delta\rho$, $\boldsymbol{S} = \hat{\boldsymbol{z}}\delta s$ and introduce Fourier amplitudes $(\delta\rho, \delta\boldsymbol{w}, \delta s) = \sum_{\boldsymbol{q}}(\rho_{\boldsymbol{q}}, \boldsymbol{w}_{\boldsymbol{q}}, s_{\boldsymbol{q}})e^{i\boldsymbol{q}\cdot\boldsymbol{r}+\sigma t}$ to obtain a set of linearized equations in Fourier space (see Appendix B).

3.4.1 Longitudinal modes: banding instability

We first consider the dynamics of fluctuations with spatial variations along the direction of broken symmetry by letting $\boldsymbol{q} = q\hat{\boldsymbol{x}}$. In this case, $w^y_{\boldsymbol{q}}$ and $s_{\boldsymbol{q}}$ decouple from $\rho_{\boldsymbol{q}}$ and $w^x_{\boldsymbol{q}}$.

The coupled linear dynamics of fluctuations in the density and the magnitude of polarization ($w^x_{\boldsymbol{q}}$) is unaffected by angular inertia and is controlled by a stable relaxational mode and a propagating mode given by

$$\sigma_b(q) = \frac{i\alpha_\rho}{2\beta w_0}q + \frac{1}{2\alpha_0}\left[\frac{\lambda\alpha_\rho}{2\beta} + \frac{1}{2} + \frac{\alpha_\rho^2}{4\beta\alpha_0}\right]q^2 + \mathcal{O}(q^3)\,, \tag{3.15}$$

where $\alpha_\rho = \partial_\rho\alpha$ and $\lambda = \lambda_1 - \lambda_2$. This mode is unstable when $\gamma < 8/3$. This instability is well known in Vicsek and Toner-Tu models as banding instability and has been discussed extensively [88, 89, 101]. It signals the onset of alternating bands of ordered and disordered regions extending in the direction normal to that of mean order and traveling along the direction of broken symmetry. These bands have been observed in simulations of the Vicsek model [102], as well as in numerical solutions of the nonlinear hydrodynamic equations for polar fluids [88, 89]. This instability arises from the density dependence of the polarization damping $\alpha(\rho)$ and sets in right at the onset of the polarized state. Although the details of the instability and resulting emergent patterns depend on the polar or nematic symmetry of the ordered state, the existence of such an instability has been shown to be a generic property of 'dry' active systems where the parameter that

tunes the order-disorder transition, namely the density, is also dynamically coupled to the order parameter [103].

The coupled dynamics of spin and bending fluctuations ($w_{\boldsymbol{q}}^{y}$) gives rise to finite-wavelength spin waves that mediate the propagation of turning information throughout the flock. Propagating spin waves are a unique feature of the present model and their existence has been demonstrated on the basis of general arguments [55] and phenomenological continuum models [24]. Such spin waves arise in polarized flocks from the interplay between the elastic restoring forces associated with bend deformations and angular inertia, provided the dissipation of angular momentum is slow compared to both the time scales controlling angular noise and alignment interaction. Our work yields an expression for the wave speed in terms of the microscopic parameters of the model. Neglecting convection and diffusion, the spin-wave dispersion relation is given by

$$\sigma_{l\pm} = -\frac{\xi}{2} \pm ic_s q\sqrt{1-[\xi/(2c_s q)]^2}\ . \tag{3.16}$$

with wave speed $c_s = w_0\sqrt{\Omega_1\Omega_3}$. Longitudinal propagating spin waves only exist for wave vector $q > \xi/2c_s$, defining the characteristic length scale over which the wave can travel before being dissipated through frictional coupling to the substrate.

3.4.2 Transverse modes: spin-wave instability

Next we consider the dynamics of fluctuations with spatial variations transverse to the direction of broken symmetry, corresponding to $\boldsymbol{q} = q\hat{\boldsymbol{y}}$. In this case all four equations are coupled. Two of the modes are stable and relaxational and will not be discussed further. The other two modes are propagating. When calculated in a small wave vector expansion, the dispersion relations are given by

$$\sigma_t^{\pm}(q) = ic_t^{\pm}q - \mathcal{D}_{sw}q^2 + \mathcal{O}(q^3)\ , \tag{3.17}$$

with transverse wave speed $c_t = 1/\sqrt{2}$ and damping controlled by an effective diffusion constant $\mathcal{D}_{sw}$, given by

$$\mathcal{D}_{sw} = \frac{D_w}{2} + \frac{w_0^2\Omega_1(\lambda_2+\Omega_3)}{2\xi} - \frac{\Omega_1\alpha_\rho}{4\beta\xi} \tag{3.18}$$

The damping rate $\mathcal{D}_{sw}$ can become negative when

$$2\beta w_0^2\lambda_2 < \alpha_\rho - (2D_w\beta\xi)/\Omega_1 - 2\beta w_0^2\Omega_3, \tag{3.19}$$

yielding unstable growth of long wavelength polarization and spin fluctuations in the direction transverse to the direction of broken symmetry. In terms of our dimensionless parameters the instability condition reads $\gamma > (1+4\chi)(1+\chi)/(8\chi^2)+4$. This transverse instability is driven by the bend $-\beta\boldsymbol{\nabla}(|w|^2\boldsymbol{w})$ and splay $\lambda_2\boldsymbol{w}(\boldsymbol{\nabla}\cdot\boldsymbol{w})$ deformation augmented by the spin wave $\Omega_1\boldsymbol{S}\times\boldsymbol{w}$. The terms on the RHS of the instability condition 3.19 represent the stabilizing effects from density-dependent alignment interaction, rotational diffusion and spin elasticity that favor a homogeneous polar state. This long-wavelength instability of the ordered state is a new result of our work and will be referred to as spin-wave instability. As shown below, it leads to a complex spatio-temporal dynamics with large density and spin fluctuations characterized by continuously turning and swirling flocks and anisotropic propagating spin waves (see Fig. 3.1 bottom row). Particle simulations based on the inertial spin model 3.1-3.2 verifies the existence of this instability.

We note, however, that this instability disappears deep in the polar state for $\gamma > 50$ and is replaced by a homogeneous flocking state as observed from the particle simulation. In this region, the hydrodynamic equations 3.12-3.14 no longer hold, and a new closure [45] is used to derive an alternative set of hydrodynamic equations for this regime (See Appendix 3.B). The new equations are free of instabilities deep in the polar state, and successfully reproduce the homogeneous flocking state. They serve as the foundation to study the propagation of information in well-polarized flocks, a subject left for future study.

By carrying out the small wave vector expansion of the dispersion relation Eq (3.17) up to fourth order in q we can identify the wave vector q_c of the fastest growing mode corresponding to the maximum of $Re[\sigma_t^{\pm}(q)]$ shown in Fig. 3.2c and d for various values of γ and χ. This defines a characteristic length scale $\lambda_c \sim 1/q_c$ that diverges close to the transition. This length scale is inversely proportional to γ and displays a non-monotonic dependence on χ, as highlighted in Fig.3.2b. The figure shows the isolines of q_c in the plane of γ and χ, with the color indicating the magnitude of q_c, which sets the characteristic length scale of the turning flocks.

To gain more insight on the complex spatio-temporal structures that emerge in the unstable regions of parameter and confirm the results of the linear stability analysis, we have solved numerically Eqs. (3.12-3.14) on a 300×300 grid, with grid size 0.1 and periodic boundary conditions. The integration is carried over 200000 time steps using predictor-corrector method, with each time step 0.002. The system was initialized in the polarized state with small superimposed perturbations. The results are summarized in the phase diagram of Fig.3.2a. The squares in Fig.3.2a correspond to the onset of spatially varying states characterized by mean density fluctuations $\Delta\rho > 0.01$,

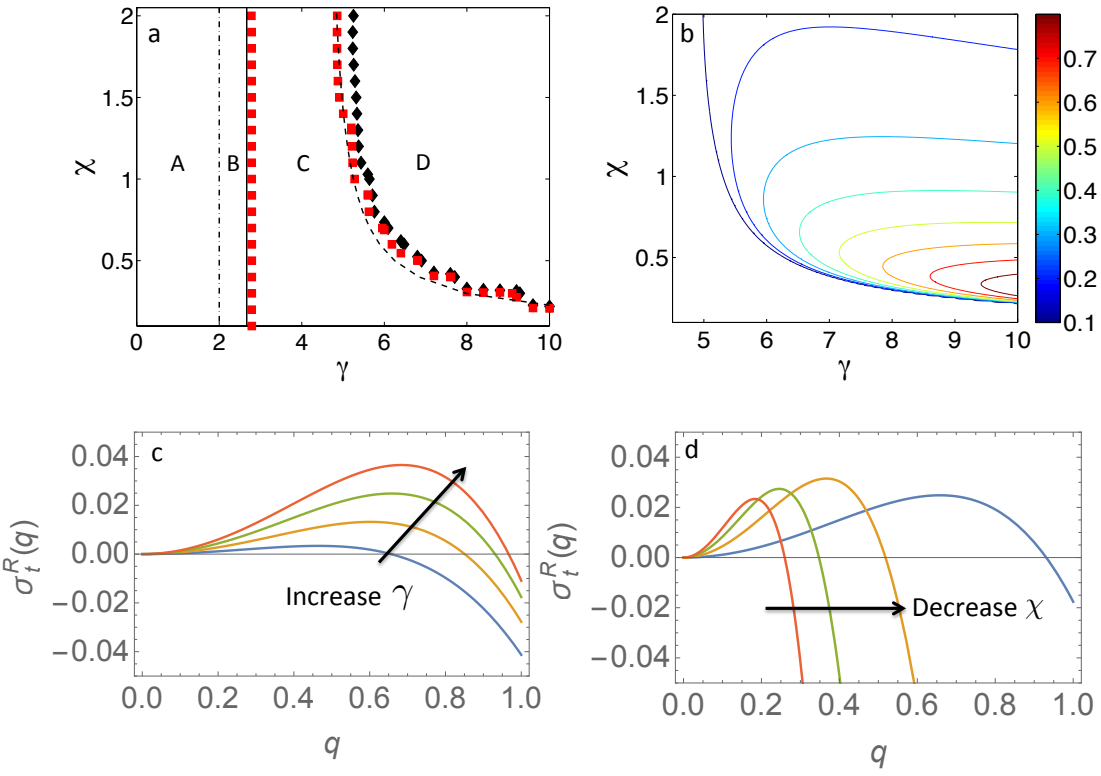

FIGURE 3.2: a. Phase diagram in the plane of dimensionless γ and χ. Labels A to D correspond to isotropic state, banding state, uniformly polarized state and spin-wave instability, respectively. b. Contour plot for the wave number q_c of the most unstable mode in the transverse direction. c. Real part of the dispersion relation of the transverse mode $\sigma_t^{\pm}$ at $\chi = 1$ and $\gamma = 7.0, 8.0, 9.0, 10.0$. d. Real part of the dispersion relation of the transverse mode $\sigma_t^{\pm}$ at $\gamma = 9$ and $\chi = 0.5, 1.0, 1.5, 2.0$.

where $\Delta\rho = \sqrt{\frac{1}{N}\sum_{\mathbf{r}} < (\rho(\boldsymbol{r}) - \rho_0)^2 >}/\rho_0$ with N the number of grid points. Similarly, the squares correspond to the onset of spin waves as characterized by spin fluctuations $\Delta S = \sqrt{\frac{1}{N}\sum_{\mathbf{r}} < (S(\boldsymbol{r}) - < S >)^2 >} > 0.01$. These criteria are in quantitative agreement with the boundaries of linear stability shown in Fig.3.2a. The system transits from an isotropic state (A) with zero mean polarization to a polarized banding state (B) above the disorder-order phase transition at $\gamma = 2$. Above $\gamma = 8/3$, the banding state is replaced by a uniformly polarized state (C) until spin-wave instability (D) sets in above the black dashed line deep in the polarized state. States B and D are shown in Fig. 3.1.

3.5 Anisotropic spin waves

To understand the nature of the spin waves that mediate the transfer of turning information within the flock, we study the propagation of the spin waves numerically with Eqs. (3.12-3.14) by initializing the system in the isotropic and uniformly polarized state, respectively, with concentrated spin current at the center (Fig. 3.3). In the isotropic state at $\gamma = 0.5$ and $\chi = 2.0$, the spin current diffuses isotropically and dissipates

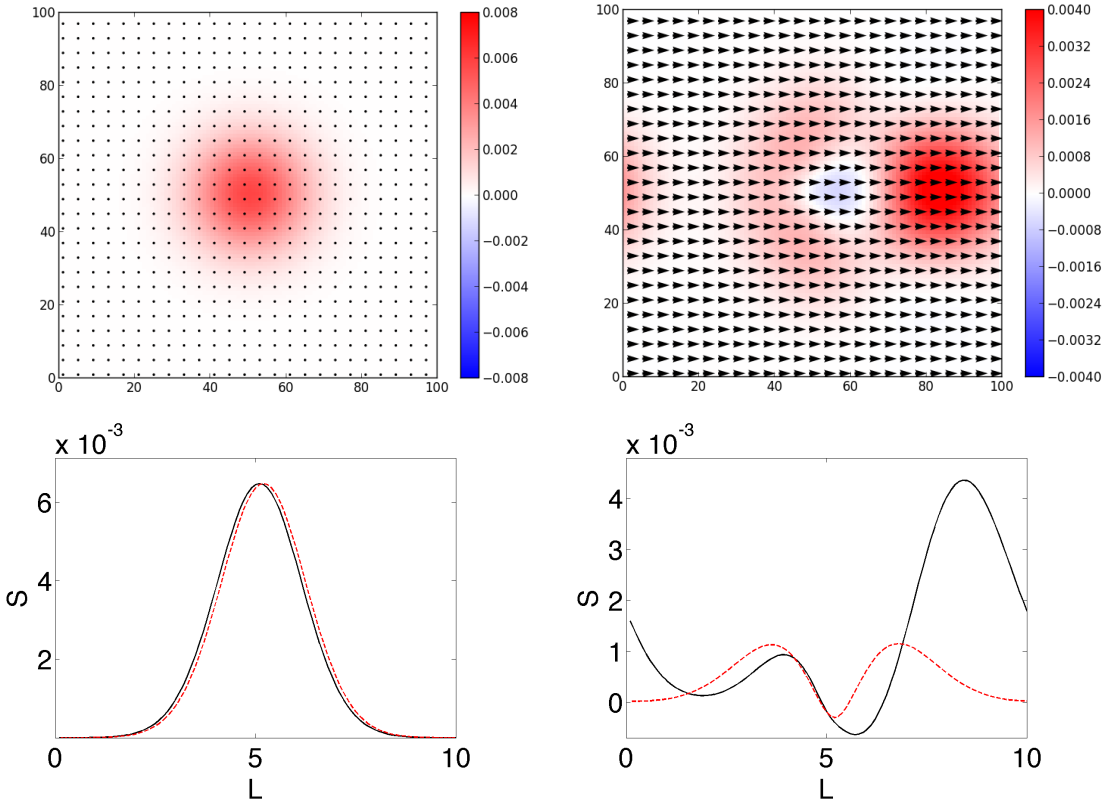

FIGURE 3.3: Top row: Snapshots of the transient diffusion (left) and propagation of spin current (right) in the isotropic state with $\gamma = 0.5$ and polarized state with $\gamma = 7.0$, respectively. $\chi = 2.0$. The system is initialized with concentrated spin current at the center and evolves for 800 time steps. Bottom row: Time-dependent distribution of spin current in the longitudinal (black solid lines) and transverse (red dashed lines) directions of mean polarization in correspondence to the snapshots. The spin wave propagates anisotropically with enhanced wave speed in the direction of mean polarization.

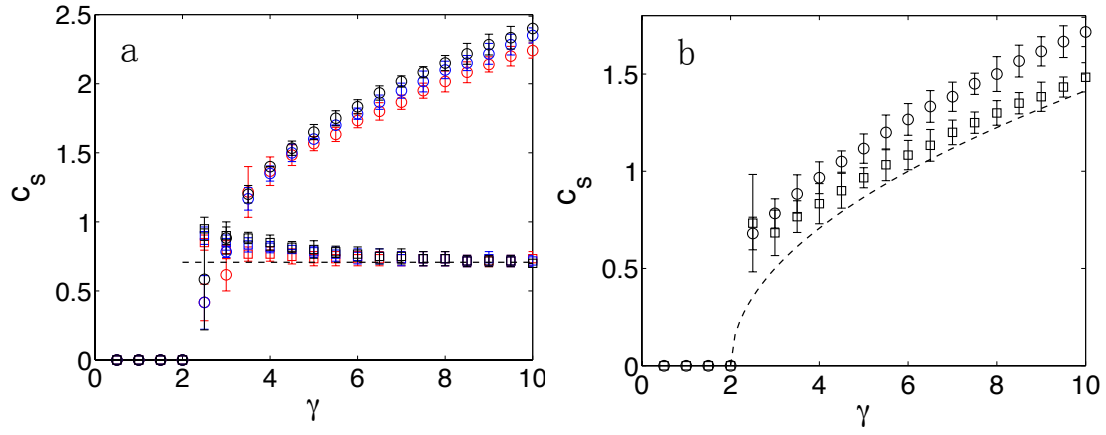

FIGURE 3.4: a. Speed of spin waves in the polarized state as a function of alignment strength γ for $\chi = 1.0, 1.5, 2.0$ (red, blue, black) in the longitudinal (circles) and transverse (squares) directions of the mean polarization obtained with perturbations in all fields. Dashed line is the transverse speed c_t in Eqn.3.17. b. Speed of spin waves with suppressed fluctuations in $\delta\rho$ and δw_x. Dashed line is the wave speed c_s in Eqn. 3.16. The system is evolved for 5000 time steps.

over time. In the polarized state at $\gamma = 7.0$ and $\chi = 2.0$, the spin current propagates anisotropically in the form of spin waves. The observation is supported by the plot of the time-dependent distribution in the longitudinal (black solid lines) and transverse (red dashed lines) directions of mean polarization in Fig. 3.3. The propagation speed is augmented in the direction of mean polarization.

Finally, we measure the speed of spin waves along (c_x) and perpendicular to (c_y) mean polarization as a function of alignment strength γ for various χ by tracing the displacement of the maxima of the distribution, and plot the results in Fig. 3.4a. The longitudinal speed c_x (circles) increases with the strength of alignment interaction while the transverse speed c_y (squares) stays approximately constant over the range of parameters.

In the longitudinal direction, where δw_y and δs decouple from δw_x and $\delta\rho$, Eqn.3.16 captures the trend of c_x except for a systematic enhancement by convection, suggesting that the longitudinal spin wave is governed by a damped wave equation at finite wavelength. In the transverse direction, all fluctuations are coupled, leading to the failure of Eqn.3.16, and the dynamics is governed at long wavelength by a hydrodynamic mode that arises from the coupling between spin current density and local vorticity through density-dependent friction. This mode has an angular-dependent propagating speed of the form

$$c_s^{\pm}(\theta) = \frac{\alpha_\rho \cos(\theta) \pm \sqrt{\alpha_\rho^2 \cos^2(\theta) + 8\beta^2 w_0^2 \sin^2(\theta)}}{4\beta w_0}, \tag{3.20}$$

that reduces to $c_t = 1/\sqrt{2}$ in the transverse direction at $\theta = \pi/2$ as in Eqn.3.17, and fits the data quantitatively in Fig.3.4a. This is also the mode that drives the spin-wave instability through the interplay between density and bending fluctuations deep in the polarized state as illustrated by Eqn.3.17.

To support this argument, we suppress fluctuations in δw_x and $\delta\rho$ as well as convections in the numerical solutions. The directional anisotropy in wave speed is significantly reduced as displayed in Fig.3.4b. In this case, both c_x and c_y agrees with the prediction by Eqn.3.16 derived from the coupled equations of δw_y and $\delta\rho$. This is the second central result of our work, and we call for experiments and particle simulations to check this prediction.

3.6 Finite-size turning flocks

Next, we explore the finite size effect by solving the hydrodynamic equations numerically in the polarized state with initially concentrated spin current at the center for different inertia, alignment strength and system sizes. We measure the average turning angle of the polarization after 2000 time steps, and plot a phase diagram in the plane of χ and γ (Fig. 3.5). The phase boundaries are drawn at where the average turning angle is 20 degrees, above which the collective turning is considered substantial. Consistent with the results from the previous section, the average turning angle increases with alignment strength and inertia, and is inversely proportional to the system size due to dissipation over large distance. This simulates the collective turning behavior initialized by individuals in a small to mid-sized flock, in agreement with particle simulations in Ref. [55].

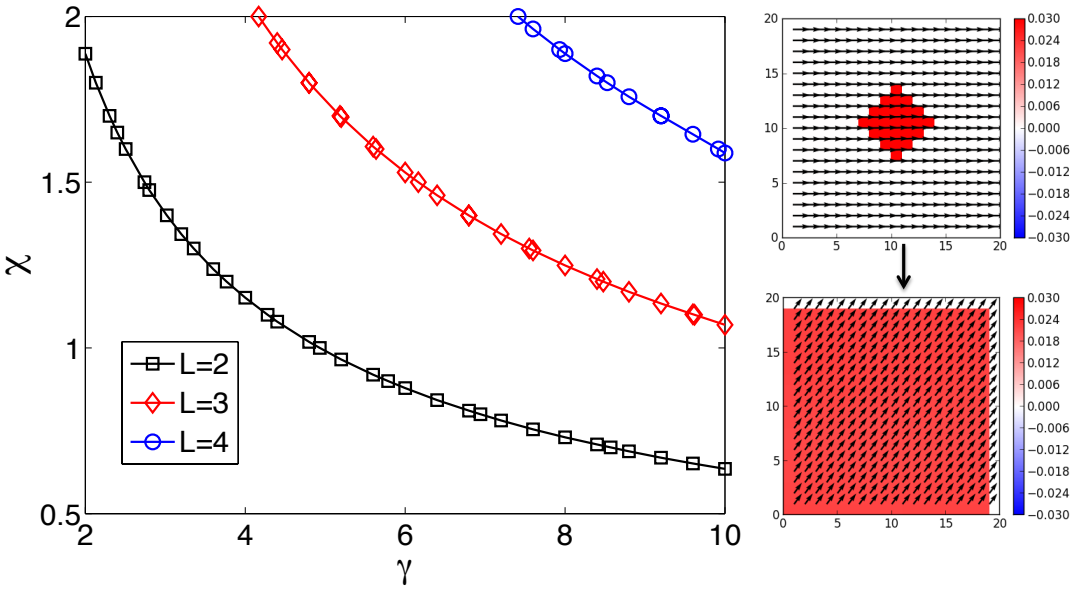

FIGURE 3.5: Phase diagram of collective turning in well-polarized flock of different sizes mediated by spin wave. The spin current is initialized at the center of the system and evolved for 2000 time steps. The lines and markers correspond to the boundaries drawn at where the average turning angle is 20 degrees. The collective turning is substantial above the lines and reduces as the system size increases due to dissipation.

3.7 Particle simulations

Finally, we perform a preliminary particle simulation based on the inertial spin model to check the hydrodynamic theory. For comparison, we simulate the continuous time Vicsek model in parallel. The results are summarized in Fig. 3.6 and 3.7.

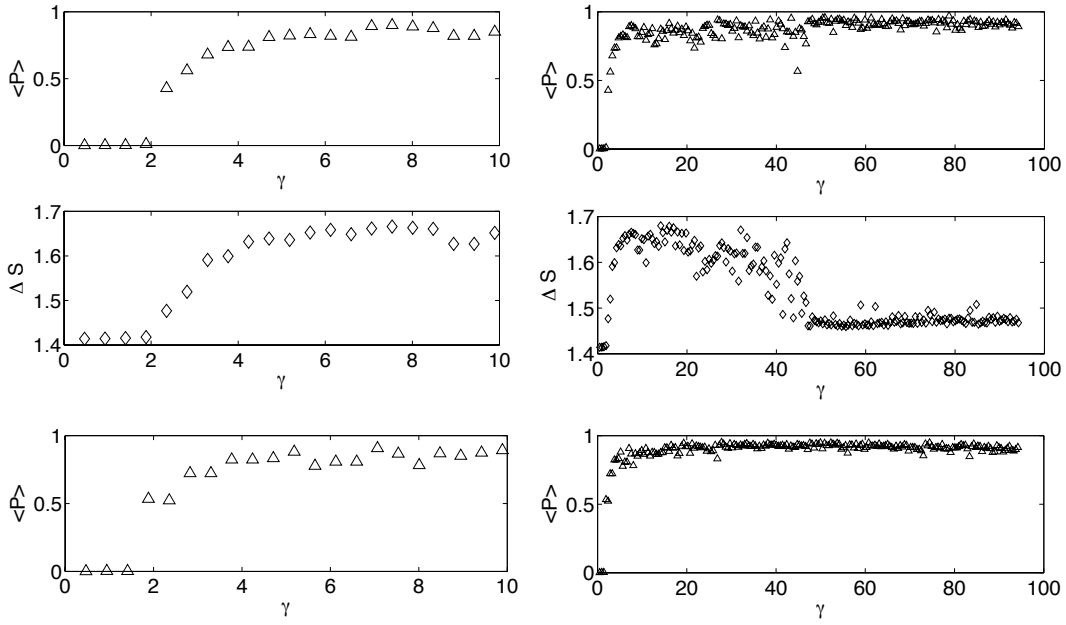

FIGURE 3.6: Order parameters as function of dimensionless alignment strength. Top/Mid row: average polarization/variance of spin from the simulation of the inertial spin model. $\chi = 1$. Bottom row: average polarization from the simulation of continuous time Vicsek model.

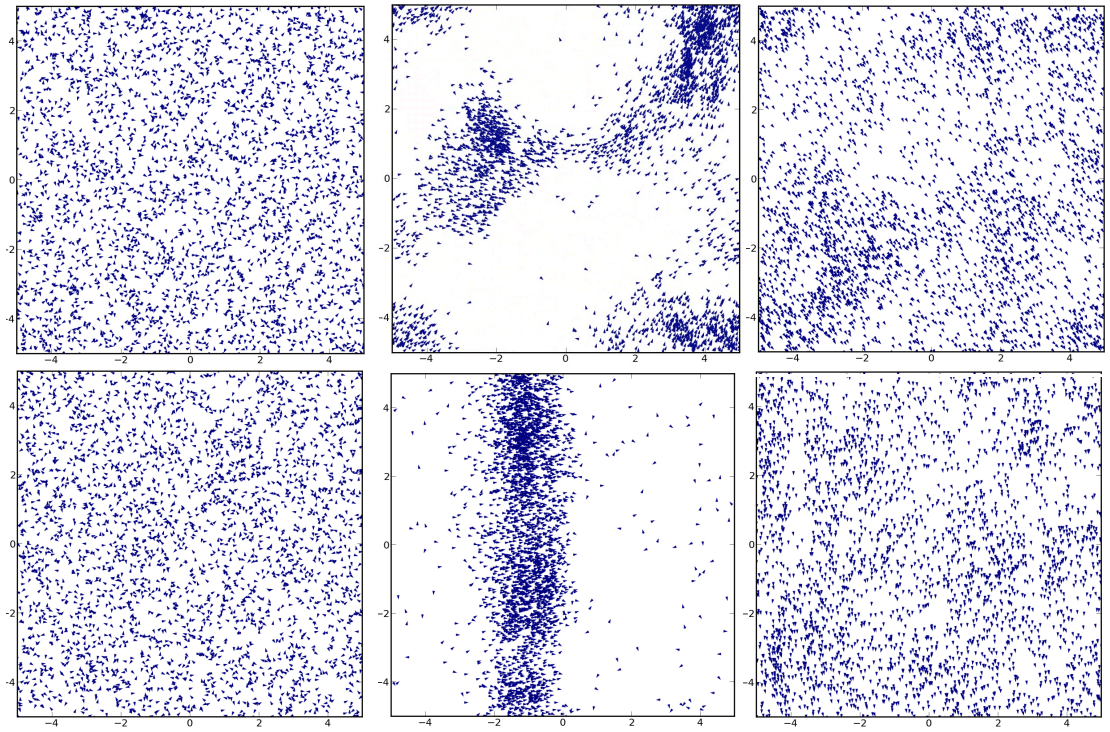

FIGURE 3.7: Top row: snapshots from the inertial spin model. Bottom row: snapshots from the continuous time Vicsek model.

The simulations reproduce the disorder-order phase transition line quantitatively as predicted by the hydrodynamic theory. Notice that for the inertial spin model, there is a regime of large spin fluctuations from the onset of order to $\gamma \approx 50$, where spontaneously swirling and turning flocks are observed Fig.3.7 (top middle). Beyond this regime, the mean polarization approximates unity and the spin fluctuations are suppressed, signaling the transition to a homogeneous polar state. An alternative set of hydrodynamic equations based on a different closure is applicable for this regime as shown in section 3.9.2 of the Appendix. In contrast, the continuous time Vicsek model displays a smooth transition from the banding state to a homogeneous polar state much earlier ($\gamma \approx 20$) Fig. 3.7 (bottom) without spontaneously turning flocks. The observations lend qualitative support to the existence of a spin-wave instability at intermediate alignment interactions as predicted by the hydrodynamic theory.

3.8 Appendix 3.A: Fokker-Planck equation

In this section, we derive the Fokker-Planck equation for the active inertial spin model starting from the microscopic equations of motion as in Eq.3.1-3.2. To start, we introduce an arbitrary analytic function $g(\boldsymbol{r}_i, \theta_i, s_i)$, and the probability distribution function for particle i

$$p_i(\boldsymbol{r}, \theta, s) = \delta(\boldsymbol{r} - \boldsymbol{r}_i)\delta(\theta - \theta_i)\delta(s - s_i), \tag{3.21}$$

from which we define the global probability distribution function

$$P(\boldsymbol{r}, \theta, s) = \sum_i p_i(\boldsymbol{r}, \theta, s), \tag{3.22}$$

whose dynamics is governed by the Fokker-Planck equation to be derived. We take the time derivative of $g(\boldsymbol{r}_i, \theta_i, s_i)$ using Ito calculus and obtain

$$\dot{g}(\boldsymbol{r}_i, \theta_i, s_i) = \nabla_{\boldsymbol{r}_i} g \cdot \dot{\boldsymbol{r}}_i + (\partial_{\theta_i} g)\dot{\theta}_i + (\partial_{s_i} g)\dot{s}_i + \epsilon \frac{\partial^2 g}{\partial s_i^2} \tag{3.23}$$

Using Eq. 3.1-3.2, we obtain

$$\begin{aligned} \dot{g}(\boldsymbol{r}_i, \theta_i, s_i) &= \nabla_{\boldsymbol{r}_i} g \cdot \boldsymbol{v} + \frac{s_i}{\chi}(\partial_{\theta_i} g) \\ +(\partial_{s_i} g)[\gamma \sum_j F(\theta_j - \theta_i, \boldsymbol{r}_j - \boldsymbol{r}_i) &+ \sqrt{2\epsilon}\xi_i(t) - \frac{\eta}{\chi} s_i] + \epsilon \frac{\partial^2 g}{\partial s_i^2} \end{aligned} \tag{3.24}$$

Using the definition of p_i (Eqn. 3.21)

$$\dot{g}(\boldsymbol{r}_i,\theta_i,s_i) = \int d\boldsymbol{r}d\theta ds(\nabla g\cdot\boldsymbol{v} + \frac{s}{\chi}(\partial_\theta g) \tag{3.25}$$
$$+(\partial_s g)[\gamma\sum_j F(\theta_j-\theta,\boldsymbol{r}_j-\boldsymbol{r}) + \sqrt{2\epsilon}\xi_i(t) - \frac{\eta}{\chi}s] + \epsilon\frac{\partial^2 g}{\partial s^2})p_i.$$

Integrating by parts

$$\dot{g}(\boldsymbol{r}_i,\theta_i,s_i) = \int d\boldsymbol{r}d\theta ds(-\nabla\cdot(p_i\boldsymbol{v}) - \frac{s}{\chi}(\partial_\theta p_i) \tag{3.26}$$
$$-\partial_s[\gamma p_i\sum_j F(\theta_j-\theta,\boldsymbol{r}_j-\boldsymbol{r}) + \sqrt{2\epsilon}p_i\xi_i(t) - \frac{\eta}{\chi}sp_i] + \epsilon\frac{\partial^2 p_i}{\partial s^2})g(\boldsymbol{r},\theta,s).$$

and using identities

$$\dot{g}(\boldsymbol{r}_i,\theta_i,s_i) = \int d\boldsymbol{r}d\theta ds[\dot{p}_i g(\boldsymbol{r},\theta,s)] \tag{3.27}$$
$$F(\boldsymbol{r}_j-\boldsymbol{r},\theta_j-\theta) = \int d\boldsymbol{r}'d\theta' ds'[p_j(\boldsymbol{r}',\theta',s')F(\boldsymbol{r}'-\boldsymbol{r},\theta'-\theta)] \tag{3.28}$$

we obtain

$$\int d\boldsymbol{r}d\theta ds(-\partial_s[\gamma p_i\int d\boldsymbol{r}'d\theta' ds' p_j\sum_j F(\theta'-\theta,\boldsymbol{r}'-\boldsymbol{r}) + \sqrt{2\epsilon}p_i\xi_i(t) - \frac{\eta}{\chi}sp_i] \tag{3.29}$$
$$-\nabla\cdot(p_i\boldsymbol{v}) - \frac{s}{\chi}(\partial_\theta p_i) + \epsilon\frac{\partial^2 p_i}{\partial s^2})g(\boldsymbol{r},\theta,s) = \int d\boldsymbol{r}d\theta ds[\dot{p}_i g(\boldsymbol{r},\theta,s)].$$

Summing over all particles by using eqn. eq:p and with the fact that $g(\boldsymbol{r},\theta,s)$ is an arbitrary function, we obtain the Fokker-Planck equation

$$\dot{P}(\boldsymbol{r},\theta,s,t) + \boldsymbol{v}_\theta\cdot\nabla P = -\frac{\partial}{\partial\theta}(\frac{1}{\chi}sP) + \tau(\theta,\boldsymbol{r},t)\frac{\partial P}{\partial s} + \frac{\partial}{\partial s}(\frac{\eta}{\chi}sP) + \epsilon\frac{\partial^2 P}{\partial s^2} \tag{3.30}$$
$$-\frac{\partial}{\partial s}\sqrt{2\epsilon P}\xi(\boldsymbol{r},\theta,s,t)\,,$$

where

$$<\xi(\boldsymbol{r},\theta,s,t)\xi(\boldsymbol{r}',\theta',s',t')>=\delta(\boldsymbol{r}'-\boldsymbol{r})\delta(\theta'-\theta)\delta(s'-s)\delta(t'-t) \tag{3.31}$$

For later discussion, we drop the stochastic noise and work with noise-averaged quantities.

3.9 Appendix 3.B: Closures for continuum equations

The Fokker-Planck equation for the one-particle probability density $P(\boldsymbol{r},\theta,s,t)$ associated with Eqs. 3.1 and 3.2 of the main text is given by

$$\dot{P}(\boldsymbol{r},\theta,s,t)+\boldsymbol{v}_\theta\cdot\nabla P=-\frac{\partial}{\partial\theta}(\frac{1}{\chi}sP)+\tau(\theta,\boldsymbol{r},t)\frac{\partial P}{\partial s}+\frac{\partial}{\partial s}(\frac{\eta}{\chi}sP)+\epsilon\frac{\partial^2 P}{\partial s^2}\,, \tag{3.32}$$

where $\tau(\theta,\boldsymbol{r},t)=-\gamma\int_{-\pi}^{\pi}d\theta' F(\theta'-\theta)p_0(\boldsymbol{r},\theta',t)$ is the torque. We have assumed local interaction $F(\theta,\boldsymbol{r})=\delta(\boldsymbol{r})\sin(\theta)$ and defined $p_0(\boldsymbol{r},\theta',t)=\int_s P(\boldsymbol{r},\theta',s,t)$. To make the notation more compact, we define the Fokker-Planck operator as

$$L_k=L_{rev}+L_{ir}\,, \tag{3.33}$$

$$L_{rev}=-\frac{s}{\chi}\frac{\partial}{\partial\theta}+\tau(\boldsymbol{r},\theta,t)\frac{\partial}{\partial s}-\boldsymbol{v}_\theta\cdot\boldsymbol{\nabla}\,, \tag{3.34}$$

$$L_{ir}=\frac{\eta}{\chi}\frac{\partial}{\partial s}(s+s_0^2\frac{\partial}{\partial s})\,, \tag{3.35}$$

where L_{rev} and L_{ir} represent the reversible and irreversible part of the Fokker-Planck operator respectively, and we have introduced the steady state value of the spin $s_0^2=\frac{\epsilon\chi}{\eta}$. In the absence of interaction and activity, the steady state distribution of the spin has a Maxwell-like form, given by

$$P_0(s)=\frac{1}{\sqrt{2\pi s_0^2}}\exp(-\frac{s^2}{2s_0^2}). \tag{3.36}$$

Following standard methods [98], we transform the Fokker-Planck operator by multiplying it from the right and the left by $\phi_0(s)=P_0^{\frac{1}{2}}(s)$ and $\phi_0^{-1}(s)=P_0^{-\frac{1}{2}}(s)$, respectively, with the result

$$\bar{L}_k=\phi_0^{-1}(s)L_k\phi_0(s)=\bar{L}_{rev}+\bar{L}_{ir}\,, \tag{3.37}$$

$$\bar{L}_{ir}=-\frac{\eta}{\chi}b^+b\,,\quad \bar{L}_{rev}=-bD-b^+\hat{D}-\boldsymbol{v}_\theta\cdot\boldsymbol{\nabla}\,, \tag{3.38}$$

where b^+ and b are creation and annihilation operators, respectively.

$$b^+\phi_n(s)=\sqrt{n+1}\phi_{n+1}(s)\,, \tag{3.39}$$

$$b\phi_n(s)=\sqrt{n}\phi_{n-1}(s). \tag{3.40}$$

D and $\hat{D}$ are the differential operators, with the latter containing the information of the interaction,

$$b^+ = -s_0\frac{\partial}{\partial s} + \frac{1}{2}\frac{s}{s_0}\,, \qquad b = s_0\frac{\partial}{\partial s} + \frac{1}{2}\frac{s}{s_0}\,, \tag{3.41}$$

$$D = \frac{s_0}{\chi}\frac{\partial}{\partial\theta}\,, \qquad \hat{D} = \frac{s_0}{\chi}\frac{\partial}{\partial\theta} + \frac{\tau(\theta,\boldsymbol{r},t)}{s_0}. \tag{3.42}$$

The normalized eigenfunctions $\phi_n(s)$ of the operator $\bar{L}_{ir} = -\frac{\eta}{\chi}b^+b$ are defined by the eigenvalue equation

$$\bar{L}_{ir}\phi_n(s) = -\frac{\eta}{\chi}n\phi_n(s)\,, \tag{3.43}$$

with

$$\phi_n(s) = (b^+)^n\phi_0(s)/\sqrt{n!}\,, \tag{3.44}$$

$$\phi_0(s) = \exp(-\frac{s^2}{4s_0^2})/\sqrt{s_0\sqrt{2\pi}}. \tag{3.45}$$

Finally, $\phi_n(s)$ are related to the Hermite polynomials $H_n(x) = \left(2x - \frac{d}{dx}\right)^n \cdot 1$ as

$$\phi_n(s) = H_n(\frac{s}{\sqrt{2}s_0})\exp(-\frac{s^2}{4s_0^2})/\sqrt{n!2^n s_0\sqrt{2\pi}}. \tag{3.46}$$

We now expand the probability distribution function in terms of $\phi_n(s)$,

$$P(\boldsymbol{r},\theta,s,t) = \phi_0(s)\sum_{n=0}^{\infty}p_n(\boldsymbol{r},\theta,t)\phi_n(s)\,, \tag{3.47}$$

and we insert the expansion into the Fokker-Plank equation,

$$\partial_t P(\boldsymbol{r},\theta,s,t) = L_k P(\boldsymbol{r},\theta,s,t)\,, \tag{3.48}$$

where the Fokker-Plank operator is obtained after an inverse transformation, as

$$L_k = \phi_0(s)(-\frac{\eta}{\chi}b^+b - bD - b^+\hat{D} - \boldsymbol{v}\cdot\boldsymbol{\nabla})\phi_0^{-1}(s). \tag{3.49}$$

Using the properties of the operators and the orthogonality of the Hermite polynomials, we obtain a hierarchy of equations for the moments $p_n(\boldsymbol{r},\theta,t)$,

$$\mathcal{D}_t p_n(\boldsymbol{r},\theta,t) = -\frac{\eta}{\chi}np_n(\boldsymbol{r},\theta,t) \tag{3.50}$$

$$-\sqrt{n+1}Dp_{n+1}(\boldsymbol{r},\theta,t) - \sqrt{n}\hat{D}p_{n-1}(\boldsymbol{r},\theta,t)\,,$$

where $\mathcal{D}_t = \partial_t + \boldsymbol{v}_\theta \cdot \boldsymbol{\nabla}$ is the material derivative. Explicitly, the equations for the first three moments are given by

$$\mathcal{D}_t p_0 = -D p_1 \,, \tag{3.51}$$

$$\mathcal{D}_t p_1 = -\frac{\eta}{\chi} p_1 - \sqrt{2} D p_2 - \hat{D} p_0 \,, \tag{3.52}$$

$$\mathcal{D}_t p_2 = -\frac{2\eta}{\chi} p_2 - \sqrt{3} D p_3 - \sqrt{2} \hat{D} p_1 . \tag{3.53}$$

The first two moments are related to the probability density $c(\boldsymbol{r}, \theta, t)$ of finding a particle at $\boldsymbol{r}$, with velocity directed along θ at time t and the spin current $j(\boldsymbol{r}, \theta, t)$,

$$c(\boldsymbol{r}, \theta, t) = p_0 = \int_{-\infty}^{\infty} P(\boldsymbol{r}, \theta, s, t) ds \,, \tag{3.54}$$

$$j(\boldsymbol{r}, \theta, t) = s_0 p_1 = \int_{-\infty}^{\infty} s P(\boldsymbol{r}, \theta, s, t) ds \,, \tag{3.55}$$

To obtain closed equations for c and j, we set $\mathcal{D}_t p_2 = 0$ for times long compared to $\chi/2\eta$, and let $p_n = 0$ for $n \geq 3$. We then eliminate p_2 in favor of p_0 and p_1 to obtain closed equations. The equations for density and current are then given by

$$\mathcal{D}_t c(\boldsymbol{r}, \theta, t) = -\frac{1}{\chi} \frac{\partial j}{\partial \theta} \,, \tag{3.56}$$

$$\begin{aligned} \mathcal{D}_t j(\boldsymbol{r}, \theta, t) = &-\frac{\eta}{\chi} j + \frac{\epsilon}{\eta^2} \frac{\partial^2 j}{\partial \theta^2} + \frac{1}{\eta} \frac{\partial [\tau(\boldsymbol{r}, \theta, t) j]}{\partial \theta} \\ &-\frac{\epsilon}{\eta} \frac{\partial c}{\partial \theta} - \tau(\boldsymbol{r}, \theta, t) c. \end{aligned} \tag{3.57}$$

The goal is to obtain closed equations for the number density $\rho(\boldsymbol{r}, t)$, polarization density $\boldsymbol{w}(\boldsymbol{r}, t)$ and spin current $S(\boldsymbol{r}, t)$, which are the conserved, symmetry-breaking and relevant dynamic variables in the flocking system, respectively. Generalizing the method described in Ref.[88], we introduce the angular Fourier transform of c and j as

$$c_k(\boldsymbol{r}, t) = \int_{-\pi}^{\pi} c(\boldsymbol{r}, \theta, t) e^{ik\theta} d\theta \,, \tag{3.58}$$

$$j_k(\boldsymbol{r}, t) = \int_{-\pi}^{\pi} j(\boldsymbol{r}, \theta, t) e^{ik\theta} d\theta \,, \tag{3.59}$$

which are related to $\rho(\boldsymbol{r}, t)$, $\boldsymbol{w}(\boldsymbol{r}, t)$ and $S(\boldsymbol{r}, t)$ by

$$\rho(\boldsymbol{r}, t) = c_0(\boldsymbol{r}, t) \,, \quad S(\boldsymbol{r}, t) = j_0(\boldsymbol{r}, t) \,, \tag{3.60}$$

$$w_x(\boldsymbol{r}, t) = Re[c_1(\boldsymbol{r}, t)] \,, \quad w_y(\boldsymbol{r}, t) = Im[c_1(\boldsymbol{r}, t)] \,, \tag{3.61}$$

whose dynamic equations are

$$\partial_t c_k(\boldsymbol{r},t) + \frac{v_0}{2}\nabla^* c_{k+1} + \frac{v_0}{2}\nabla c_{k-1} = \frac{ik}{\chi} j_k \,, \tag{3.62}$$

$$\partial_t j_k(\boldsymbol{r},t) + \frac{v_0}{2}\nabla^* j_{k+1} + \frac{v_0}{2}\nabla j_{k-1} = -\frac{\eta_k}{\chi} j_k + \frac{ik\epsilon}{\eta} c_k \tag{3.63}$$
$$+\frac{ik\gamma}{2\pi\eta}\sum_m j_{k-m}F_{-m}c_m + \frac{\gamma}{2\pi}\sum_m c_{k-m}F_{-m}c_m \,,$$

where $\nabla = \partial_x + i\partial_y$, $\nabla^* = \partial_x - i\partial_y$ and $F_{\pm 1} = \pm i\pi$. We have introduced an effective friction $\eta_k = \eta + k^2\epsilon\chi/\eta^2$.

3.9.1 Closure close to the disorder-order transition

Explicity, the equations for c_0, c_1 and j_0 are given by

$$\partial_t c_0 + \frac{v_0}{2}\nabla^* c_1 + \frac{v_0}{2}\nabla c_1^* = 0 \,, \tag{3.64}$$

$$\partial_t c_1 + \frac{v_0}{2}\nabla^* c_2 + \frac{v_0}{2}\nabla c_0 = \frac{i}{\chi} j_1 \,, \tag{3.65}$$

$$\partial_t j_0 + \frac{v_0}{2}\nabla^* j_1 + \frac{v_0}{2}\nabla j_1^* = -\frac{\eta}{\chi} j_0. \tag{3.66}$$

To close these equations, we need to express j_1 and c_2 in terms of c_0, c_1 and j_0. To do so, we consider the equations for j_1, j_2 and c_2,

$$\partial_t j_1 + \frac{v_0}{2}\nabla^* j_2 + \frac{v_0}{2}\nabla j_0 = -\frac{\eta_1}{\chi} j_1 + \frac{i\epsilon}{\eta} c_1 - \frac{\gamma}{2\eta}(j_2 c_1^* - j_0 c_1) + \frac{i\gamma}{2}(c_2 c_1^* - c_0 c_1) \,, \tag{3.67}$$

$$\partial_t j_2 + \frac{v_0}{2}\nabla^* j_3 + \frac{v_0}{2}\nabla j_1 = -\frac{\eta_2}{\chi} j_2 + \frac{2i\epsilon}{\eta} c_2 - \frac{\gamma}{\eta}(j_3 c_1^* - j_1 c_1) + \frac{i\gamma}{2}(c_3 c_1^* - c_1 c_1) \,, \tag{3.68}$$

$$\partial_t c_2 + \frac{v_0}{2}\nabla^* c_3 + \frac{v_0}{2}\nabla c_1 = \frac{2i}{\chi} j_2. \tag{3.69}$$

For times long compared to χ/η, we set $\partial_t j_1 = \partial_t j_2 = 0$. Retaining terms up to first order in χ/η we obtain the expression for j_1 and j_2,

$$j_1 = \frac{\chi}{\eta_1}\left[\frac{i\epsilon}{\eta} c_1 + \frac{\gamma}{2\eta} j_0 c_1 + \frac{i\gamma}{2}(c_2 c_1^* - c_0 c_1) - \frac{v_0}{2}\nabla j_0\right] + \mathcal{O}(\chi^2), \tag{3.70}$$

$$j_2 = \frac{\chi}{\eta_2}\left(\frac{2i\epsilon}{\eta} c_2 - \frac{i\gamma}{2} c_1^2\right) + \mathcal{O}(\chi^2). \tag{3.71}$$

Inserting Eq. 3.71 into the equation for c_2, we obtain,

$$\partial_t c_2 + \frac{v_0}{2}\nabla^* c_3 + \frac{v_0}{2}\nabla c_1 = \frac{\gamma}{\eta_2} c_1^2 - \frac{4\epsilon}{\eta\eta_2} c_2. \tag{3.72}$$

For times long compared to $\frac{\eta\eta_2}{4\epsilon}$, we follow the method of Ref. [88, 95] and set $\partial_t c_2 = 0$ and $c_n = 0$ for $n \geq 3$ to obtain the expression for c_2,

$$c_2 = \frac{\gamma\eta}{4\epsilon}c_1^2 - \frac{v_0\eta\eta_2}{8\epsilon}\nabla c_1. \tag{3.73}$$

Equations 3.70-3.72 complete the closure and lead to the following closed equations.

$$\frac{\partial c_0}{\partial t} + \frac{v_0}{2}\nabla c_1^* + \frac{v_0}{2}\nabla c_1 = 0\,, \tag{3.74}$$

$$\frac{\partial c_1}{\partial t} + \frac{v_0}{2}\nabla c_0 + \frac{v_0\gamma\eta}{8\epsilon}\nabla^* c_1^2 = \left(\frac{\gamma}{2\eta_1}c_0 - \frac{\epsilon}{\eta\eta_1} - \frac{\gamma^2\eta}{8\epsilon\eta_1}|c_1|^2\right)c_1 + \frac{i\gamma}{2\eta\eta_1}j_0 c_1$$
$$-\frac{iv_0}{2\eta_1}\nabla j_0 + \frac{\gamma v_0\eta\eta_2}{16\epsilon\eta_1}c_1^*\nabla c_1 + \frac{v_0^2\eta\eta_2}{16\epsilon}\nabla^2 c_1\,, \tag{3.75}$$

$$\frac{\partial j_0}{\partial t} + \frac{i\chi\gamma v_0^2\eta\eta_2}{32\epsilon\eta_1}\left(\nabla\left[(\nabla^* c_1^*)c_1\right] - \nabla^*\left[(\nabla c_1)c_1^*\right]\right) = -\frac{v_0\gamma\chi}{4\eta_1}\left[i\nabla(c_0 c_1^*) - i\nabla^*(c_0 c_1)\right] \tag{3.76}$$
$$-\frac{v_0\epsilon\chi}{2\eta\eta_1}\left(-i\nabla c_1^* + i\nabla^* c_1\right) - \frac{v_0\gamma^2\eta\chi}{16\epsilon\eta_1}\left[-i\nabla(|c_1|^2 c_1^*) + i\nabla^*(|c_1|^2 c_1)\right]$$
$$-\frac{v_0\gamma\chi}{4\eta\eta_1}\left[\nabla(c_1^* j_0) + \nabla^*(c_1 j_0)\right] + \frac{\chi v_0^2}{2\eta_1}\nabla^2 j_0 - \frac{\eta}{\chi}j_0. \tag{3.77}$$

Using relations given in Eqn.3.60, and the following identities

$$\nabla^* c_1^2 = \left[2(\boldsymbol{w}\cdot\nabla)\boldsymbol{w} + 2\boldsymbol{w}(\nabla\cdot\boldsymbol{w}) - \nabla|w|^2\right]\,, \tag{3.78}$$

$$ic_1 j_0 = \boldsymbol{S}\times\boldsymbol{w}\,, \tag{3.79}$$

$$i\nabla j_0 = -\nabla\times\boldsymbol{S} \tag{3.80}$$

$$i\nabla(c_0 c_1^*) - i\nabla^*(c_0 c_1) = -2\nabla\times(\rho\boldsymbol{w})\,, \tag{3.81}$$

$$-i\nabla c_1^* + i\nabla^* c_1 = 2\nabla\times\boldsymbol{w}\,, \tag{3.82}$$

$$-i\nabla(|c_1|^2 c_1^*) + i\nabla^*(|c_1|^2 c_1) = 2\nabla\times(|w|^2\boldsymbol{w})\,, \tag{3.83}$$

$$\nabla(c_1^* j_0) + \nabla^*(c_1 j_0) = 2\boldsymbol{S}\nabla\cdot\boldsymbol{w} + 2(\boldsymbol{w}\cdot\nabla)\boldsymbol{S}\,, \tag{3.84}$$

$$c_1^*\nabla c_1 = (\boldsymbol{w}\cdot\nabla)\boldsymbol{w} - \boldsymbol{w}(\nabla\cdot\boldsymbol{w}) + \frac{1}{2}\nabla|\boldsymbol{w}|^2\,, \tag{3.85}$$

$$i\left(\nabla\left[(\nabla^* c_1^*)c_1\right]\right) - \nabla^*\left[(\nabla c_1)c_1^*\right]) = -2\boldsymbol{w}\times\nabla^2\boldsymbol{w}, \tag{3.86}$$

we arrive at the hydrodynamic equations

$$\frac{\partial\rho}{\partial t} = -v_0\boldsymbol{\nabla}\cdot\boldsymbol{w}\,, \tag{3.87}$$

$$\mathcal{D}_t^w\boldsymbol{w} = -\left[\alpha(\rho) + \beta|\boldsymbol{w}|^2\right]\boldsymbol{w} - \frac{v_0}{2}\boldsymbol{\nabla}\rho + \lambda_2\boldsymbol{w}(\boldsymbol{\nabla}\cdot\boldsymbol{w}) + \frac{\lambda_3}{2}\nabla|w|^2$$
$$+\Omega_1\boldsymbol{S}\times\boldsymbol{w} + \Omega_2\boldsymbol{\nabla}\times\boldsymbol{S} + D_w\nabla^2\boldsymbol{w}\,, \tag{3.88}$$

$$\mathcal{D}_t^s\boldsymbol{S} = -v_0\chi\boldsymbol{\nabla}\times\left[\left(\alpha(\rho) + \beta|w|^2\right)\boldsymbol{w}\right] + \Omega_3\boldsymbol{w}\times\nabla^2\boldsymbol{w}$$
$$-\lambda_s(\boldsymbol{\nabla}\cdot\boldsymbol{w})\boldsymbol{S} - \xi\boldsymbol{S} + D_s\nabla^2\boldsymbol{S}\,, \tag{3.89}$$

where $\mathcal{D}_t^w = \partial_t + \lambda_1 \boldsymbol{w}\cdot\boldsymbol{\nabla}$ and $\mathcal{D}_t^s = \partial_t + \lambda_s \boldsymbol{w}\cdot\boldsymbol{\nabla}$ are convective derivatives. All coefficients are related to the microscopic parameters as

$$\alpha(\rho) = \frac{1}{\eta_1}(\frac{\epsilon}{\eta} - \frac{\gamma\rho}{2}),\ \beta = \frac{1}{\eta_1}\frac{\eta\gamma^2}{8\epsilon},$$
$$\Omega_1 = \frac{\gamma}{2\eta\eta_1},\ \Omega_2 = \frac{v_0}{2\eta_1},\ \Omega_3 = \frac{\chi\gamma v_0^2\eta\eta_2}{16\epsilon\eta_1},$$
$$\lambda_1 = \frac{v_0\gamma\eta}{4\epsilon} - \frac{\gamma v_0\eta\eta_2}{16\epsilon\eta_1},\ \lambda_3 = -\lambda_2 = \frac{v_0\gamma\eta}{4\epsilon} + \frac{\gamma v_0\eta\eta_2}{16\epsilon\eta_1},$$
$$\lambda_s = \frac{v_0\chi\gamma}{2\eta\eta_1},\ \xi = \frac{\eta}{\chi},\ D_w = \frac{v_0^2\eta\eta_2}{16\epsilon},\ D_s = \frac{\chi v_0^2}{2\eta_1},\ \eta_k = \eta + \frac{k^2\epsilon\chi}{\eta^2}.$$

3.9.2 Closure away from the disorder-order transition

The closure in the previous section is justified close to the disorder-order transition, which predicts the banding instability from the growth of longitudinal fluctuations and the spin wave instability from transverse fluctuations. However, it fails to account for the stable homogeneous polar state deep in the polarized region, which is relevant for cohesive flocks that do not display large density fluctuations. Particle simulations show that homogeneous polar flock emerges for $\tilde{\gamma} = \gamma\rho_0\eta/\epsilon > 50$. Thus for this regime, we use an alternative closure in reference to [45].

Instead of Eqn. 3.72, we close c_2 assuming $c_2 = c_1^2|c_1|^2/c_0^3$. This is the case when the angular probability distribution $\Phi(\boldsymbol{r},\theta,t)$ is peaked and the high-order cumulants of the generating function can be neglected, satisfied by the homogeneous polar state. Together with Eqn 3.70, this yields the following hydrodynamic equations.

$$\frac{\partial\rho}{\partial t} = -v_0\boldsymbol{\nabla}\cdot\boldsymbol{w}\ , \tag{3.90}$$

$$\partial_t\boldsymbol{w} + \frac{v_0}{\rho^3}|w|^2(\boldsymbol{w}\cdot\nabla)\boldsymbol{w} = -\left[\alpha(\rho) + \beta\frac{|w|^4}{\rho^3}\right]\boldsymbol{w} - \frac{v_0}{2}\boldsymbol{\nabla}\rho + \frac{3v_0}{2\rho^4}|w|^2(2\boldsymbol{w}\boldsymbol{w} - |w|^2\boldsymbol{I})\cdot\nabla\rho$$
$$-\frac{v_0}{\rho^3}|w|^2\boldsymbol{w}(\boldsymbol{\nabla}\cdot\boldsymbol{w}) + \frac{v_0}{\rho^3}(|w|^2\boldsymbol{I} - \boldsymbol{w}\boldsymbol{w})\cdot\boldsymbol{\nabla}|w|^2 + \Omega_1\boldsymbol{S}\times\boldsymbol{w} + \Omega_2\boldsymbol{\nabla}\times\boldsymbol{S}\ , \tag{3.91}$$

$$\partial_t\boldsymbol{S} + \lambda_s(\boldsymbol{w}\cdot\nabla)\boldsymbol{S} = -v_0\chi\boldsymbol{\nabla}\times\left[\left(\alpha(\rho) + \beta\frac{|w|^4}{\rho^3}\right)\boldsymbol{w}\right] - \lambda_s(\boldsymbol{\nabla}\cdot\boldsymbol{w})\boldsymbol{S} - \xi\boldsymbol{S} + D_s\nabla^2\boldsymbol{S}\ , \tag{3.92}$$

with coefficients

$$\alpha(\rho) = \frac{1}{\eta_1}(\frac{\epsilon}{\eta} - \frac{\gamma\rho}{2}),\ \beta = \frac{\gamma}{2\eta_1},$$
$$\Omega_1 = \frac{\gamma}{2\eta\eta_1},\ \Omega_2 = \frac{v_0}{2\eta_1},$$
$$\lambda_s = \frac{v_0\chi\gamma}{2\eta\eta_1},\ \xi = \frac{\eta}{\chi},\ D_s = \frac{\chi v_0^2}{2\eta_1},\ \eta_k = \eta + \frac{k^2\epsilon\chi}{\eta^2}.$$

These set of equations predict a stable homogeneous polar state away from the disorder-order transition as expected, and retains the banding instability close to the transition. Surprisingly, The transition line is unaltered. A set of more compact equations can be written down for the density-independent polarization $\boldsymbol{P} = \boldsymbol{w}/\rho$ and spin current $\boldsymbol{g} = \boldsymbol{S}/\rho$.

$$\frac{\partial \rho}{\partial t} = -v_0 \boldsymbol{P} \cdot \boldsymbol{\nabla} \rho - v_0 \rho (\nabla \cdot \boldsymbol{P}) \ , \tag{3.93}$$

$$\begin{aligned}\partial_t \boldsymbol{P} + v_0 |P|^2 (\boldsymbol{P} \cdot \nabla) \boldsymbol{P} = &- \left[\alpha(\rho) + \beta \rho |P|^4\right] \boldsymbol{P} + \frac{v_0}{2\rho}(|P|^4 - 1)\nabla\rho + \frac{v_0}{\rho}(1 - |P|^2)\boldsymbol{P}(\boldsymbol{P}\cdot\nabla)\rho \\ &+ v_0(1 - |P|^2)\boldsymbol{P}(\boldsymbol{\nabla}\cdot\boldsymbol{P}) + v_0(|P|^2 \boldsymbol{I} - \boldsymbol{PP})\cdot\boldsymbol{\nabla}|P|^2 + \Omega_1 \rho \boldsymbol{g}\times\boldsymbol{P} + \Omega_2 \boldsymbol{\nabla}\times\boldsymbol{g} + \frac{\Omega_2}{\rho}\nabla\rho\times\boldsymbol{g} \ ,\end{aligned} \tag{3.94}$$

$$\begin{aligned}\partial_t \boldsymbol{g} + \lambda_s \rho (\boldsymbol{P}\cdot\nabla)\boldsymbol{g} = &-v_0\chi\boldsymbol{\nabla}\times\left[\left(\alpha(\rho) + \beta\rho|P|^4\right)\boldsymbol{P}\right] - (\lambda_s\rho - v_0)(\boldsymbol{\nabla}\cdot\boldsymbol{P})\boldsymbol{g} - \xi\boldsymbol{g} + D_s\nabla^2\boldsymbol{g} \\ &+ (\frac{v_0}{\rho} - \frac{v_0\gamma\chi}{\eta\eta_1})\boldsymbol{g}\boldsymbol{P}\cdot\nabla\rho - \frac{v_0\chi}{\rho}\nabla\rho\times\left[\left(\alpha(\rho) + \beta\rho|P|^4\right)\boldsymbol{P}\right] + \frac{\chi v_0^2}{2\eta_1\rho}\boldsymbol{g}\nabla^2\rho,\end{aligned} \tag{3.95}$$

These complicated-looking equations can be simplified deep in the polar state given that the homogeneous polar state is stable with a magnitude of the polarization $|P| \to 1$. Moreover, if we restrict ourselves to the linear response of the system, i.e. its behavior under small fluctuations, we neglect terms that have no contribution once linearized, we obtain the minimal equations deep in the polar state.

$$\frac{\partial \rho}{\partial t} = -v_0 \boldsymbol{P} \cdot \boldsymbol{\nabla} \rho - v_0 \rho (\nabla \cdot \boldsymbol{P}) \ , \tag{3.96}$$

$$\begin{aligned}\partial_t \boldsymbol{P} + v_0 |P|^2 (\boldsymbol{P} \cdot \nabla) \boldsymbol{P} = &- \left[\alpha(\rho) + \beta \rho |P|^4\right] \boldsymbol{P} + v_0(|P|^2 \boldsymbol{I} - \boldsymbol{PP})\cdot\boldsymbol{\nabla}|P|^2 \\ &+ \Omega_1 \rho \boldsymbol{g}\times\boldsymbol{P} + \Omega_2 \boldsymbol{\nabla}\times\boldsymbol{g} \ ,\end{aligned} \tag{3.97}$$

$$\partial_t \boldsymbol{g} + \lambda_s \rho (\boldsymbol{P}\cdot\nabla)\boldsymbol{g} = -v_0\chi\boldsymbol{\nabla}\times\left[\left(\alpha(\rho) + \beta\rho|P|^4\right)\boldsymbol{P}\right] - \xi\boldsymbol{g} + D_s\nabla^2\boldsymbol{g}, \tag{3.98}$$

These set of equations could serve as the basis for the analysis of information propagation through well-polarized cohesive flocks.

3.10 Appendix 3.C: Free-energy-based hydrodynamic equations

As an alternative approach, we write down the free energy of the system based on symmetry,

$$\begin{aligned}F = \int d\boldsymbol{r}[&\frac{\alpha}{2}w^2 + \frac{\beta}{4}w^4 + \frac{K_w}{2}(\nabla\boldsymbol{w})^2 + c_1\boldsymbol{w}\cdot\nabla\rho + c_2\boldsymbol{S}\cdot(\nabla\times\boldsymbol{w}) + \frac{\lambda}{2}|w|^2\nabla\cdot\boldsymbol{w} \\ &+ \frac{S^2}{2\chi} + \frac{K_s}{2}(\nabla\boldsymbol{S})^2].\end{aligned} \tag{3.99}$$

The dynamic equations can thus be written as

$$\partial_t \boldsymbol{w} + \lambda_w \boldsymbol{w} \cdot \nabla \boldsymbol{w} = -\Gamma_1 \frac{\delta F}{\delta \boldsymbol{w}} - \Gamma_2 \boldsymbol{w} \times \frac{\delta F}{\delta \boldsymbol{S}} \tag{3.100}$$

$$\partial_t \boldsymbol{S} + \lambda_s \boldsymbol{w} \cdot \nabla \boldsymbol{S} = -\Gamma_3 \frac{\delta F}{\delta \boldsymbol{S}} - \Gamma_4 \boldsymbol{w} \times \frac{\delta F}{\delta \boldsymbol{w}} - \Gamma_5 \nabla \times \frac{\delta F}{\delta \boldsymbol{w}} \tag{3.101}$$

With conservation of density, the resulting equations are as follows, where $F[\boldsymbol{w}, \nabla \boldsymbol{w}] = -\Gamma_1 \lambda [\boldsymbol{w}(\nabla \cdot \boldsymbol{w}) - \frac{1}{2} \nabla |w|^2]$.

$$\frac{\partial \rho}{\partial t} = -\nabla \cdot (v_0 \boldsymbol{w}) + D \nabla^2 \rho \tag{3.102}$$

$$\frac{\partial \boldsymbol{w}}{\partial t} + \lambda_w \boldsymbol{w} \cdot \nabla \boldsymbol{w} = -\Gamma_1 [(\alpha + \beta |w|^2) \boldsymbol{w} + c_1 \nabla \rho - c_2 (\nabla \times \boldsymbol{S})] + \frac{\Gamma_2}{\chi} \boldsymbol{S} \times \boldsymbol{w} \tag{3.103}$$

$$+ F[\boldsymbol{w}, \nabla \boldsymbol{w}] + \Gamma_1 K_w \nabla^2 \boldsymbol{w}$$

$$\frac{\partial \boldsymbol{S}}{\partial t} + \lambda_s \boldsymbol{w} \cdot \nabla \boldsymbol{S} = -\Gamma_5 \nabla \times [(\alpha + \beta |w|^2) \boldsymbol{w}] + \Gamma_4 K_w \boldsymbol{w} \times \nabla^2 \boldsymbol{w} - c_2 \Gamma_4 (\nabla \cdot \boldsymbol{w}) \boldsymbol{S} \tag{3.104}$$

$$+ \Gamma_3 K_s \nabla^2 \boldsymbol{S} - \frac{\Gamma_3}{\chi} \boldsymbol{S}$$

3.11 Appendix 3.D: Linearized equations

3.11.1 Linear stability close to the disorder-order transition

We start with the dimensionless hydrodynamic equations 3.12-3.14, and add the λ_3 term for completeness. To perform linear mode analysis, we restrict ourselves to the 2D planar case. The isotropic state is always stable therefore trivial, and we focus on the uniformly polarized state for $\gamma > 2$ with the direction of spontaneous broken symmetry along $\hat{x}$. Perturbing around the polarized state $\rho = 1 + \delta\rho$, $\boldsymbol{w} = w_0 \hat{x} + \delta \boldsymbol{w}$ and $\boldsymbol{S} = \delta S \hat{z}$, we arrive at the linearized equations

$$\frac{\partial \delta \rho}{\partial t} = -\nabla \cdot \delta \boldsymbol{w}, \tag{3.105}$$

$$\frac{\partial \delta \boldsymbol{w}}{\partial t} + \lambda_1 w_0 \partial_x \delta \boldsymbol{w} = (\mu_1 \delta \rho + \mu_2 \delta w_x)\, w_0 \hat{x} - \kappa \boldsymbol{\nabla} \delta \rho + \lambda_2 w_0 \hat{x} \boldsymbol{\nabla} \cdot \delta \boldsymbol{w} \tag{3.106}$$

$$+ \lambda_3 w_0 \nabla \delta w_x + \Omega_1 \delta S \hat{z} \times w_0 \hat{x} + \Omega_2 \boldsymbol{\nabla} \times \delta S \hat{z} + D_w \nabla^2 \delta \boldsymbol{w},$$

$$\frac{\partial \delta S \hat{z}}{\partial t} + \lambda_s w_0 \partial_x (\delta S_z \hat{z}) = \nabla \times [(\mu_1 \delta \rho + \mu_2 \delta w_x) w_0 \hat{x}] + \Omega_3 w_0 \hat{x} \times \nabla^2 \delta w \tag{3.107}$$

$$- \xi \delta S \hat{z} + D_s \nabla^2 (\delta S \hat{z}),$$

where $\mu_1 = \frac{\gamma}{2(1+\chi)}$, $\mu_2 = -\frac{w_0 \gamma^2}{4(1+\chi)}$, $\kappa = \frac{1}{2}$ and $w_0 = \left[(\frac{\gamma}{2} - 1) \frac{8}{\gamma^2} \right]^{1/2}$.

3.11.2 Longitudinal mode

Considering mode along the direction of broken symmetry, we obtain

$$\sigma\delta\rho = -iq\delta w_x, \tag{3.108}$$

$$\sigma\delta w_x = \mu_1 w_0\delta\rho + \mu_2 w_0\delta w_x - i\kappa q\delta\rho + iq\lambda w_0\delta w_x - D_w q^2\delta w_x, \tag{3.109}$$

$$\sigma\delta w_y = -iq\lambda_1 w_0\delta w_y + \Omega_1 w_0\delta S - iq\Omega_2\delta S - D_w q^2\delta w_y, \tag{3.110}$$

$$\sigma\delta S = -q^2\Omega_3 w_0\delta w_y - \xi\delta S - iqw_0\lambda_s\delta S - D_s q^2\delta S, \tag{3.111}$$

where $\lambda = \lambda_3 + \lambda_2 - \lambda_1$. Notice that $\delta\rho$ and δw_x decouple from δw_y and δS, leading to the dispersion relation

$$\sigma(q) = \frac{i\mu_1}{\mu_2}q + \frac{1}{\mu_2 w_0}\left[\frac{\lambda w_0\mu_1}{\mu_2} + \kappa - \frac{\mu_1^2}{\mu_2^2}\right]q^2 + \mathcal{O}(q^3). \tag{3.112}$$

Fluctuations in density and magnitude of polarization lead to the "banding instability" close to the isotropic-polar phase transition as generally observed in polar active fluid, the condition of which is given by

$$\frac{\lambda w_0\mu_1}{\mu_2} + \kappa < \frac{\mu_1^2}{\mu_2^2}. \tag{3.113}$$

Neglecting λ_3 and in terms of the microscopic parameters, it reads

$$\gamma < \frac{8}{3}. \tag{3.114}$$

Dynamics of δw_y and δS gives rise to the spin wave, carrying the information of turning. Neglecting convections and diffusion, the dispersion relation for the spin wave is

$$\sigma_\pm = -\frac{\xi}{2} \pm c_s q\sqrt{\frac{[\xi/(2c_s)]^2}{q^2} - 1}, \tag{3.115}$$

where

$$c_s = w_0\sqrt{\Omega_1\Omega_3} = \left[(\frac{\gamma}{2} - 1)\frac{\chi(1+4\chi)}{4(1+\chi)^2}\right]^{\frac{1}{2}} \tag{3.116}$$

is the wave speed.

3.11.3 Transverse mode

Transverse mode is governed by the full coupled equations:

$$\begin{pmatrix} 0 & 0 & -iq & 0 \\ \mu_1 w_0 & \mu_2 w_0 - D_w q^2 & iq\lambda_2 w_0 & iq\Omega_2 \\ -i\kappa q & iq\lambda_3 w_0 & -D_w q^2 & \Omega_1 w_0 \\ -iq w_0 \mu_1 & -iq w_0 \mu_2 & -q^2\Omega_3 w_0 & -\xi - D_s q^2 \end{pmatrix} \begin{pmatrix} \delta\rho \\ \delta w_x \\ \delta w_y \\ \delta S \end{pmatrix} = \sigma(q) \begin{pmatrix} \delta\rho \\ \delta w_x \\ \delta w_y \\ \delta S \end{pmatrix},$$

which leads to the dispersion relation once treated perturbatively in the long wavelength limit:

$$\begin{aligned} \sigma_\pm(q) = \pm \left(-\frac{w_0\lambda_3\mu_1}{\mu_2} - \kappa \right)^{\frac{1}{2}} q + \frac{1}{2\xi\mu_2^2} \left(\xi w_0 \lambda_2 \lambda_3 \mu_2 - \xi\lambda_3\mu_1 - \xi D_w \mu_2^2 \right) q^2 \\ + \frac{1}{2\xi\mu_2^2} \left(w_0\mu_1\mu_2\Omega_1 - w_0^2\lambda_2\mu_2^2\Omega_1 - w_0^2\mu_2^2\Omega_1\Omega_3 \right) q^2 + \mathcal{O}(q^3), \end{aligned} \tag{3.117}$$

from which a transverse instability is obtained when

$$-\frac{w_0\lambda_3\mu_1}{\mu_2} - \kappa > 0. \tag{3.118}$$

This condition is always satisfied with the microscopic parameters, therefore predicts an instability all over the parameter space. This model-dependent instability has also been reported in previous literatures [89, 103], and is attributed to an effective negative compressibility. However, this instability has never been seen in our particle simulations, therefore is a spurious one due to the truncation of the closure. Thus we suppress this instability by setting $\lambda_3 = 0$. This leads to an imaginary part of the eigenvalue to the order q, therefore predicts a propagating hydrodynamic mode. The stability of this mode is determined by the sign of the real part of the eigenvalue to the order q^2, which leads to the condition in the absence of λ_3:

$$\frac{w_0\Omega_1\mu_1}{\mu_2} - \lambda_2 w_0^2 \Omega_1 > D_w\xi + \Omega_1\Omega_3 w_0^2, \tag{3.119}$$

or in terms of microscopic parameters

$$\gamma > \frac{(1+4\chi)(1+\chi)}{8\chi^2} + 4. \tag{3.120}$$

The phase diagram is plotted in Fig. 3.2 in the main text, with quantitative agreement between the numerical and analytical phase boundaries. This transverse instability renders the system spatially inhomogeneous with large density and spin fluctuations characterized by continuously turning and swirling flocks with propagating spin waves. Therefore, we term it the spin-wave instability. The spatial-temporal patterns have

been observed from both the numerical simulations of the hydrodynamic equations and particle simulations. To understand the origin of the instability, we write down the minimal equations that yield this instability. For clarity, we write down the dimensional form.

$$\partial_t \boldsymbol{w} = -\beta|\boldsymbol{w}|^2\boldsymbol{w} + \lambda_2\boldsymbol{w}(\boldsymbol{\nabla}\cdot\boldsymbol{w}) + \Omega_1\boldsymbol{S}\times\boldsymbol{w}\ , \tag{3.121}$$

$$\partial_t \boldsymbol{S} = -v_0\chi\boldsymbol{\nabla}\times\left(\beta|w|^2\boldsymbol{w}\right) - \xi\boldsymbol{S}\ , \tag{3.122}$$

where $\lambda_2 = -v_0\gamma\eta/(4\epsilon) - \gamma v_0\eta\eta_2/(16\epsilon\eta_1) < 0$, $\beta = \eta\gamma^2/(8\epsilon\eta_1)$, $\Omega_1 = \gamma/(2\eta\eta_1)$ and $\xi = \eta/\chi$. The linearized equations are

$$\partial_t\delta w_x = \mu_2 w_0\delta w_x + \lambda_2 w_0\partial_y\delta w_y\ , \tag{3.123}$$

$$\partial_t\delta w_y = \Omega_1 w_0\delta s_z, \tag{3.124}$$

$$\partial_t\delta s_z = -\mu_s w_0\partial_y\delta w_x - \xi\delta s_z, \tag{3.125}$$

where $\mu_2 = -2\beta w_0 < 0$ and $\mu_s = v_0\chi\mu_2 < 0$. They lead to the dispersion relation

$$\sigma(q) = -\frac{w_0^2\lambda_2\mu_s\Omega_1}{\xi\mu_2}q^2 + \mathcal{O}(q^3), \tag{3.126}$$

which yields the instability condition

$$\frac{w_0^2\lambda_2\mu_s\Omega_1}{\xi\mu_2} < 0. \tag{3.127}$$

This condition can be interpreted as the growth of bend and splay deformation augmented by the spin dynamics through self-rotation. If we include the alignment interaction through density, rotational diffusion and spin elasticity, all of which serve as stabilization factors, we recover the full condition 3.119. The competition among these effects yields the spin-wave instability.

3.11.4 Linear stability away from the disorder-order transition

Deep in the polar state, particularly for $\gamma > 50$, we observe homogeneous polar state, which is free of instabilities. In this regime, we refer to the hydrodynamic equations derived using the alternative closure as given by 3.90-3.92. The linearized equations have exactly the same structure as eqns. 3.105, but with a different relation between coefficients and microscopic parameters. The new set of coefficients yield banding instability if applied close to the transition, but lead to a stable homogeneous polar state deep in the polarized region in agreement with particle simulations. This can be attributed to

the suppression of spin-wave instability through strong alignment interaction, rotational diffusion and spin elasticity as shown by the same instability condition 3.119.

3.11.5 Angular-dependent spin wave

We can extract the propagating speed of the spin wave from the linearized equations. Along the direction of broken symmetry, the spin and director fluctuations decouple from the density and polarization magnitude fluctuations, leading to a damped wave equation with propagating speed $c_s = \sqrt{\Omega_1 \Omega_3} w_0$.

Along other directions making an angle θ with respect to the mean polarization, all the fluctuations are coupled, and the propagating mode is the hydrodynamic mode that also controls the stability of the system. This mode has a general dispersion relation as a function of θ.

$$c_s^{\pm}(\theta) = \frac{\mu_1}{2\mu_2} cos\theta \pm \sqrt{\frac{\mu_1^2 cos^2\theta}{4\mu_2^2} + \frac{1}{2} sin^2\theta}, \tag{3.128}$$

In the longitudinal direction, $c_s(0) = \frac{\mu_1}{\mu_2}$, corresponding to the propagating speed of the density band. In the transverse direction, $c_s(\pi/2) = \frac{1}{\sqrt{2}}$, corresponding to the propagating speed of the spin wave.

The fact that the spin wave is governed by two different modes with different propagating speed along the longitudinal and transverse directions renders the spin wave anisotropic, verified by the numerical solution of the hydrodynamic equations as in Fig. 3.4.

3.12 Appendix 3.E: Alternative alignment interaction

The polar alignment interaction can take up multiple forms. Thought it does not change the structure of the derived continuum equations in general, different form of polar interactions yields different coefficients which shifts the phase diagram. Here we discuss an alternative alignment interaction of the form

$$\tau = \delta(\boldsymbol{r}' - \boldsymbol{r}) sin[(\theta' - \theta)/2] \tag{3.129}$$

defined in the region $[-\pi, \pi]$. This interaction, upon Fourier transform, yields non-vanishing coefficients for all even moments

$$\tau_{\pm m} = -\frac{8m(-1)^m}{1 - 4m^2}, \tag{3.130}$$

which couples the density field to higher order moments in the Fourier transformed Fokker-Planck equation. This coupling yields more physical saturated polarization magnitude deep in the polarized state by introducing a new set of dimensionless coefficients in the continuum equations Eqns. 3.12-3.14.

$$\alpha(\rho) = \frac{1}{1+\chi}(1 - \frac{4\gamma\rho}{3\pi}), \quad \beta = \frac{28\gamma}{15\pi(1+\chi)}\frac{2\gamma/(3\pi)}{1+4\gamma/(15\pi)},$$
$$\Omega_1 = \frac{4\chi\gamma}{3\pi(1+\chi)}, \quad \Omega_2 = \frac{\chi}{2(1+\chi)}, \quad \Omega_3 = \frac{1}{1+\chi}\left[\frac{7(1+4\chi)}{8+30\pi/\gamma} - \frac{\chi\gamma}{3\pi}\right],$$
$$\lambda_1 = \frac{2\gamma/(3\pi)}{1+4\gamma/(15\pi)} - \frac{1}{1+\chi}\left[\frac{7(1+4\chi)}{8+30\pi/\gamma} - \frac{\chi\gamma}{3\pi}\right], \quad \lambda_s = \frac{4\chi\gamma}{3\pi(1+\chi)},$$
$$\lambda_3 = -\lambda_2 = \frac{2\gamma/(3\pi)}{1+4\gamma/(15\pi)} + \frac{1}{1+\chi}\left[\frac{7(1+4\chi)}{8+30\pi/\gamma} - \frac{\chi\gamma}{3\pi}\right],$$
$$\xi = \frac{1}{\chi}, \quad D_w = \frac{1+4\chi}{16[1+4\gamma/(15\pi)]}, \quad D_s = \frac{\chi}{2(1+\chi)}.$$

The structure of the equations remain unchanged. Deep in the polarized state, the saturated magnitude of polarization $w_0 = \sqrt{-\alpha_0/\beta}$ approaches a constant and proportional to the mean density ρ_0. Both the banding instability and spin wave instability are present in this case, with a slightly shifted parameter space as compared to the original alignment interaction.

Finally, we plot the phase diagram for this particular interaction based on the linear stability analysis below.

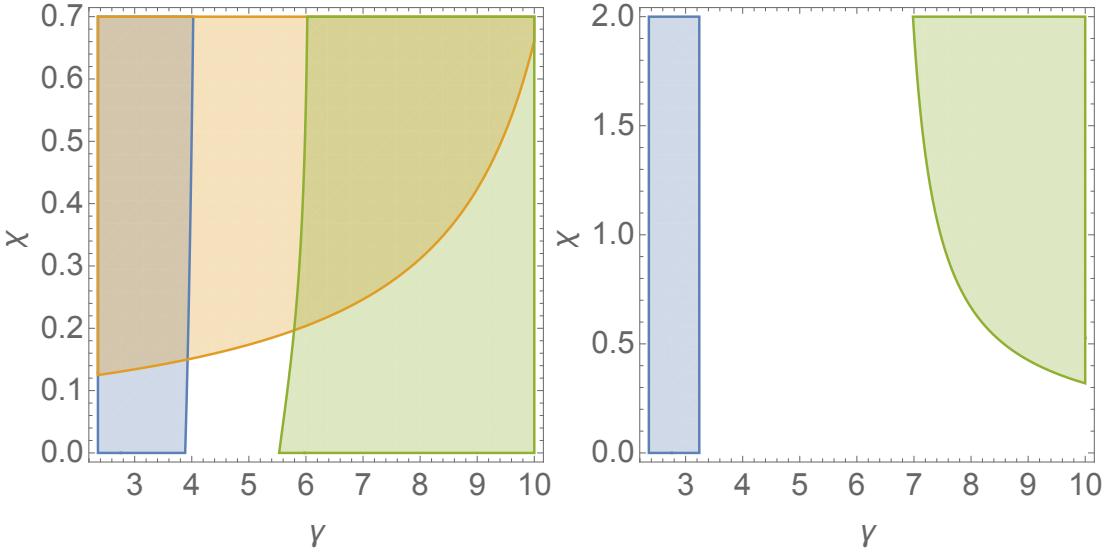

FIGURE 3.8: Phase diagram in the plane of dimensionless χ and γ for alignment interaction $\tau = \delta(\boldsymbol{r}' - \boldsymbol{r})sin[(\theta' - \theta)/2]$. Left: with λ_3. Right: without λ_3. Blue region:banding instability; orange region: transverse instability due to negative compressibility; green region: spin-wave instability.

Chapter 4

Mechanics of confined active particles

4.1 Introduction

Minimal models of self-propelled particles (SPP) have provided much insight into the emergent behavior of non-equilibrium, active systems where energy is injected at the scale of the individual constituents. This novel class of materials spans many length scales, ranging from bird flocks to bacterial swarms, cell layers and synthetic microswimmers [15]. Novel behaviors have been predicted theoretically and observed in simulations and experiments, including flocking [22], large density fluctuations [40, 104], and spontaneous phase separation [10, 36, 80]. Walls and confined geometries are ubiquitous in realizations of active systems. For example, sperm and bacteria often live near surfaces or in narrow channels, and these interfaces strongly affect their dynamics [32, 39, 105, 106]. Vibrated granular rods spontaneously accumulate at the walls even in the absence of hydrodynamic interactions [35, 107]. Finally, mixtures of two types of active particles have been studied as minimal models of cell sorting in co-cultures and have been shown to segregate in bulk in the presence of adhesive interactions [108–110].

In this paper we study a minimal model of athermal self-propelled disks with soft repulsive interactions confined to a box in two dimensions. The soft repulsive potential is chosen to provide finite energy barriers to particle crossing, as a way to mimic living cells that are capable of escaping to the third dimension and cross over each other. Each disk performs a persistent random walk consisting of ballistic runs at speed v_0, randomized by rotational diffusion at rate D_r. We find that confined self-propelled particles aggregate at the walls provided their rotational diffusion is sufficiently slow (Fig. 4.1(a)). At low density, aggregation occurs when a particle travels ballistically across the con-

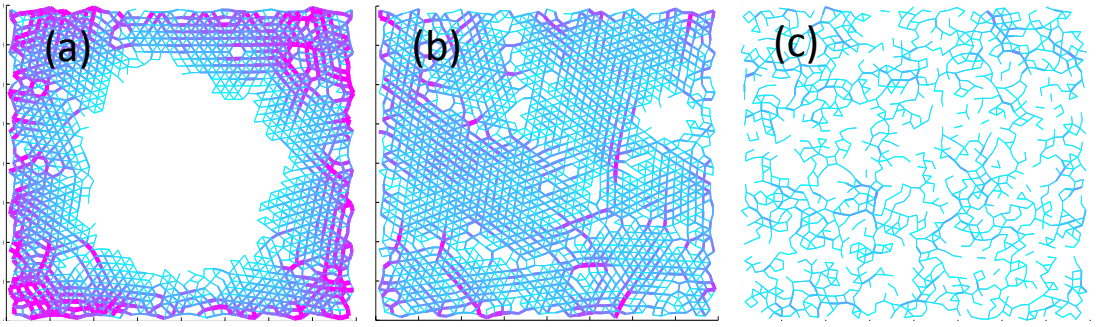

FIGURE 4.1: Force chains at time $T = 2000$ for $v_0 = 0.02$ displaying (a) aggregation at $D_r = 5 \times 10^{-5}$ and $\phi = 0.672$, (b) jammed state at $D_r = 5 \times 10^{-5}$ and $\phi = 0.896$, and (c) homogeneous gas state at $D_r = 0.005$ and $\phi = 0.672$. (†Supplementary Movies 1-3)

tainer. At high packing fraction ϕ, however, a critical active speed $v_c(\phi)$ is required for wall aggregation even in the limit $D_r \to 0$. The onset of a nonzero value of v_c in our active material correlates with the packing fraction at which non-active hard disks become "jammed" [111], i.e. exhibit a non-zero yield stress. The pressure of the active fluid, like the density, is spatially inhomogeneous as the particles seem to organize to optimally transmit stresses to the walls, as shown in Fig. 4.1(a). As the jamming point is approached, the system becomes more uniform (Fig. 4.1(b)) and the pressure begins to decrease with increasing density. This decrease occurs well below the jamming point and is associated with the onset of slow relaxation times due to strong caging effects that occur over a broad range of densities due to their activity. This non-monotonic dependence of pressure on density is unique to active systems. It is consistent with the non-monotonic dependence of pressure on temperature in a thermal active gas [112] and on system size in a dilute active gas [113]. Finally, this aggregation can be harnessed in a mixture of self-propelled particles of different sizes that segregates in the absence of any alignment or attraction (Fig. 4.3). The sense of the segregation (i.e., whether the large or the small disks accumulate on the outside) is determined by a mean field calculation for the energy barrier generated by the repulsive interaction. This segregation is reminiscent of cell sorting in embryonic development and is very different from the mechanisms that have been previously studied [114–118], which require differential cell adhesion or repulsion and postulate that cell sorting relaxes the tissue towards a free energy minimum, as in thermal systems.

4.2 Self-propelled particle model

We consider a system of N monodisperse disks of radius R in a square box of length L. The overdamped dynamics is governed by Langevin equations for the position $\mathbf{r}_i$ of the center of the i-th disk and a unit vector $\mathbf{u}_i = (\cos\theta_i, \sin\theta_i)$ along the axis of self

propulsion,

$$\partial_t \boldsymbol{r}_i = v_0 \boldsymbol{u}_i + \mu \sum_j \boldsymbol{F}_{ij} \ , \qquad \partial_t \theta_i = \eta_i(t) \ , \tag{4.1}$$

where v_0 is the active (self-propulsion) speed and μ the mobility. The particles interact via short-range repulsive forces $\boldsymbol{F}_{ij}$ proportional to the overlap between two disks, $\boldsymbol{F}_{ij} = k(2R - r_{ij})\hat{\mathbf{r}}_{ij}$, with $\mathbf{r}_{ij} = \mathbf{r}_i - \mathbf{r}_j = \hat{\mathbf{r}}_{ij} r_{ij}$, and k a force constant. The angular noise η is white, with $< \eta_i(t)\eta_j(t') >= 2D_r\delta_{ij}\delta(t-t')$ and D_r the rotational diffusion rate. Large immobile particles are glued to the walls of the box to implement the confinement and to suppress crystallization. At low density, each disk performs a persistent random walk and is diffusive at long times ($t \gg D_r^{-1}$), with an effective diffusion constant $D_a = v_0^2/2D_r$ [10]. We treat D_r as an independent parameter because in many realizations, including bacterial suspensions [46] and active colloids [11], the rotational noise is athermal. In these systems, D_a is also typically two orders of magnitude larger than the thermal diffusivity, and so we neglect thermal noise in Eq. (4.1).

Lengths and times are in units of the particle radius R and the elastic time $(\mu k)^{-1}$. Unless otherwise noted, the size of the box is $L = 83$. Particle positions are initialized with a uniform random distribution inside the box, and orientations are random over the interval $[0, 2\pi]$. Equations (4.1) are integrated numerically using an Runge-Kutta algorithm for $t = 9000$ time steps. This time interval is sufficient to ensure that the density profile of the system has reached steady state. We explore the behavior of the system by varying the active velocity v_0, the rotational diffusion rate D_r, and the packing fraction $\phi = N\pi R^2/L^2$ [1].

4.3 Self-organization

4.3.1 Wall aggregation

To quantify wall aggregation and the resulting density inhomogeneities we divide the system in n_Δ nested square strips of thickness Δ (Fig. 4.2(a)) and calculate the gini coefficient [119], given by $g = \frac{1}{2N^2|\bar{\rho}|}\sum_i \sum_j |\rho_i - \rho_j|$, with $\bar{\rho}$ the mean density, ρ_i the number density of particles in the i-th strip, and $\Delta = 2R$. The gini coefficient provides direct information of the spatial organization of density inhomogeneities. It approaches 0 when the density is homogeneous Fig.4.1(b)(c) and 1 when all particles are at the wall Fig.4.1(a). The boundary separating homogenous states from aggregated states where the particles accumulate at the walls is obtained by a linear fit to isosurfaces of the gini coefficient, and corresponds to $g = 0.5$, above which we say the system is wall-aggregated

[1] The values of packing fraction quoted below and in all figures have been adjusted to take into account the area occupied by the particles glued to the walls.

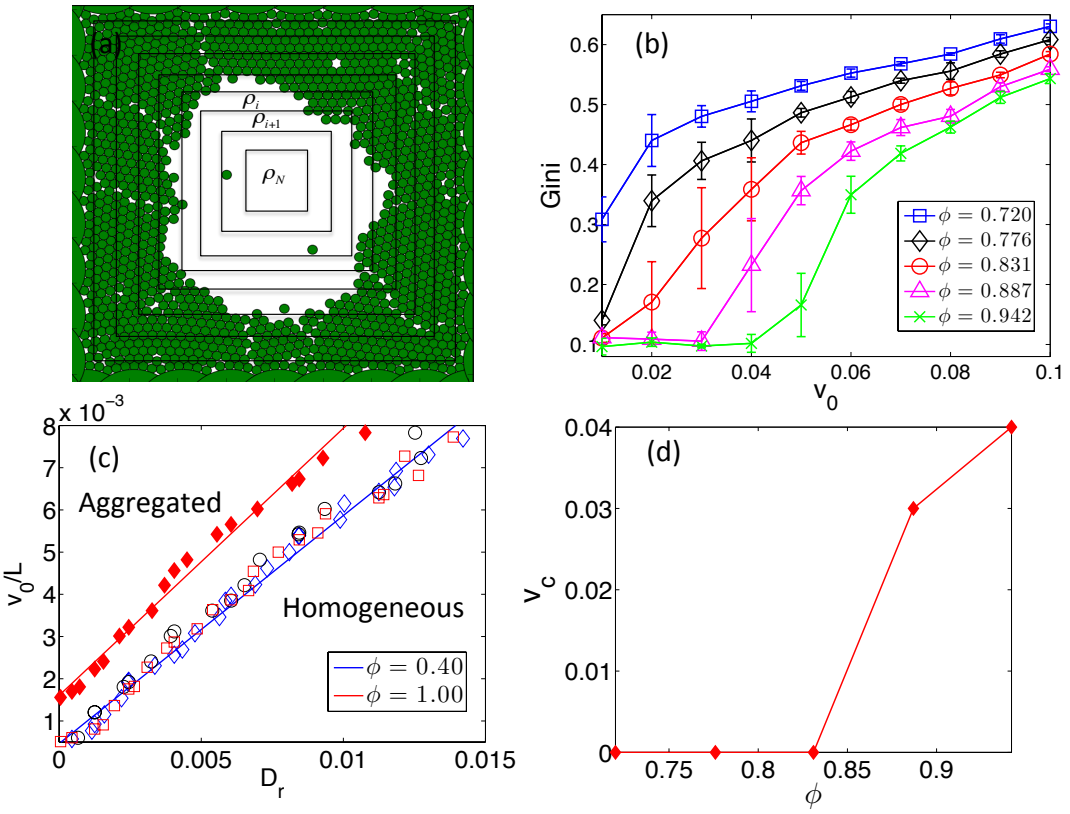

FIGURE 4.2: (a) Diagram of nested square strips. (b) Gini coefficient vs. v_0 at various packing fractions. The rotational noise is $D_r = 5 \times 10^{-5}$ and the total simulation time is $T = 9000$. (c) Phase boundaries separating aggregated and homogeneous states in the plane of v_0/L vs D_r. The open symbols are for $\phi = 0.40$ and $L = 83, 110, 130$ (circles, squares, diamonds). The straight line is a fit to that data with $v_0 = ALD_r$, where $A = 0.5402$. Filled diamonds are for $\phi = 1.00$ and $L = 83$. The total simulation time is $T = 2000$. (d) Critical speed at $D_r \to 0$ vs. packing fraction.

as shown in Fig 4.2 (c) for different values of ϕ. At low ϕ, aggregation occurs when D_r is small and particles travel ballistically across the container. The phase boundary is well-described by $v_0/L \propto D_r$, which is the solid line through the open circles in Fig. 4.2 (c). The gini coefficient increases continuously with v_0/D_r, consistent with the result in [39]. At high ϕ, a finite value $v_c(\phi)$ is required for wall aggregation even in the limit $D_r \to 0$, as shown by the solid line through the closed diamonds in Fig. 4.2 (c). The dependence on ϕ is seen in Fig. 4.2 (b), where the gini coefficient immediately rises from its minimal value for $\phi < 0.83$, and only rises at a finite v_c for $\phi > 0.88$. The critical v_c as a function of ϕ is shown in Fig. 4.2(d). The onset of a finite threshold for aggregation at $\phi \simeq 0.88$ coincides with the jamming point for monodisperse passive hard disks at zero temperature [111]. The result is also consistent with active jamming in a disordered landscape [120].

4.3.2 Active mixtures and segregation

The mechanisms responsible for athermal phase separation [10] and wall aggregation of purely repulsive self-propelled particles have remarkable consequences in mixtures. We simulate a binary mixture of small (S) and large (L) self propelled particles with diameter ratio 1.4 to prevent crystallization. Although different in size, they interact via the same harmonic soft repulsive potential, with *equal* force constants $k_{SL} = k_{SS} = k_{LL}$, and with dynamics described by Eqs. (4.1). The self-propulsion speeds are v_S and v_L respectively, and to reduce the number of parameters we have assumed equal mobilities for both types of particles. To quantify the spatial distribution of the two particle types,

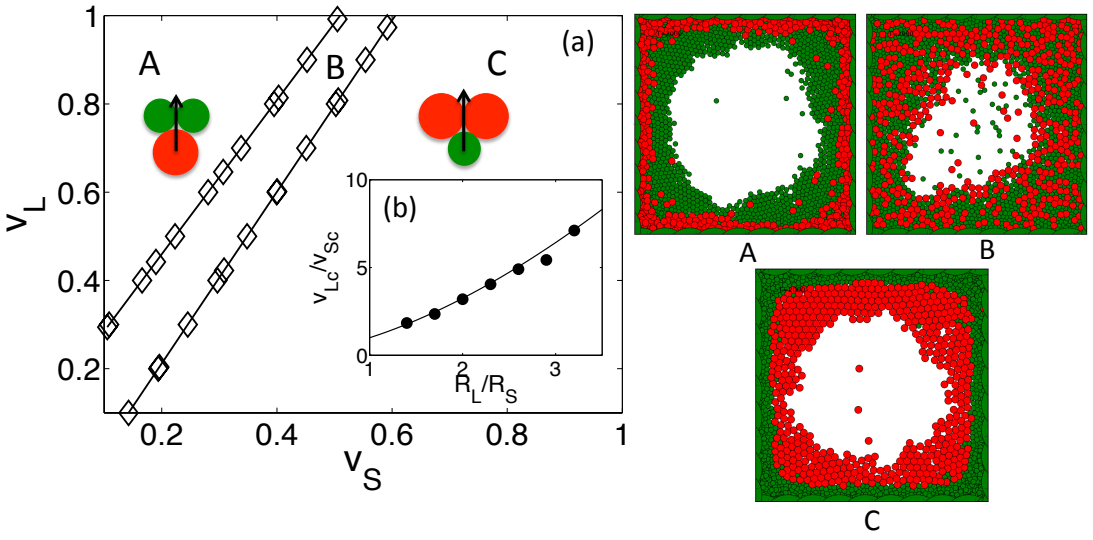

FIGURE 4.3: (a) Phase diagram showing the segregated and homogeneous states as functions of the active velocities v_S and v_L (small particles are green and large ones are red) for $D_r = 5\times10^{-5}$ and a total packing fraction $\phi = 0.9$, with each species occupying half of the packing fraction. (b) Analytical calculation identifying when particles with a given active velocity and radius ratio are able to overcome mean-field elastic energy barriers (solid line). Onset of particle segregation in simulations (data points). The remarkable agreement with no fit parameters demonstrates that segregation is driven by asymmetric elastic energy barriers. A-C are snapshots of segregated and homogeneous states. The labels A, B, C correspond to the states marked in the phase diagram.

we define a segregation coefficient S:

$$S = \frac{\sum_i |\rho_i^L - \rho_i^S|}{\sum_i \max[\rho_i^L, \rho_i^S]} \tag{4.2}$$

where the shell width Δ is the large particle diameter and $\rho_i^{S,L}$ is the density of small-/large particles in the i-th shell. With this definition, $S \to 0$ for a uniform distribution of L and S disks, and $S \to 1$ for complete segregation.

When these purely repulsive disks are exactly the same except for their size ($v_S = v_L$), the system spontaneously segregates so that the small particles aggregate near the walls and the large particles are closer to the center of the box. We choose a critical value of $S = 0.5$ to differentiate segregated state from mixed state.

To better understand this surprising result, we study a phase diagram of the segregation as a function of the two self-propulsion speeds v_S and v_L, shown in Fig. 4.3. We find three distinct states: (A) a segregated state where all the large (red) disks have accumulated at the wall, with the small (green) ones closer to the center, (B) a mixed state where the particles have accumulated at the wall, but they are homogeneously distributed, hence $S \sim 0$ and (C) a segregated state where the small disks are near the walls and the large ones are near the center. The lower left hand corner of Fig 4.3 demonstrates that if both the small and large particle velocities are too small, the system remains mixed. This suggests that particles must overcome a finite energy barrier in order to segregate. To quantify and test this assumption, we let v_{Sc} (v_{Lc}) denote the critical velocity of the small (large) particles in the limit $v_L \to 0$ ($v_S \to 0$). To estimate v_{Sc}, we derive an analytic expression for the velocity required for an active small particle to cross through two immobile large particles in contact with zero overlap, assuming that the small particle is moving directly perpendicular to the pair, as illustrated in Fig. 4.3.

To evaluate the barrier that particles must overcome for segregation, we consider the geometry shown in Fig. 4.4 displaying a small active particle of radius R_S that has to make its way through two immobile large particles of radius R_L. For the small particle to travel through the barrier imposed by the two large ones, the active force v_0/μ has to overcome the maximum of the repulsive force F_{rep}. This defines a critical active velocity v_{Sc} for the small particle. To calculate this barrier we assume that the small active particle initially just touches its neighbors, then travels upward a distance of d. At this point, the net repulsive force is

$$F_{rep} = 2F sin\theta \ , \tag{4.3}$$

where $F = k[(R_L + R_S) - \sqrt{(l-d)^2 + R_L^2}]$ is the repulsive force between two particles and $sin\theta = l'/s$. Geometrical considerations lead to $l' = l - d$, $s = \sqrt{(l-d)^2 + R_L^2}$ and $l = \sqrt{r^2 + 2R_S R_L}$, allowing us to express F_{rep} solely in terms of d.

The critical active velocity v_{Sc} is defined as the maximum value of $\mu F_{rep}(d)$. This gives

$$\begin{aligned} v_{Sc} = 2\mu k[(R_L + R_S)R_L^2]^{1/3}[1 - (1 + \frac{R_S}{R_L})^{-2/3}]^{1/2} \\ \times[(1 + \frac{R_s}{R_L})^{2/3} - 1] \ . \end{aligned} \tag{4.4}$$

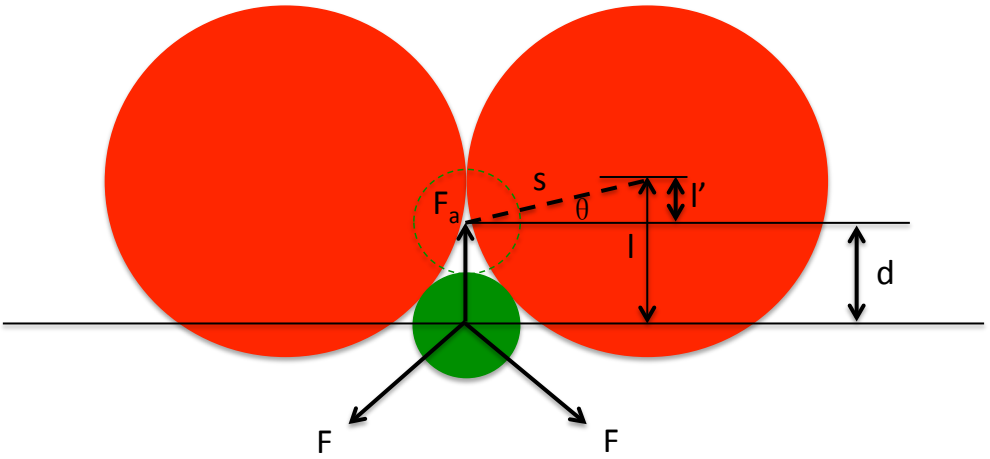

FIGURE 4.4: Minimal model used to evaluate the barriers of segregation: a small active particle pushing its way through two adjacent, immobile large particles. R_S and R_L are the particles' radii. The small particle initially just touches its neighbors, then travels a distance d vertically with active velocity $F_a = v_0/\mu$. F is the repulsive force between two particles. Other geometrical quantities are as labelled.

This is the critical velocity of an active particle with radius R_S pushing through two immobile particles of radius R_L. The critical velocity for the reversed configuration, corresponding to a particle of radius R_L pushing through two particles of radius R_S, can be obtained by interchanging R_S and R_L. Segregation occurs when either species has an active velocity above the critical value. Note that particles with different radii have different critical velocities. If, for instance, $R_S < R_L$, then $v_{Sc} < v_{Lc}$, and small particles will aggregate to the outside, next to the wall, when both species have the same active velocity.

Finally, the ratio of active velocities of the two species can be written as a function of their radii ratio as

$$\frac{v_{Lc}}{v_{Sc}} = x^{-\frac{2}{3}} \frac{[1-(1+x)^{-2/3}]^{\frac{1}{2}}[(1+x)^{2/3}-1]}{[1-(1+\frac{1}{x})^{-2/3}]^{\frac{1}{2}}[(1+\frac{1}{x})^{2/3}-1]}\,, \tag{4.5}$$

where $x = R_L/R_S$.

This is a mean-field theory for energy barriers in a system exactly at the jamming transition. While the data in Fig. 4.3(a) are for a bidisperse mixture with diameter ratio 1.4, we calculate the velocity ratio as a function of the diameter ratio $x = R_L/R_S$, obtaining

$$\frac{v_{Lc}}{v_{Sc}} = x^{-\frac{2}{3}} \frac{[1-(1+x)^{-2/3}]^{\frac{1}{2}}[(1+x)^{2/3}-1]}{[1-(1+\frac{1}{x})^{-2/3}]^{\frac{1}{2}}[(1+\frac{1}{x})^{2/3}-1]} \tag{4.6}$$

This function $\frac{v_L}{v_S}(x)$ is plotted in Fig 4.3(b) as a solid line. We then extract numerical values of v_{Lc}/v_{Sc} from the segregation boundary in simulations with different values

of R_L/R_S. These numerical results are the data points in Fig 4.3 (b). The remarkable overlap between the theory and simulation suggests that our mean field theory is valid and that asymmetric energy barriers for particles moving across one another are responsible for segregation.

We emphasize that the phenomenon of active segregation is intrinsically different from the "Brazil Nut Effect"[121], where a bidisperse granular mixture segregates under external shaking. Our soft active particles are individually driven rather than agitated through boundary forces. As a result, size segregation in our active system is driven by the asymmetry of the energy barriers imposed by soft repulsive interaction between particles as supported by the outstanding agreement between analytical and numerical results shown in Fig 4.3(b), rather than by the "void-filling" [121] or "granular convection" [122] mechanisms proposed to explain the "Brazil Nut Effect".

4.4 Pressure

To quantify force distribution in our active fluid, we have evaluated the pressure both in the homogeneous and wall-aggregated states. We define the pressure using the Irving-Kirkwood (IK) expression for the stress tensor given below [123], augmented by a contribution from self-propulsion. We have checked that this yields the same result as measuring the force per unit length on the walls of the container at all packing fractions. This demonstrates that the generalized IK formula proposed below is the correct expression for evaluating the mechanical pressure of an active system. The stress tensor $\sigma_{\alpha\beta}$ (with $\alpha, \beta = x, y$) is naturally separated in a contribution from interactions and an active contribution, as $\sigma_{\alpha\beta} = \sigma^{int}_{\alpha\beta} + \sigma^{a}_{\alpha\beta}$, with

$$\sigma^{int}_{\alpha\beta} = \frac{1}{L^2}\Big\langle \sum_{i\neq j} F^{\alpha}_{ij} r^{\beta}_{ij} \Big\rangle, \;\; \sigma^{a}_{\alpha\beta} = \frac{1}{L^2}\Big\langle \sum_{i} F^{\alpha}_{i,a} r^{\beta}_{i} \Big\rangle, \tag{4.7}$$

where $\mathbf{F}_{i,a} = (v_0/\mu)\mathbf{u}_i$ is the active force on each disk. The pressure is the trace of the stress tensor, $P = \sigma_{\alpha\alpha}/2 = P_{int} + P_a$, shown in Fig. 4.5(a) as a function of ϕ for a small rotational diffusion rate $D_r = 5 \times 10^{-5}$. For small D_r, where the system aggregates at the walls and exhibits strong density and pressure inhomogeneities (Fig. 4.1(a)), the pressure is a strongly non-monotonic function of density and starts decreasing at $\phi \simeq 0.672$, well below jamming. At this packing fraction the density gradients start to smoothen, and the pressure becomes more homogeneous, as shown in Fig. 4.6(a), which displays the interaction force between particles as a function of distance to the wall. Fig. 4.6(b) shows the gini coefficients of density and pressure, demonstrating that the pressure inhomogeneity is a direct consequence of density inhomogeneity. Meanwhile,

particles are caged by their neighbors. This leads to "self-trapping", resulting in a suppression of their effective self-propulsion speed, as discussed in recent work on active phase separation [10, 17, 36, 80, 124, 125]. In this region, although the system is fairly homogeneous, the transmission of force is impeded by crowding, resulting in an increased effective rotational diffusion rate and a sharp decrease in pressure. This description is supported by the correlation between the compressibility and homogeneity of the system, Fig 4.6(b). The decrease in the forces that particles are able to transmit to the walls is most dramatic in the active pressure, that seems to essentially vanish near $\phi = 0.907$, the packing fraction corresponding to perfect crystalline order in a triangular lattice. Fig. 4.5(b) shows that the pressure non-monotonicity diminishes with increasing D_r, and the active system exhibits thermal-like behavior when $v_0/L \ll D_r$, as suggested by the curve of filled circles. The analogy with a thermal system and the notion of effective temperature can, however, be made precise only in the low density limit. At finite density, repulsive interactions affect the active system quite differently from its thermal counterpart even in the limit of large D_r, and the pressure of the thermal system increases much faster than the active one, as shown in Appendix 4.A. In all cases, the pressure increases steeply above $\phi \simeq 0.88$ due to enforced overlap.

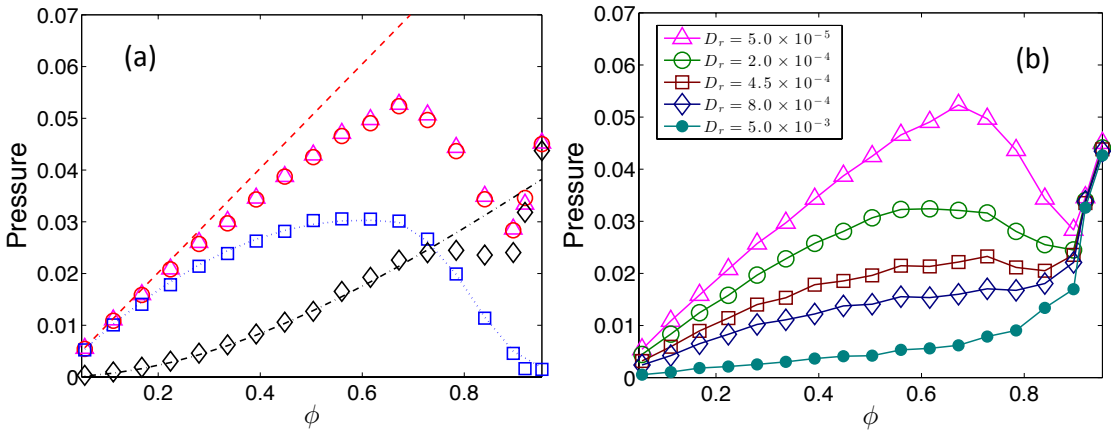

FIGURE 4.5: (a) Total pressure calculated from the IK formula (triangles) and as the force on the walls (circles) as a function of packing fraction at $v_0 = 0.02$ and $D_r = 5 \times 10^{-5}$. The two calculations yield the same result. Also shown are the interaction (black diamond) and active (blue squares) contributions to the pressure. The dashed magenta line is the calculated ideal gas pressure with no fitting parameters. The black dot-dashed line is the calculated interaction pressure with $c = 1.2$. The blue dotted line is the calculated active pressure with a density-dependent active velocity $v(\phi)$ and effective rotational diffusion rate $D_r^{eff}(\phi)$. (b) Total pressure for various rotational noise D_r.

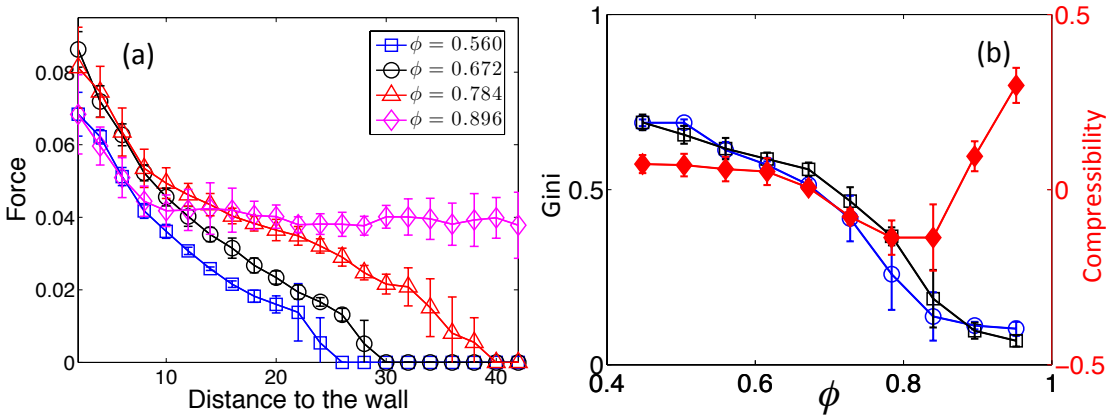

FIGURE 4.6: (a) Interaction force as a function of distance to the wall for various packing fractions ϕ. (b) Gini coefficient of density (circles), gini coefficient of force (squares) and compressibility (filled diamonds) vs. packing fractions at $v_0 = 0.02$, $D_r = 5 \times 10^{-5}$.

4.4.1 Active pressure

The active pressure can be calculated analytically at low density from the Langevin equations (4.1) neglecting interactions. The result corresponds to the pressure of an active ideal gas, also discussed in [126, 127]. Using $\langle u_{i\alpha}(t)u_{j\beta}(t')\rangle = e^{-D_r|t-t'|}\delta_{ij}\delta_{\alpha\beta}$, we find $P_0(t) = \frac{\rho v_0^2}{2\mu D_r}\left(1 - e^{-D_r t}\right)$ for the ideal active gas pressure. In a container of side L, active particles eventually get stuck at the wall. For small, but finite D_r, we then define the ideal gas active pressure as $P_0 = P_0(t = L/v_0)$, where L/v_0 is the time required by an active particle to travel ballistically through the container. The resulting expression

$$P_0 = \frac{\rho v_0^2}{2\mu D_r}\left(1 - e^{-D_r L/v_0}\right) \tag{4.8}$$

interpolates between the thermal limit $P_0 \approx \rho v_0^2/(s\mu D_r)$ for $D_r \gg v_0/L$ and the value $P_0 \approx \rho v_0 L/(2\mu)$ for $D_r \ll v_0/L$ corresponding to N disks each exerting a uniform force v_0/μ on the walls. The ideal pressure of an active gas is shown in Fig. 4.5(a) as a dashed line and fits the data at low density. At moderate density the pressure remains a monotonically increasing function of density, but is suppressed relative to the ideal gas expression. This deviation can be understood as arising from "self-trapping", which yields a density-dependent effective active velocity [10] $v(\phi) = v_0(1-\lambda\phi)$. At high density, however, the active pressure shows a nonmonotonic behavior and decreases with increasing density. This nonmonotonicity is indicative of strong caging and cannot be described solely in terms of a suppression of active speed. A mean-field formula that fits the pressure over the entire range of density can be obtained by assuming that caged active particles repeatedly change direction of motion due to interaction, resulting in an enhanced effective rotational diffusion rate, $D_r^{eff}(\phi) = \Theta(\phi - \phi_c)\exp[\alpha(\phi - \phi_c)]$, which characterizes the rate of change in the direction of the actual velocity $\boldsymbol{v}_i = \partial_t \boldsymbol{r}_i$,

with $\Theta(\phi - \phi_c)$ the Heaviside step function, and ϕ_c the critical packing fraction above which this caging effect kicks in. We emphasize that this occurs well below jamming and ϕ_c generally depends on the active speed v_0. A fit to this mean-field theory that incorporates density-dependent velocity and rotational diffusion rate is shown in Fig. 4.5(a) as a dotted line.

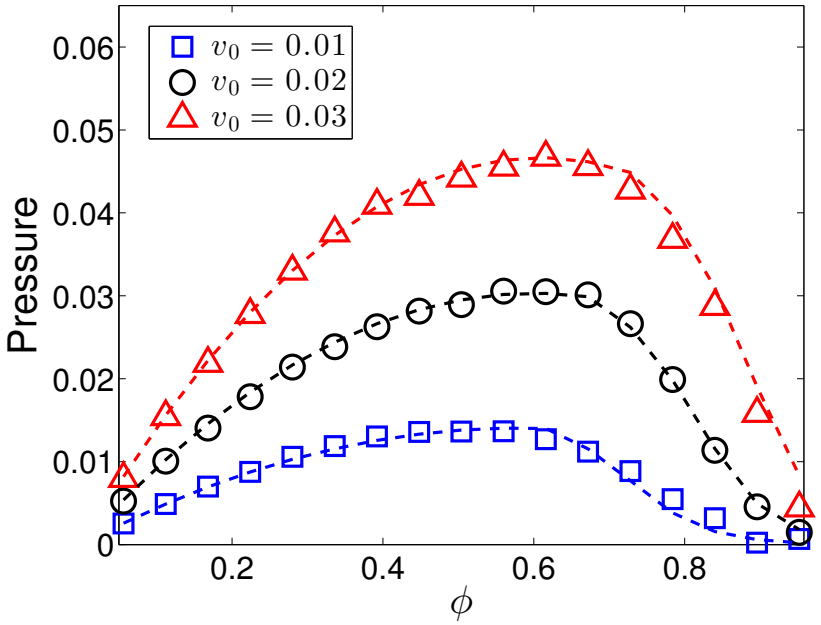

FIGURE 4.7: Markers: Active pressure as a function of packing fraction for various active speeds v_0 and $D_r = 5 \times 10^{-5}$. Dashed line: Fitting using expression of ideal active gas pressure with density-dependent velocity and density-dependent effective rotational diffusion rate.

The suppression of self-propulsion due to caging can be incorporated in a mean-field fashion by replacing the active speed v_0 in the ideal gas pressure by a density-dependent speed $v(\phi)$, as suggested by recent work on phase separation of active particles [10]. We also speculate that crowding effectively increases the rate of rotational diffusion as particles rattle around the confining cage and incorporate this effect into a density-dependent effective rotational diffusion rate $D_r^{eff}(\phi)$, which is enhanced at packing fraction above ϕ_c, where the active pressure starts to decrease sharply. A fit to the active pressure for various active speeds v_0 using the ideal gas formula $P_0 = \frac{\rho v_0^2}{2\mu D_r}\left(1 - e^{-D_r L/v_0}\right)$ with $v(\phi) = v_0(1 - \lambda\phi)$ replacing v_0 and $D_r^{eff}(\phi) = \Theta(\phi - \phi_c)\exp[\alpha(\phi - \phi_c)]$ replacing D_r, where $\Theta(\phi - \phi_c)$ is the Heaviside step function, is shown in Fig. 4.7 as dashed lines. The fitting parameters are $\lambda = 0.8$ and $\alpha = 13$. The critical packing fraction ϕ_c increases with active speed v_0, where $\phi_c = 0.616,\ 0.672,\ 0.728$ corresponds to $v_0 = 0.01,\ 0.02,\ 0.03$ respectively. This suggests that activity counteracts the effect of crowding, which is consistent with the "unjamming" of the system as activity increases (Fig. 4.2(b)).

4.4.2 Interaction pressure

On the other hand, a simple expression for the interaction pressure can be obtained by modeling the system as concentric layers of particles aggregated at the walls and assuming that the particle overlap, hence the force that each layer exerts on the walls, increases linearly as the wall is approached. For simplicity, we consider a completely aggregated state, where the active force is balanced by the interaction force. We work in a coordinate system with axes along the principal direction of the stress tensor, and therefore drop the label of component for force and particle position. The trace of the stress is then given by

$$\sigma_{\alpha\alpha} = \frac{1}{L^2} \sum_{i \neq j} F_{ij} r_{ij} \ , \tag{4.9}$$

where the summation is over all interacting pairs. As illustrated in Fig 4.8, the interaction forces are transmitted through chains of particles, resulting in a larger interaction force/stress closer to the wall. Given that our repulsive force is a linear function of overlap, we assume that the stress increases linearly as the wall is approached. This assumption is supported by Fig 4(a) in the paper. To proceed, we divide the system into

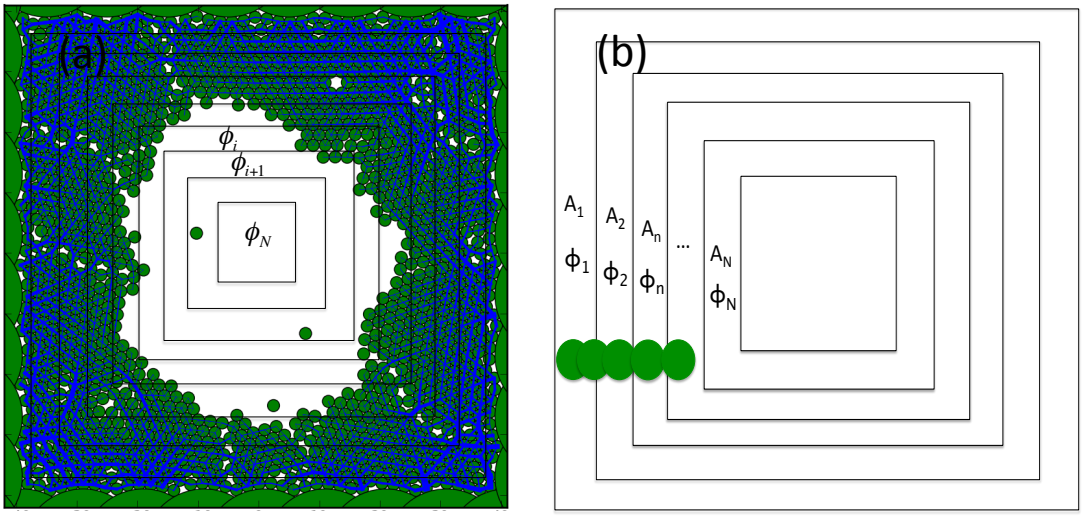

FIGURE 4.8: (a) Snapshot of an aggregated state with force chains (blue). The nested particle layers are also displayed. The overlap between particles increases as they approach the wall, indicating an inhomogeneous distribution of pressure, which is maximum at the wall, as shown by the force chains. (b) The aggregated state is modeled as a collection of N nested layers of particles, with a linear increase of overlap (or pressure) as the wall is approached. Each layer has area A_n and is occupied by active particles of packing fraction ϕ_n.

N nested particle layers, as shown in Fig 4.8. Each layer has the width of a particle diameter $2R$, area A_n and occupies a fraction $\phi_n = A_n/L^2$ of the entire system's area. We assume that ϕ_n is also the packing fraction of particles in the n-th layer. Approximating

the area of a layer as the sum of the area of four equal strips, we can write

$$A_n = 8LR - 32R^2(n-1) \; . \tag{4.10}$$

We assume that the total packing fraction ϕ of the system is equal to the sum of ϕ_n,

$$\phi = \sum_{n=1}^{N} \phi_n = \frac{1}{L^2}\left(8LRN + 16NR^2 - 16R^2N^2\right) \; . \tag{4.11}$$

Solving Eq. (4.11) for N in terms of ϕ, we obtain

$$N \simeq \frac{L}{8R}\phi + \mathcal{O}(R/L) \; . \tag{4.12}$$

Now we proceed to calculate the stress. When the system is completely aggregated, the interaction forces are balanced by the active forces $F_a = v_0/\mu$. Assuming that the force increases linearly as we approach the wall, and imposing force balance between the interaction force F_{ij}^n on particle i in the n-th layer due to particle j in the $n-1$ layer and the active forces, we can write

$$F_{ij}^n = (n-1)F_a = (n-1)\frac{v_0}{\mu} \; . \tag{4.13}$$

The stress in the nth layer is then given by

$$\sigma_{\alpha\alpha}^n = \frac{1}{A_n}\sum_{i\neq j} F_{ij}^n r_{ij}^n \; . \tag{4.14}$$

Inserting Eq. (4.13), we obtain

$$\sigma_{\alpha\alpha}^n = \frac{1}{A_n}\sum_{1}^{CN_n/2} (n-1)\frac{v_0}{\mu}[2R - (n-1)\frac{v_0}{k\mu}] \; , \tag{4.15}$$

where C is a fitting parameter corresponding to the average contact number of a particle and N_n is the number of particles in the nth layer. Expanding Eq. (4.15) and keeping only terms to lowest order in v_0, we obtain

$$\sigma_{\alpha\alpha}^n = c\phi_n(n-1)v_0 \; , \tag{4.16}$$

where $c = \frac{C}{\pi R\mu}$ is a rescaled fitting parameter. Using $\phi_n = \frac{A_n}{L^2}$ and summing over the layers, we obtain an expression for the total stress as

$$\begin{aligned} \sigma_{\alpha\alpha} &= \sum_{n=1}^{N} \sigma_{\alpha\alpha}^{n} \simeq \int_{1}^{N} \sigma_{\alpha\alpha}^{n}(n)dn \\ &= \int_{1}^{N} \left[\frac{8Rcv_0}{L}(n-1) - \frac{32R^2cv_0}{L^2}(n-1)^2 \right] dn \end{aligned} \tag{4.17}$$

where the sum over layers has been replaced by an integration. Carrying out the integration we find

$$\begin{aligned} \sigma_{\alpha\alpha} &= \frac{4Rcv_0}{L}(N-1)^2 - \frac{32R^2cv_0}{3L^2}(N-1)^3 \\ &\simeq \frac{4Rcv_0}{L}N^2 - \frac{32R^2cv_0}{3L^2}N^3 = c\left(\frac{Lv_0}{16R}\phi^2 - \frac{Lv_0}{48R}\phi^3\right) \end{aligned} \tag{4.18}$$

The pressure of the system is defined as

$$P = \frac{\sigma_{\alpha\alpha}}{2} \tag{4.19}$$

To fit the data for $k = 1$, $\mu = 1$, $R = 1$ and $L = 80$ yields $c = 1.2$, corresponding to an average contact number of 6. This estimate, gives $P_{int} = c\left(\frac{Lv_0}{16R}\phi^2 - \frac{Lv_0}{48R}\phi^3\right)$, with c a fitting parameter. A fit to this expression with $c = 1.2$ is shown in Fig. 4.5.

4.4.3 Finite size effect

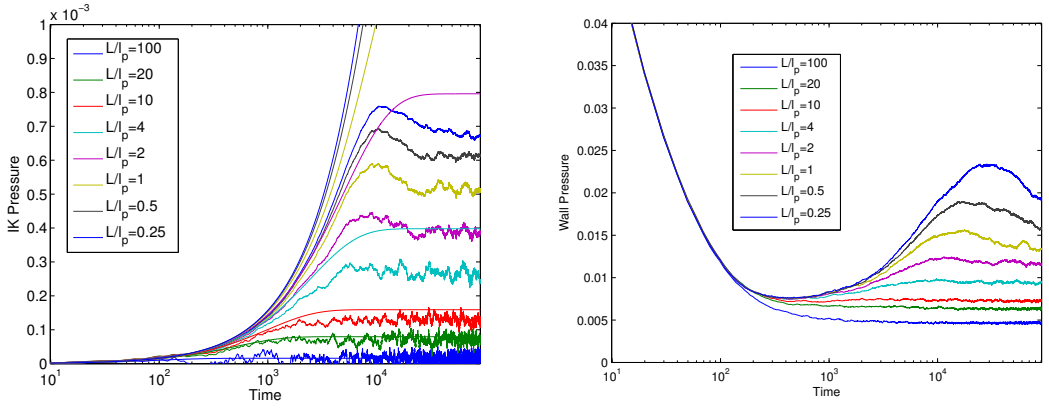

FIGURE 4.9: Time evolution of pressure in confined SPP system at various persistence length. Left: dilute limit at $\Phi = 0.01$. Right: dense limit at $\phi = 0.80$

In the dilute limit, the ideal active gas pressure reads $P_0(t) = \frac{\rho v_0^2}{2\mu D_r}\left(1 - e^{-D_r t}\right)$. However, for a finite system, this expression fails to fit the data at long times (Fig.4.9) due to the fact that there is an upper bound for the time set by $T = L/v_0$, the time required by an active particle to travel ballistically through the container. This leads to an saturated

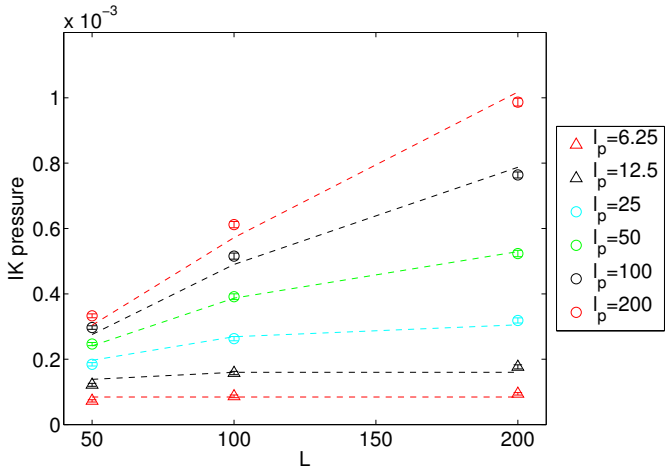

FIGURE 4.10: IK pressure in confined system at dilute limit $\phi = 0.01$ as a function of system size at various persistence length. Dashed line is the fitting using Eqn.4.20

value of the active pressure

$$P_0(t \to \infty) = P_0(t = L/v_0) = \frac{\rho v_0^2}{2\mu D_r}\left(1 - e^{-L/l_p}\right), \tag{4.20}$$

where $l_p = \frac{v_0}{D_r}$ is the persistence length. This expression matches with the simulation data quite well in Fig. 4.10.

Finally, in the dense limit, the time evolution of total pressure is non-monotonic with a long relaxation tail at large persistence length (Fig. 4.9).

4.5 Appendix 4.A: Effective temperature

In the limit $v_0/L \ll D_r$ the pressure of an ideal active gas given in Eq. (4.8) takes the form of the pressure of an ideal thermal gas, with an effective temperature $k_B T_{\text{eff}} = v_0^2/(2\mu D_r)$, corresponding to a thermal diffusivity $D_t = \mu k_B T_{eff} = \frac{v_0^2}{2D_r}$. This suggests that in this limit it may be possible to map the active system onto a thermal one with an effective temperature. Figure 4.11 compares the pressure of an active gas for $v_0 = 0.02$ and $D_r = 0.005$ to that of a thermal gas with the corresponding value $D_t = 0.04$. Also shown is the analytical expression of Eq. (4.8). Although the three curves overlap at very low density, the pressure of the thermal gas rises much more rapidly than that of the active gas with increasing packing fraction, indicating that repulsive interactions are more effective in building up pressure in the thermal system. Surprisingly, the pressure in the active system falls slightly below the active ideal gas limit at intermediate packing fractions.

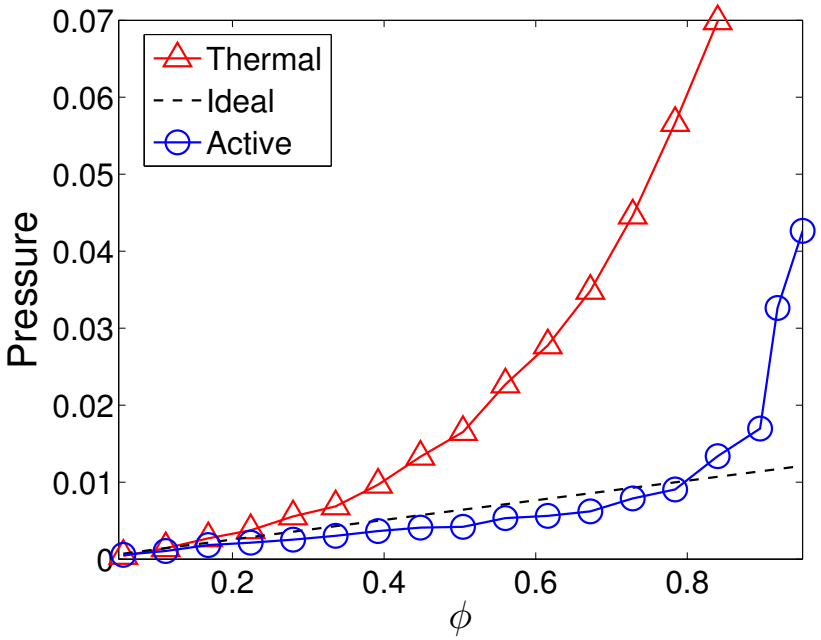

FIGURE 4.11: Pressure as a function of packing fraction for an active system with $v_0 = 0.02$, $D_r = 0.005$ and $L = 80$ (blue circles) and of a thermal system with $D_t = 0.04$ (red triangles). The black dashed line is the calculated expression for pressure for the ideal active gas pressure given in Eq. (4.8).

4.6 Appendix 4.B: Numerical simulations

We outline the procedures to perform molecular dynamic simulations for the SPP model based on the equations of motion 4.1.

- Initialize the positions and orientations of the particles using a random number generator to generate a homogeneous and disordered configuration.
- Construct a neighbor list by sorting particles based on their positions into cells with the length of the cell edge no less than the range of the interactions.
- Update the positions and orientations of the particles by integrating the equations of motion 4.1. The interactions are only calculated between particles in the same cell (red in Fig.4.12), or in the neighboring cells (green in Fig. 4.12). The white noise in the orientation is realized by adding a random number drawn from a Gaussian distribution with variance $\sqrt{2D_r dt}$ to the angular displacement, where dt is the time step increment of the simulation.
- Construct a new neighbor list based on the updated particle positions, and repeat step 3.

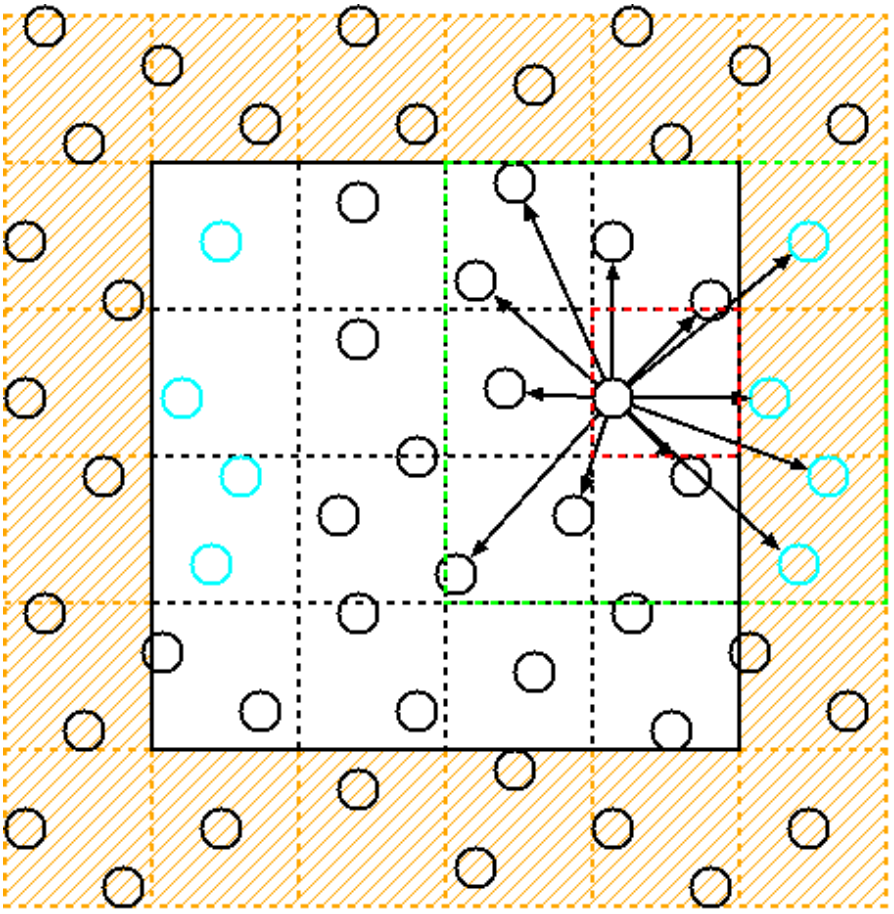

FIGURE 4.12: Diagram for the neighbor list in the MD simulations for SPP model. The particles are sorted based on their positions into cells with the cell length no less than the range of the interactions. The interactions are calculated only between particles in the same cell, or in neighboring cells (arrows). In the case of periodic boundary condition, the simulation box is wrapped by the images of the system, with interactions between particles and corresponding images in the neighboring cells.

Chapter 5

Active Self-assembly

5.1 Introduction

Self-assembly describes the process in which independent constituents of a dynamical system self-organize into ordered structures as a result of the local interactions among the components themselves. Examples include the formation of lipid bilayers in cytoplasm membranes, the aggregation of surfactant molecules into micelles, and the gelation of DNA-coated colloids [128]. The energy source and interactions can be of various natures. It is known that depletion interactions can drive aggregation of thermal particles due to pure entropic effect [129, 130]. In the presence of short-range attraction, one can tune the morphology of the final phase by tuning the strength and direction of the interactions, leading to kinetic arrest from different pathways, which makes programmed self-assembly possible [131].

In recent years, the studies of active systems far away from equilibrium with self-driven units have yielded striking dynamical properties distinct from their thermal counterparts. Motility induced phase separation (MIPS) and kinetically arrested gelation have been observed in self-propelled particle systems with and without attractive interactions [132]. Spontaneous segregation has been seen in a mixture of active and passive particles with isotropic [133] or elongated shapes [110]. Crystallization of hard-sphere glasses by doping with active particles has been reported [134]. Recently, an active counterpart of depletion interaction has also been investigated [135]. These concepts have been partially tested in experimental set-ups such as the mixture of swimming bacteria in colloidal suspensions [136].

While a majority of the focus in the aforementioned literature has been on the phase behaviors of active systems, the literature of self-assembly in active systems are still quite

limited, especially the studies of active-passive mixtures. Given the understanding of the dynamical and mechanical properties of a single component self-propelled particle (SPP) model, we are well-equipped to study the self-assembly of an active-passive mixture. An interesting question I am attempting to address in this chapter is:*how does an active bath composed of self-propelled particles drive the assembly of attractive and repulsive passive particles as compared to a thermal bath?*

The minimal active bath is composed of self-propelled particles with isotropic repulsive interactions among themselves and with the immersed passive particles. Each self-propelled particle is characterized by a dimensionless Péclet number defined as the persistence length divided by the particle size. This number, together with the ratio of packing fractions between the active and passive components, controls the dynamics of the self-assembly of the immersed passive particles. The interactions among passive particles are also important, and we discuss two kinds of interactions: short-range attraction and repulsion.

5.2 Model

Let's consider an active-passive mixture in 2D with passive particles immersed in a self-propelled particle bath. The dynamics of the passive component, which we label as red, is controlled by the following overdamped equations of motion:

$$\partial_t \boldsymbol{r}_i^r = \mu \sum_j \boldsymbol{F}_{ij} \ , \tag{5.1}$$

where $\boldsymbol{F}_{ij}$ is the interaction forces and μ is the mobility. Notice that the passive particles have no independent dynamics, and are completely stationary in the absence of collisions. The dynamics of the self-propelled particles, which we label as green, is described by:

$$\partial_t \boldsymbol{r}_i^g = v_0 \boldsymbol{n}_i^g + \mu \sum_j \boldsymbol{F}_{ij} \ , \qquad \partial_t \theta_i^g = \eta_i^r(t) \ , \tag{5.2}$$

where v_0 is the constant self-propulsion speed along the direction of the polarization vector $\boldsymbol{n}_i^g$. The polarization vector is subject to rotational noise characterized by $\eta_i^r(t)$ with$< \eta_i^r(t)\eta_j^r(t') >= 2D_r\delta_{ij}\delta(t-t')$. D_r is the rotational frequency.

The self-propelled particles interact with themselves and the passive particles through a repulsive force proportional to the overlap upon collisions.

$$\boldsymbol{F}_{ij} = k(R_i + R_j - r_{ij})\hat{r}_{ij}, \tag{5.3}$$

with $\boldsymbol{r}_{ij} = \boldsymbol{r}_i - \boldsymbol{r}_j = \hat{r}_{ij} r_{ij}$, and k a repulsive force constant. R is the particle radius. The interactions among passive particles can be attractive or repulsive, leading to different behaviors in self-assembly. We discuss each case separately.

5.3 Self-assembly with repulsive interaction

First we consider the simplest case with repulsive interactions among all particles. The form of the interaction is given in Eqn. 5.3. In this case, the parameters controlling the self-assembly is the Péclet number $Pe = \frac{v_0}{D_r R_g}$ of the active particles, where R_g is the radius of the active particle, the packing fractions of the passive ϕ_r and active ϕ_g components, and the repulsive force constant k. We set the mobility $\mu = 1$ unless otherwise noted.

We run simulations with Eqn. 5.1-5.2 tuning the parameters introduced above. Particularly, we study the effect of Péclet number of the active bath on the self-assembly of passive particles. We plot two phase diagrams in the plane $\phi_r - \phi_g$ for small and large Péclet numbers, corresponding to the brownian and ballistic limits, respectively. Notice that the crystallization of passive particles happens at small Péclet number above a threshold packing fraction of $\phi_r \approx 0.5$ with a packing fraction of the active bath as small as $\phi_g \approx 0.1$. In contrast, assembly of passive particles is not observed in the ballistic limit, but the motility induced phase separation (MIPS) occurs above a critical packing fraction of $\phi_g + \phi_r \approx 0.5$. This finding reveals a non-trivial dependence of self-assembly on the properties of the active bath. At small Péclet number, the self-propelled particles behave like a thermal bath by performing brownian motions, therefore the crystallization in this limit is attributed to the depletion interaction induced by the unbalanced

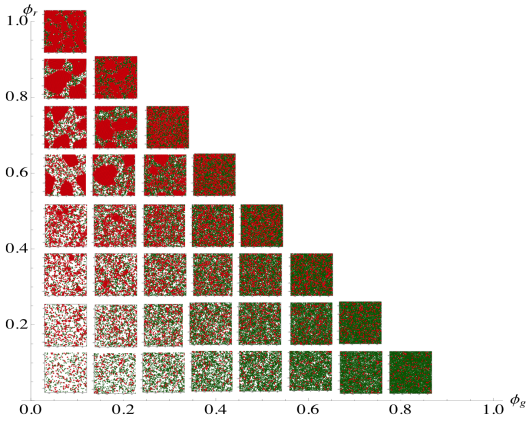

FIGURE 5.1: Active self-assembly in active-passive mixtures with $Pe = 2$. $k = 10$.

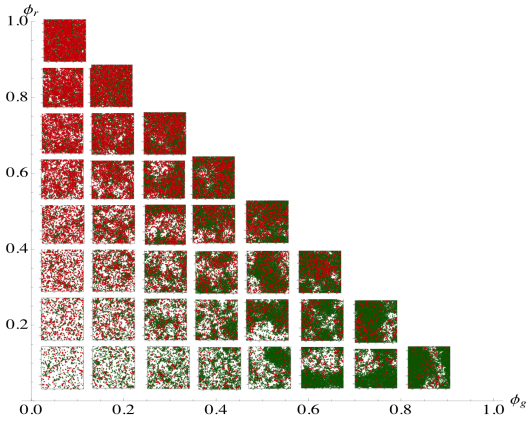

FIGURE 5.2: Active self-assembly in active-passive mixtures with $Pe = 100$. $k = 10$.

.

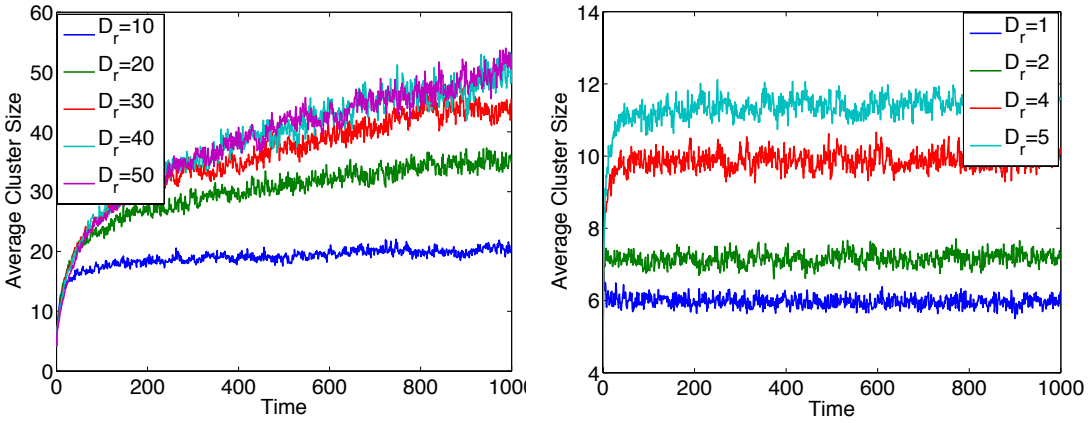

FIGURE 5.3: Average cluster size as a function of time. $\phi_r = 0.3$ and $\phi_g = 0.1$. $k = 100$ and $v_0 = 10$. $R_g = R_r = 1.0$. The cluster rate and average cluster size grows as D_r is decreased, in correspondence with Fig.5.1-5.2

pressures from excluded volume interaction. At large Péclet number, the active bath is highly persistent, and the argument of a depletion interaction generally fails due to the non-Markovian nature of the system. We expect an optimal value of the Péclet number, at which the self-assembly of the passive particles is most efficient due to an enhanced motility of passive particles and a preserved brownian nature of the system.

5.3.1 Mapping to a thermal bath at small Péclet number

To understand the depletion interaction that drives the crystallization of the passive particles in an active bath, we first rewrite Eqn. 5.2 solely in terms of translational dynamics by integrating the angular dynamics as

$$\partial_t \boldsymbol{r}_i^g = \mu \sum_j \boldsymbol{F}_{ij} + \boldsymbol{\xi}_i(t) \ , \tag{5.4}$$

where $\boldsymbol{\xi}_i(t)$ is generally a non-Markovian noise with zero mean and variance

$$< \xi_{i\alpha}(t)\xi_{j\beta}(t') >= \frac{v_0^2}{2} e^{-D_r|t-t'|}\delta_{\alpha\beta}\delta_{ij}. \tag{5.5}$$

For $|t-t'| >> 1/D_r$, it can be approximated as a white noise, with $< \xi_{i\alpha}(t)\xi_{j\beta}(t') >= 2D_t\delta(t-t')\delta_{\alpha\beta}\delta_{ij}$, where $D_t = v_0^2/(2D_r)$. At small Péclet number, this approximation holds for the time scales of the self-assembly. Therefore, the active bath is mapped to a thermal bath in this limit with an effective temperature $k_B T_{eff} = v_0^2/(2D_r\mu)$. In the following sections, we use this thermal equivalent to discuss the depletion interaction that drives the crystallization of passive particles in an active bath in the small Péclet number limit. For simplicity in the notation, we use T for the effective temperature.

5.3.2 The Asakura-Oosawa depletion interaction

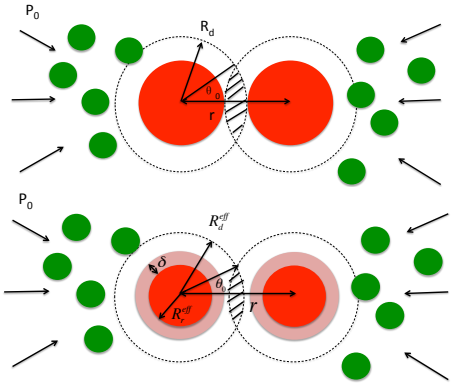

FIGURE 5.4: Diagram of depletion interaction.

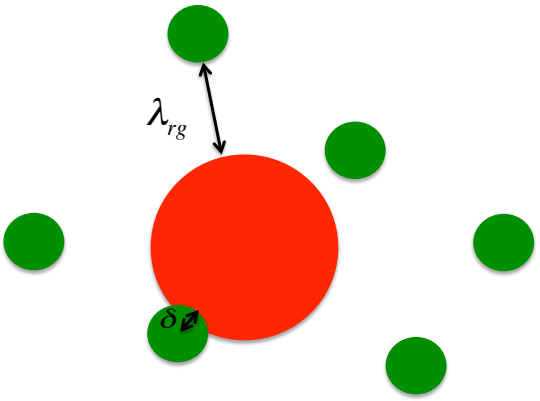

FIGURE 5.5: Diagram of thermal agitation due to collisions.

We start off by calculating the depletion forces between two hard disks in a bath of thermal hard depletants, first studied by Asakura-Oosawa (AO model)[129]. The attractive depletion interaction arises from an imbalanced osmotic pressure due to the excluded volume unaccessible to the depletants (Fig.5.4 top). In our case, the depletion force is simply an integration of the x component of the gas pressure P_0 over the angle extended by the excluded volume.

$$F(r) = -2\int_0^{\theta_b} P_0 R_d cos\theta sin\theta d\theta, \tag{5.6}$$

where $P_0 = n_b k_B T$ with the number density $n_b = \frac{N_g}{V} = \frac{\phi_g}{\pi R_g^2}$.

An explicit integration yields

$$F(r) = -P_0 R_d[1 - (\frac{r}{2R_d})^2], \tag{5.7}$$

where $R_d = R_r + R_g$, from which we can calculate the depletion potential energy

$$U(r) = \int_r^{2R_d} F(r)dr = -P_0 R_d(\frac{4R_d}{3} - r + \frac{r^3}{12R_d^2}). \tag{5.8}$$

The depletion interaction is short-range, non-vanishing for $2R_r < r < 2R_d$. The height of the potential energy, corresponding to the depth of the attractive potential well, is

$$\Delta U = \int_{2R_d}^{2R_r} F(r)dr = 2R_g^2 P_0 \left[1 - \frac{1}{3(1 + R_r/R_g)}\right]. \tag{5.9}$$

Notice that it's linearly proportional to the temperature $k_B T$.

5.3.3 Soft depletion interaction

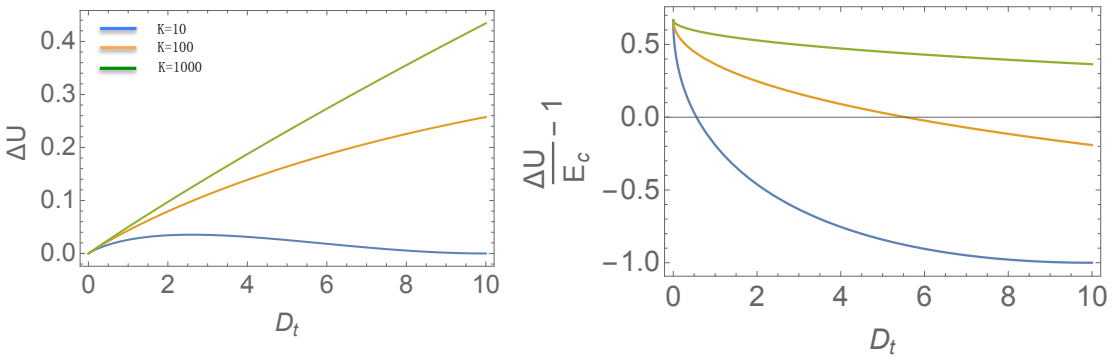

FIGURE 5.6: Left: depth of the attractive well of the soft depletion interaction (Eqn.5.3.3) as a function of thermal diffusivity D_t of the depletants for various stiffness of the depleted particles. At very large stiffness, the potential reduces to the AO potential. Right: coefficient of self-assembly (eqn.5.13) as a function of thermal diffusivity of the depletants. Self-assembly is suppressed for $\Delta U/E_c - 1 < 0$. $\phi_g = 0.1$, $R_r = R_g = 1.0$.

The AO model, based on impenetrable hard particles, does not account for the effect of soft interaction potentials, which bear experimental relevance in suspensions of micelles, star polymers, dendrimers or microgel particles [137–139]. The harmonic potential used in our simulations is also soft, with its strength tunable by the rigidity k. Here, I propose a minimal modification of AO model to account for the soft depletion interaction.

First, we need to quantify the "softness" of the depleted passive particles. The depleted particle has an effective soft shell with thickness δ penetrable by the depletants upon collisions (Fig.5.4 bottom). The shell thickness δ is set by the competition between the thermal energy of depletant particles and the stiffness of the depleted particles. In our model, the stiffness is characterized by a single parameter k, as a spring constant. Therefore δ is determined by balancing the thermal energy and the interaction potential energy

$$\frac{1}{2}k\delta^2 = \frac{1}{2}k_bT, \tag{5.10}$$

which leads to $\delta = \sqrt{\frac{k_bT}{k}}$. The higher the temperature is, the softer the particles are.

Then we treat the depleted particles as hard particles with an effective radius $R_r^{eff} = R_r - \delta$ (Fig.5.4 bottom). Therefore the depletion force (eqn.5.7) and depletion potential (eqn.5.9) is modified by replacing $R_d = R_r + R_g$ with $R_d^{eff} = R_r^{eff} + R_g$. The range of the soft depletion interaction is now $2R_r < r < 2R_d^{eff}$, with the width $\Delta r = 2R_d^{eff} - 2R_r = 2(R_g - \delta)$. The depletion interaction vanishes when $\delta > R_g$.

To obtain the height of the depletion potential for soft particles, we use the modified version of depletion force (eqn.5.7), and integrate it from $2R_d^{eff}$ to $2R_r$:

$$\Delta U = \int_{2R_d^{eff}}^{2R_r} F(r)^{eff} dr = 2P_0 R_g^2 (1 - \frac{R_g}{3R_d^{eff}})$$
$$-2P_0 R_g \frac{2R_r + R_g}{R_d^{eff}} \delta + P_0 \frac{6R_r + 12R_g}{3R_d^{eff}} \delta^2 - P_0 \frac{4}{3R_d^{eff}} \delta^3, \tag{5.11}$$

where $R_d^{eff} = R_r + R_g - \delta$ and $\delta = \sqrt{\frac{k_b T}{k}} = \sqrt{D_t/(\mu k)}$. The dependence of the potential height on temperature of the depletants and stiffness of the depleted particles are plotted in Fig.5.6. Notice that for soft depleted particles, ΔU is non-monotonic that grows with small D_t but decreases as D_t is further increased due to an enhanced δ. It vanishes for $\delta > R_g$. At large stiffness k, the potential reduces to the AO potential that increases linearly with D_t.

5.3.4 Soft-depletion-driven crystallization

The crystallization of passive particles in a brownian active bath is driven by the soft depletion interaction. At the same time, crystals are observed to melt at high effective temperature due to the thermal agitation of the passive particles (depleted particles) from collisions with the active ones (depletants). The competition of the two effects yields the criteria for the self-assembly.

We proceed to calculate the thermal energy injected into the depleted particles through collisions with depletants (Fig.5.5). The injected thermal energy E_c is proportional to the diffusivity of the depleted particles D_t^r. We plot D_t^r as a function of the diffusivity of

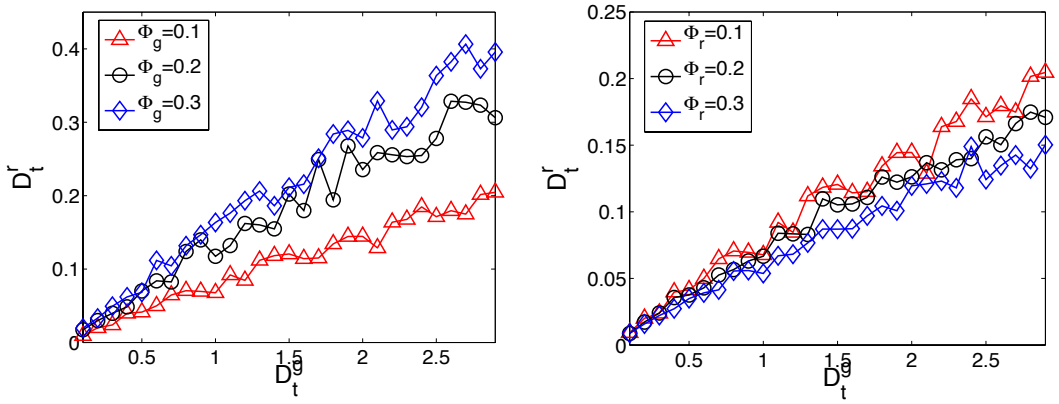

FIGURE 5.7: (color online) Diffusivity of depleted particles D_t^r due to collisions with depletants as a function of D_t^g. Left: $\Phi_r = 0.1$, Right: $\Phi_g = 0.1$.

the depletant D_t^g for different packing fractions ϕ_g and ϕ_r before the system crystallizes in Fig.5.7. We see that for all cases, D_t^r is linearly proportional to D_t^g, but much smaller

in magnitude, suggesting that the depleted particles are effectively "colder" that the depletants, revealing the non-equilirbium nature of the system.

We also notice that D_t^r is proportional to ϕ_g but relatively insensitive to ϕ_r. The above information suggests that D_t^r is determined by ϕ_g and D_t^g. Therefore, we reasonably assume that the thermal energy of the depleted particles are proportional to P_0, the pressure of depletants

$$E_c = c(R_r, R_g)P_0, \tag{5.12}$$

where $c(R_r, R_g)$ is the proportionality constant, which could depend on particle sizes. The criterion for self-assembly or crystallization of the depleted particles is therefore

$$\epsilon = \frac{\Delta U}{E_c} - 1 > 0, \tag{5.13}$$

where ϵ is defined as the coefficient for self-assembly, which we plot in Fig.5.6 as a function of thermal diffusivity D_t of the depletants for various stiffness k. $c(R_r, R_g)$ is assumed to be unity here. Notice that the coefficient generally decreases with the increase of D_t. It is due to the fact that the increase of temperature renders the depleted particles softer, therefore reduces the depletion interaction, while E_c grows with temperature linearly, resulting in a fluidized system. A larger stiffness reduces this effect. This argument is supported by particle simulations shown in Fig.5.8-5.9.

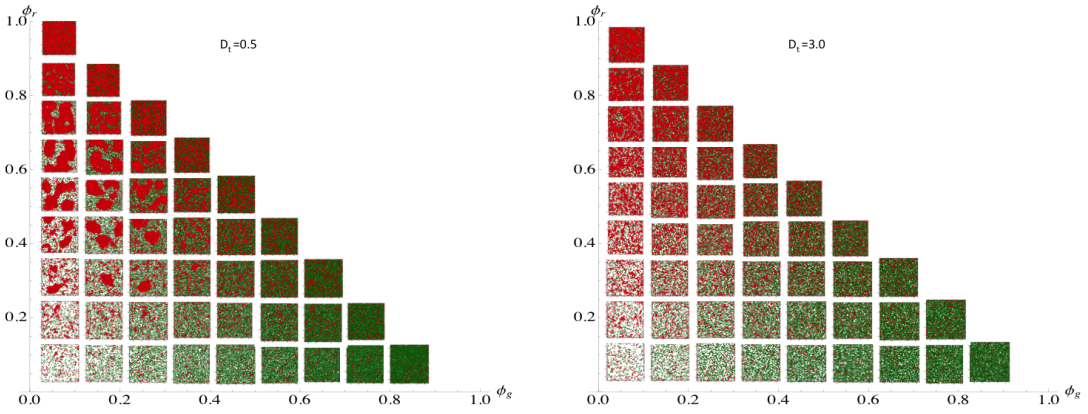

FIGURE 5.8: Simulations for $R_r = 1.4$, $R_g = 1.0$, and $D_t = 0.5$ *and* 3.0. Rigidity $k = 10$ for relatively soft particles. The increase of temperature impedes self-assembly by reducing the strength of depletion interaction.

5.4 Self-assembly with attractive interaction

We have seen in Fig. 5.2 that self-assembly does not occur in a repulsive active-passive mixture at large Péclet number of the active component. However, the motility of the passive particles is greatly enhanced in this limit due to more frequent collisions

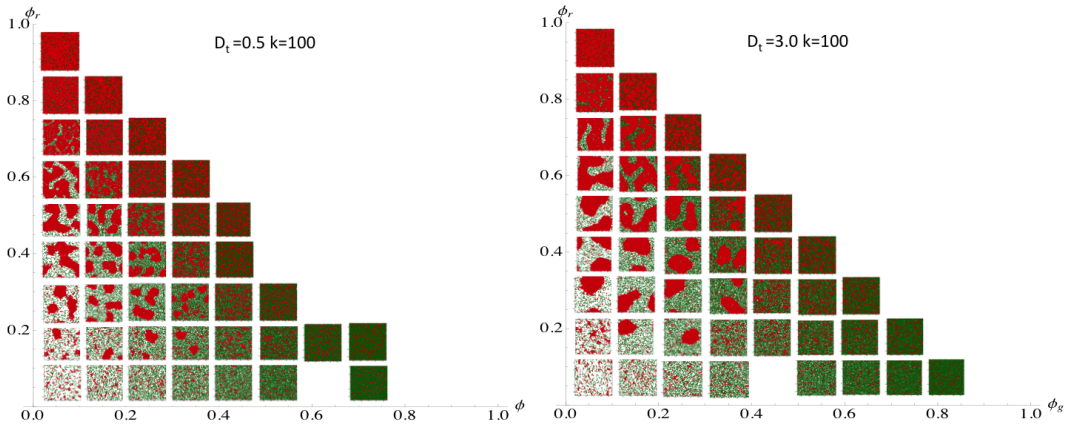

FIGURE 5.9: Simulations for $R_r = 1.4$, $R_g = 1.0$, and $D_t = 0.5$ *and* 3.0. Rigidity $k = 100$ for hard particles. The increase of temperature promotes self-assembly by increasing the dynamics of the depleted particles.

with the active components. In the presence of a non-reversible attractive interaction among passive particles, the enhancement of their motility would ultimately promote self-assembly. Therefore, in the following sections, we assume a short-range attractive interaction among non-contacting passive particles on top of the contacting repulsive interactions. The attractive part is given by

$$\boldsymbol{F}_{ij} = k_a(R_i + R_j - r_{ij})(R_i + R_j + R_a - r_{ij})\hat{r}_{ij}, \tag{5.14}$$

if $R_i + R_j < r_{ij} < R_i + R_j + R_a$, and zero if $r_{ij} > R_i + R_j + R_a$, where R_a is the adhesion range and k_a an attractive force constant. The repulsive part is given by

$$\boldsymbol{F}_{ij} = k(R_i + R_j - r_{ij})\hat{r}_{ij}, \tag{5.15}$$

provided $r_{ij} < R_i + R_j$, same to the repulsive interaction with active particles.

We run particle simulations for the active-passive mixtures using Eqn.5.1-5.2. The adhesion range is chosen to be the radius of the active particle $R_a = R_g = 1.0$, and the adhesion strength is set to be high at $k_{ad} = 4000$ to ensure a non-reversible attraction. The active velocity is $v_0 = 1.0$ and the repulsion constant is $k = 100$. We tune packing fractions of both components and the rotational noise to explore the effects of active bath on the self-assembly of attractive passive particles. The results are summarized in Fig.5.10.

Notice that in contrast to the compact crystals formed in repulsive mixtures, fractal gel-like structures emerge from the self-assembly of passive attractive particles. The cluster rate and average cluster size grow with the decrease of rotational noise, which is the opposite to the repulsive case. This is attributed to the enhancement of motility of

passive particles from collisions with active components and the irreversible attractive interaction that hold the structure together against further collisions. Interestingly, the growth rate of the cluster is linear during the initial stages, and is non-monotonic with respect to the packing fraction of the active particles. There is an optimal packing fraction of the active bath that yield the most efficient assembly from a competition between the enhancement of collision rate and crowding effect.

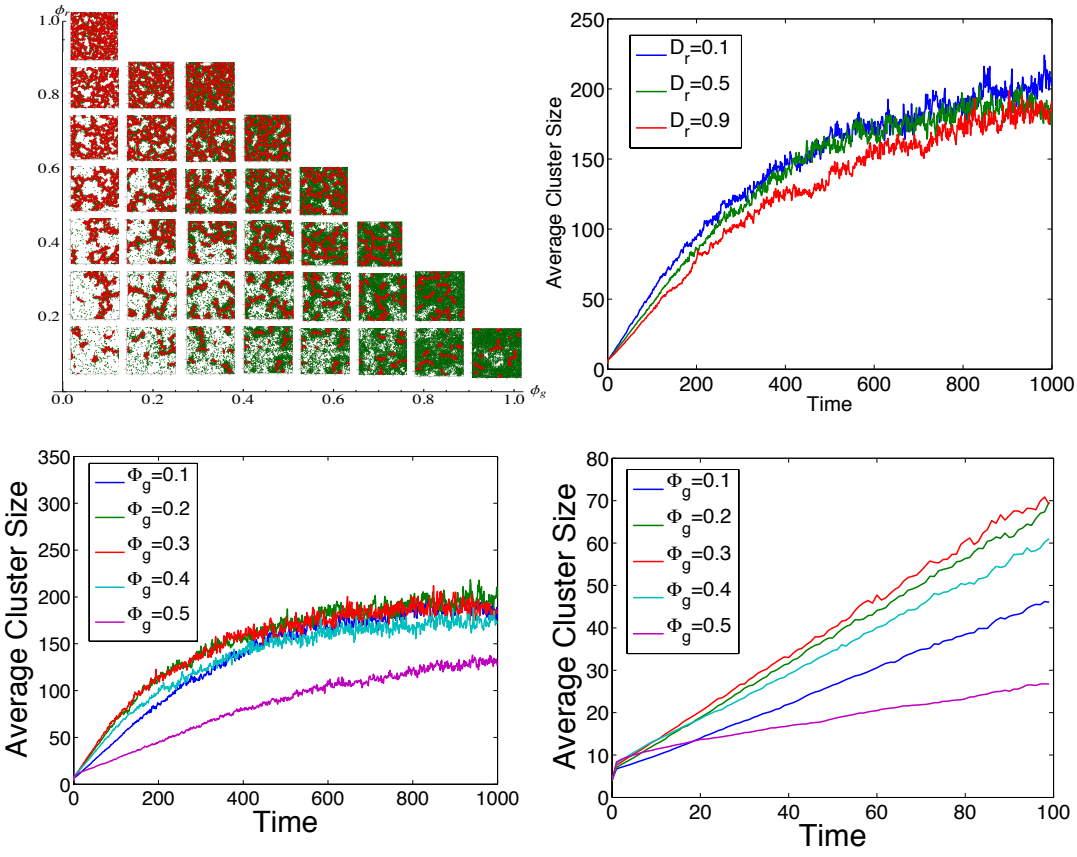

FIGURE 5.10: Active self-assembly in passive-active mixtures. The passive particles interact with a short-ranged attraction, and the active bath constitutes of self-propelled particles. Top left: The snapshots show the fractal structures of passive networks from self-assembly in the plane of ϕ_r and ϕ_g. Top right: average cluster size as a function of time for various rotational noise. Bottom left/right: average cluster size as a function of time for various ϕ_g while $\phi_r = 0.3$.

Bibliography

[1] William Bialek, Andrea Cavagna, Irene Giardina, Thierry Mora, Edmondo Silvestri, Massimiliano Viale, and Aleksandra M. Walczak. Statistical mechanics for natural flocks of birds. *PNAS*, 109(13):4786–4791, January 2012.

[2] Alessandro Attanasi, Andrea Cavagna, Lorenzo Del Castello, Irene Giardina, Tomas S Grigera, Asja Jelić, Stefania Melillo, Leonardo Parisi, Oliver Pohl, Edward Shen, and Massimiliano Viale. Information transfer and behavioural inertia in starling flocks. *Nature Physics*, 10:691–696, July 2014.

[3] Eric Lauga and Thomas R Powers. The hydrodynamics of swimming microorganisms. *Rep. Prog. Phys.*, 72:096601, August 2009.

[4] Michael T. Madigan, John M. Martinko, David Stahl, and David P. Clark. *Brock Biology of Microorganisms*. Benjamin Cummings, 12th edition, 2008.

[5] Elena O. Budrene and Howard C. Berg. Complex patterns formed by motile cells of escherichia coli. *Nature*, 349:630–633, Feb 1991.

[6] D.E. Woodward, R. Tyson, M. R. Myerscough, J. D. Murray, E. O. Budrene, and H.C.Berg. Spatio-temporal patterns generated by salmonella typhimurium. *Biophys. J.*, 68:2181–2189, 1995.

[7] URL http://www.mechanobio.info.

[8] Juha Saarikangas, Hongxia Zhao, and Pekka Lappalainen. Regulation of the actin cytoskeleton-plasma membrane interplay by phosphoinositides. *Physiological Reviews*, 90(1):259–289, January 2010.

[9] S. Whitelam, T. Bretschneider, and N. J. Burroughs. Transformation from spots to waves in a model of actin pattern formation. *Phys. Rev. Lett.*, 102:198103 [4 pages], 2009.

[10] Y. Fily and M. C. Marchetti. Athermal phase separation of self-propelled particles with no alignment. *Phys. Rev. Lett.*, 108:235702 [5pages], 2012.

[11] Jeremie Palacci, Stefano Sacanna, Asher Preska Steinberg, David J. Pine, and Paul M. Chaikin. Living crystals of light-activated colloidal surfers. *Science*, 339 (6122):936–940, Jan. 2013.

[12] Dhananjay T. Tambe, C. Corey Hardin, Thomas E. Angelini, Kavitha Rajendran, Chan Young Park, Xavier Serra-Picamal, Enhua H. Zhou, Muhammad H. Zaman, James P. Butler, David A. Weitz, Jeffrey J. Fredberg, and Xavier Trepat. Collective cell guidance by cooperative intercellular forces. *Nature Materials*, 10: 469–475, May 2011.

[13] M. E. Cates, D. Marenduzzo, I. Pagonabarraga, and J. Tailleur. Arrested phase separation in reproducing bacteria creates a generic route to pattern formation. *PNAS*, 107:11715–11720, 2010.

[14] Frank Schweitzer. *Brownian Agents and Active Particles*. Springer, 2003.

[15] M. C. Marchetti, J. F. Joanny, S. Ramaswamy, T. B. Liverpool, J. Prost, Madan Rao, and R. Aditi Simha. Hydrodynamics of soft active matter. *Rev. Mod. Phys.*, 85(3):1143–1189, Jul 2013.

[16] Shiladitya Banerjee and M. Cristina Marchettib. Instabilities and oscillations in isotropic active gels. *Soft Matter*, 7:463–473, Oct 2011.

[17] X. Yang, D. Marenduzzo, and M. C. Marchetti. Spiral and never-settling patterns in active systems. *Phys. Rev. E*, 89:012711, Jan. 2014.

[18] Dapeng Bi, J. H. Lopez, J. M. Schwarz, and M. Lisa Manning. A density-independent glass transition in biological tissues. *arXiv:1409.0593*, 2015.

[19] Aaron F. Mertz, Yonglu Chea, Shiladitya Banerjee, Jill M. Goldstein, Kathryn A. Rosowski, Stephen F. Revilla, Carien M. Niessen, M. Cristina Marchetti, Eric R. Dufresne, and Valerie Horsley. Cadherin-based intercellular adhesions organize epithelial cell–matrix traction forces. *PNAS*, 110(3):842–847, November 2012.

[20] Tim Sanchez, Daniel T. N. Chen, Stephen J. DeCamp, Michael Heymann, and Zvonimir Dogic. Spontaneous motion in hierarchically assembled active matter. *Nature*, 491:431–434, November 2012.

[21] Luca Giomi, Mark J. Bowick, Xu Ma, and M. Cristina Marchetti. Defect annihilation and proliferation in active nematics. *Phys. Rev. Lett.*, 110:228101, May 2013.

[22] T. Vicsek, A. Czirók, E. Ben-Jacob, I. Cohen, and O. Shochet. Novel type of phase transition in a system of self-driven particles. *Phys. Rev. Lett.*, 75:1226–1229, 1995.

[23] J. Toner and Y. Tu. Long-range order in a two-dimensional dynamical XY model: How birds fly together. *Phys. Rev. Lett.*, 75:4326–4329, 1995.

[24] Andrea Cavagna, Irene Giardina, Tomas S. Grigera, Asja Jelic, Dov Levine, Sriram Ramaswamy, and Massimiliano Viale. Silent flocks. *arXiv:1410.2868*, 2014.

[25] Xingbo Yang and M. Cristina Marchetti. Hydrodynamics of turning flocks. *arXiv:1410.1827*, 2014.

[26] Xavier Trepat, Michael R. Wasserman, Thomas E. Angelini, Emil Millet, David A. Weitz, James P. Butler, and Jeffrey J. Fredberg. Physical forces during collective cell migration. *Nature Physics*, 5:426–430, May 2009.

[27] Jae Hun Kim, Xavier Serra-Picamal, Dhananjay T. Tambe, Enhua H. Zhou, Chan Young Park, Monirosadat Sadati, Jin-Ah Park, Ramaswamy Krishnan, Bomi Gweon, Emil Millet, James P. Butler, Xavier Trepat, and Jeffrey J. Fredberg. Propulsion and navigation within the advancing monolayer sheet. *Nature Materials*, 12:856–863, June 2013.

[28] T. Bretschneider, K. Anderson, M. Ecke, A. Müller-Taubenberger, B. Schroth-Diez, H. C. Ishikawa-Ankerhold, and G. Gerisch. The three-dimensional dynamics of actin waves, a model of cytoskeletal self-organization. *Biophys. J.*, 96:2888–2900, 2009.

[29] V. Schaller, C. Weber, C. Semmrich, E. Frey, and A. R. Bausch. Polar patters of driven filaments. *Nature*, 467:73–77, 2010.

[30] Reza Farhadifar, Jens-Christian Röper, Benoit Aigouy, Suzanne Eaton, and Frank Jülicher. The influence of cell mechanics, cell-cell interactions, and proliferation on epithelial packing. *Current Biology*, 17(24):2095–2104, Dec 2007.

[31] R. Aditi Simha and Sriram Ramaswamy. Hydrodynamic fluctuations and instabilities in ordered suspensions of self-propelled particles. *Phys. Rev. Lett.*, 89:058101, July 2002.

[32] A. P. Berke, L. Turner, H. C. Berg, and E. Lauga. Hydrodynamic attraction of swimming microorganisms by surfaces. *Phys. Rev. Lett.*, 101(038102):038102, 2008.

[33] M. Leoni and T. B. Liverpool. Hydrodynamic synchronization of nonlinear oscillators at low reynolds number. *Phys. Rev. E*, 85:040901(R), April 2012.

[34] Felix C. Keber, Etienne Loiseau, Tim Sanchez, Stephen J. DeCamp, Luca Giomi, Mark J. Bowick, M. Cristina Marchetti, Zvonimir Dogic, and Andreas R. Bausch. Topology and dynamics of active nematic vesicles. *Science*, 345:1135–1139, 2014.

[35] Arshad Kudrolli, Geoffroy Lumay, Dmitri Volfson, and Lev S. Tsimring. Swarming and swirling in self-propelled polar granular rods. *Phys. Rev. Lett.*, 100:058001, Feb 2008. doi: 10.1103/PhysRevLett.100.058001.

[36] G. S. Redner, M. F. Hagan, and A. Baskaran. Structure and dynamics of a phase-separating active colloidal fluid. *Phys. Rev. Lett.*, 110:055701, 2013.

[37] Xingbo Yang, M. Lisa Manning, and M. Cristina Marchetti. Aggregation and segregation of confined active particles. *Soft Matter*, page DOI: 10.1039/c4sm00927d, 2014.

[38] Christoph A. Weber, Yen Ting Lin, Nicolas Biais, and Vasily Zaburdaev. Formation and dissolution of bacterial colonies. *arXiv:1506.01200*, 2015.

[39] Jens Elgeti and Gerhard Gompper. Wall accumulation of self-propelled spheres. *Europhys. Lett.*, 101:48003, Feb 2013.

[40] V. Narayan, S. Ramaswamy, and N. Menon. Long-lived giant number fluctuations in a swarming granular nematic. *Science*, 317:105–108, 2007.

[41] A. Baskaran and M. C. Marchetti. Self-regulation in self-propelled nematic fluids. *Eur. Phys. J. E*, 35:95, July 2012.

[42] G. Duclos, S. Garcia, H. G. Yevick, and P. Silberzan. Perfect nematic order in confined monolayers of spindle-shaped cells. *Soft Matter*, 10:2346–2353, Oct 2014.

[43] Shashi Thutupalli, Mingzhai Sun, Filiz Bunyak, Kannappan Palaniappan, and Joshua. W. Shaevitz. Phase transitions during fruiting body formation in myxococcus xanthus. *arXiv:1410.7230*, 2014.

[44] Marta Fontes and Dale Kaiser. Myxococcus cells respond to elastic forces in their substrate. *PNAS*, 96(14):8052–8057, 1999.

[45] Antoine Bricard, Jean-Baptiste Caussin, Nicolas Desreumaux, Olivier Dauchot, and Denis Bartolo. Emergence of macroscopic directed motion in populations of motile colloids. *Nature*, 503:95–98, November 2013.

[46] H. C. Berg. *E. coli in Motion*. Springer, New York, 2004.

[47] C M Lo, H B Wang, M Dembo, and Y L Wang. Cell movement is guided by the rigidity of the substrate. *Biophys. J.*, 79(1):144–152, 2000.

[48] Ulrich S. Schwarz and Samuel A. Safran. Physics of adherent cells. *Rev. Mod. Phys.*, 85:1327, August 2013.

[49] Ortrud Wartlick, Frank Jülicher, and Marcos Gonzalez-Gaitan. Growth control by a moving morphogen gradient during drosophila eye development. *Development*, 141:1884–1893, May 2014.

[50] Madhav Mani, Sidhartha Goyala, Kenneth D. Irvine, and Boris I. Shraiman. Collective polarization model for gradient sensing via dachsous-fat intercellular signaling. *PNAS*, 110(51):20420–20425, Dec 2013.

[51] Michael Cross and Henry Greenside. *Pattern Formation and Dynamics in Nonequilibrium systems*. Cambridge, 2009.

[52] A. M. Turing. The chemical basis of morphogenesis. *Philosophical Transactions of the Royal Society of London. Series B, Biological Sciences*, 237(641):37–72, Aug 1952.

[53] R Tyson, S R Lubkin, and J D Murray. A minimal mechanism for bacterial pattern formation. *Proc Biol Sci.*, 266(1416):299–304, 1999.

[54] C. W. Reynolds. Flocks, herds, and schools: A distributed behavioral model. *Computer Graphics*, 21(4):25–34, 1987.

[55] Andrea Cavagna, Lorenzo Del Castello, Irene Giardina, Tomas Grigera, Asja Jelic, Stefania Melillo, Thierry Mora, Leonardo Parisi, Edmondo Silvestri, Massimiliano Viale, and Aleksandra M. Walczak. Flocking and turning: a new model for self-organized collective motion. *Journal of Statistical Physics*, doi: 10.1007/s10955-014-1119-3, 2014.

[56] Michael P. Brenner, Leonid S. Levitov, and Elena O. Budrene. Physical mechanisms for chemotactic pattern formation by bacteria. *Biophysical Journal*, 74: 1677–1693, April 1998.

[57] Robert Zwanzig. *Nonequilibrium Statistical Mechanics*. Oxford University Press, 2001.

[58] E. M. Purcell. Life at low reynolds number. *American Journal of Physics*, 45: 3–11, June 1977.

[59] S. C. Takatori, W. Yan, and J. F. Brady. Swim pressure: Stress generation in active matter. *Phys. Rev. Lett.*, 113:028103, July 2014.

[60] A. P. Solon, Y. Fily, A. Baskaran, M. E. Cates, Y. Kafri, M. Kardar, and J. Tailleur. What is the pressure of an active particle fluid. *arXiv:1412.3952*, 2014.

[61] S. C. Takatori and J. F. Brady. Towards a thermodynamics of active matter. *Phys. Rev. E*, 91:032117, March 2015.

[62] T. F. F. Farage, P. Krinninger, and J. M. Brader. Effective interactions in active brownian suspensions. *arXiv:1504.00192*, 2015.

[63] Marco Salm and L M Pismen. Chemical and mechanical signaling in epithelial spreading. *Phys. Biol.*, 9:026009, April 2012.

[64] Zimmermann J, Hayes RL, Basan M, Onuchic JN, Rappel WJ, and Levine H. Intercellular stress reconstitution from traction force data. *Biophys. J.*, 107(3): 548–54, Aug. 2014.

[65] Richard Goodyear and Guy Richardson. Pattern formation in the basilar papilla: Evidence for cell rearrangement. *The Journal of Neuroscience*, 17(16):6289–6301, August 1997.

[66] Luis M. Escudero, Marcus Bischoff, and Matthew Freeman. Myosin ii regulates complex cellular arrangement and epithelial architecture in drosophila. *Developmental Cell*, 13(5):717–729, Nov 2007.

[67] J. D. Murray. *Mathematical Biology vol. II: Spatial Models and Biomedical Applications, 3rd edn.* New York: Springer, 2003.

[68] E. O. Budrene and H. Berg. Dynamics of formation of symmetrical patterns by chemotactic bacteria. *Nature*, 376:49–53, 1995.

[69] T. Butt, T. Mufti, A. Humayun, P. B. Rosenthal, S. Khan, S. Khan, and J. E. Molloy. Myosin motors drive long range alignment of actin filaments. *J. Biol. Chem.*, 285:4964–4974, 2010.

[70] F. Nédélec, T. Surrey, A.C. Maggs, and S. Leibler. Self-organization of microtubules and motors. *Nature*, 389:305–308, 1997.

[71] T. Surrey, F. J. Nédélec, S. Leibler, and E. Karsenti. Physical properties determining self-organization of motors and microtubules. *Science*, 292:1167–1171, 2001.

[72] C. Liu, X. Fu, L. Liu, X. Ren, C. K. L. Chau, S. Li, L. Xiang, H. Zeng, G. Chen, L.-H. Tang, P. lenz, X. Cui, W. Huang, T. Hwa, and J.-D. Huang. Sequential establishment of stripe patterns in an expanding cell population. *Science*, 334: 238–241, 2011.

[73] R. Thar and M. Kühl. Complex pattern formation of marine gradient bacteria explained by a simple computer model. *FEMS Microbiology Letters*, 246:75–79, 2005.

[74] K. Doubrovinski and K. Kruse. Cytoskeletal waves in the absence of molecular motors. *Europhys. Lett.*, 83:18003 [6 pages], 2008.

[75] K. Doubrovinski and K. Kruse. Cell motility resulting from spontaneous polymerization waves. *Phys. Rev. Lett.*, 107:258103 [5 pages], 2011.

[76] A. E. Carlsson. Dendritic actin filament nucleation causes traveling waves and patches. *Phys. Rev. Lett.*, 104:228102 [4 pages], 2010.

[77] M. G. Vicker. Eukaryotic cell locomotion depends on the propagation of self-organized reaction-diffusion waves and oscillations of actin filament assembly. *Exp. Cell Res.*, 275:54–66, 2002.

[78] E. Ben-Jacob, I. Cohen, and H. Levine. Cooperative self-organization of microorganisms. *Adv. Phys.*, 49:395–554, 2000.

[79] M. P. Brenner. Chemotactic patterns without chemotaxis. *Proc. Nat. Acad. Sci. USA*, 107, 2010.

[80] J. Tailleur and M. E. Cates. Statistical mechanics of interacting run-and-tumble bacteria. *Phys. Rev. Lett.*, 100:218103, 2008.

[81] J. Toner. Birth, death and flight: a theory of malthusian flocks. *Phys. Rev. Lett.*, 108:088102, 2012.

[82] Xiongfei Fu, Lei-Han Tang, Chenli Liu, Jian-Dong Huang, Terence Hwa, and Peter Lenz. Stripe formation in bacterial systems with density-suppressed motility. *Phys. Rev. Lett.*, 108:198102 [5 pages], 2012.

[83] J. Toner, Y. Tu, and S. Ramaswamy. Hydrodynamics and phases of flocks. *Ann. Phys.*, 318:170–244, 2005.

[84] M. G. Forest, Q. Wang, and R. Zhou. Kinetic theory and simluations of active polar liquid crystalline polymers. *Soft Matter*, 9:5207–5222, 2013.

[85] F. Farrell, M. C. Marchetti, D. Marenduzzo, and J. Tailleur. Pattern formation in self-propelled particles with density-dependent motility. *Phys. Rev. Lett.*, 105: 248101 [5 pages], 2012.

[86] N. Mittal, E. O. Budrene, M. P. Brenner, and A. van Oudenaarden. Motility of *Escherichia coli* cells in clusters formed by chemotactic aggregates. *Proc. Nat. Acad. Sci. USA*, 100:13259–13263, 2003.

[87] . See Fig. 5 of Ref. [86] and associated discussion.

[88] E. Bertin, M. Droz, and G. Grégoire. Hydrodynamic equations for self-propelled particles: microscopic derivation and stability analysis. *J. Phys. A: Math. Theor.*, 42:445001 (31p), 2009.

[89] S. Mishra, A. Baskaran, and M. Cristina Marchetti. Fluctuations and pattern formation in self-propelled particles. *Phys. Rev. E*, 81:061916, 2010.

[90] . This is estimated as the rotational diffusion of a F-actin cylinder of length 1 μm and thickness 5 nm, in a medium of viscosity $\eta = 1 - 10$ cP, appropriate for water and the cytosol respectively: see e.g. M. Doi and S. F. Edwards, *The Theory of Polymer Dynamics*, Oxford Science Publication, 1986.

[91] P. Romanczuk, M. Bär, W. Ebeling, B. Lindner, and L. Schimansky-Geier. Active brownian particles. *Eur. Phys. J Special Topics*, 202(1):1–162, Mar 2012.

[92] M. Ballerini, N. Cabibbo, R. Candelier, A. Cavagna, E. Cisbani, I. Giardina, V. Lecomte, A. Orlandi, G. Parisi, A. Procaccini, M. Viale, and V. Zdravkovic. Interaction ruling animal collective behavior depends on topological rather than metric distance: Evidence from a field study. *PNAS*, 105(4):1232–1237, January 2008.

[93] B. Szabó, G. J. Szolosi, B. Gonci, Zs. Juranyi, D. Selmeczi, and Tamas Vicsek. Phase transition in the collective migration of tissue cells: Experiment and model. *Phys. Rev. E*, 74(6):061908–, 2006.

[94] Sriram Ramaswamy. The mechanics and statistics of active matter. *Annual Review of Condensed Matter Physics*, 1:323–345, August 2010.

[95] A. Peshkov, E. Bertin, F. Ginelli, and H. Chaté. Boltzmann-ginzburg-landau approach for continuous descriptions of generic vicsek-like models. *Eur. Phys. J Special Topics*, 223(7):1315–1344, June 2014.

[96] E. Braun, Olga Leticia Fuchs, and Salvador Godoy. Hydrodynamic mobilities in a suspension with a fluid with spin. *Chemical Physics Letters*, 265:434–444, 1997.

[97] David S Dean. Langevin equation for the density of a system of interacting langevin processes. *J. Phys. A: Math. Theor.*, 29(24):L613, Dec 1996.

[98] Hannes Risken. *The Fokker-Planck Equation*. Springer-Verlag, second edition, 1988.

[99] J. C. Tsai, Fangfu Ye, Juan Rodriguez, J. P. Gollub, and T. C. Lubensky. A chiral granular gas. *Phys. Rev. Lett.*, 94:214301, May 2005.

[100] Michael Weinberg James T. Hynes, Raymond Kapral. Particle rotation and translation in a fluid with spin. *Physica A*, 87:427–452, June 1977.

[101] Eric Bertin, Michel Droz, and Guillaume Grégoire. Boltzmann and hydrodynamic description for self-propelled particles. *Physical Review E*, 74:022101, 2006.

[102] H. Chaté, F. Ginelli, G. Grégoire, F. Peruani, and F. Raynaud. Modeling collective motion: variations on the vicsek model. *Eur. Phys. J. B*, 64:451–456, 2008.

[103] Arvind Gopinath, Michael F. Hagan, M. Cristina Marchetti, and Aparna Baskaran. Dynamical self-regulation in self-propelled particle flows. *Phys. Rev. E*, 85:061903, June 2012.

[104] S. Ramaswamy, R. A. Simha, and J. Toner. Active nematics on a substrate: Giant number fluctuations and long-time tails. *Europhys. Lett.*, 62:196–202, 2003.

[105] E. Lauga, W. R. DiLuzio, G. M. Whiteside, and H. A. Stone. Swimming in circles: motion of bacteria near solid boundaries. *Biophys. J.*, 90:400–412, 2006.

[106] J. Tailleur and M. E. Cates. Sedimentation, trapping, and rectification of dilute bacteria. *Europhys. Lett.*, 86:60002, June 2009.

[107] J. Elgeti and G. Gompper. Self-propelled rods near surfaces. *Europhys. Lett.*, 85: 38002 (6pp), 2009.

[108] Elöd Méhes, Enys Mones, Valéria Németh, and Tamás Vicsek. Collective motion of cells mediates segregation and pattern formation in co-cultures. *PloS one*, 7(2): p.e31711, 2012.

[109] Julio M. Belmonte, Gilberto L. Thomas, Leonardo G. Brunnet, Rita M. C. de Almeida, and Hugues Chaté. Self-propelled particle model for cell-sorting phenomena. *Phys. Rev. Lett.*, 100:248702, Jun 2008. doi: 10.1103/PhysRevLett.100.248702.

[110] Samuel R. McCandlish, Aparna Baskaran, and Michael F. Hagan. Spontaneous segregation of self-propelled particles with different motilities. *Soft Matter*, 8: 2527–2534, 2012. doi: 10.1039/C2SM06960A.

[111] Aleksandar Donev, Salvatore Torquato, Frank H. Stillinger, and Robert Connelly. Jamming in hard sphere and disk packings. *Journal of Applied Physics*, 95:989, 2004.

[112] S. A. Mallory, A. Šarić, C. Valeriani, and A. Cacciuto. Anomalous thermomechanical properties of a self-propelled colloidal fluid. *Phys. Rev. E*, 89:052303, 2014.

[113] D.Ray, C.Reichhardt, and C.J.Olson Reichhardt. Casimir effect in active matter systems. *arXiv:1402.6372*, Feb 2014.

[114] MS. Steinberg. Reconstruction of tissues by dissociated cells. some morphogenetic tissue movements and the sorting out of embryonic cells may have a common explanation. *Science*, 141(3579):401–8, Aug 1963.

[115] Albert K. Harris. Is cell sorting caused by differences in the work of intercellular adhesion? a critique of the steinberg hypothesis is cell sorting caused by differences in the work of intercellular adhesion? a critique of the steinberg hypothesis is cell sorting caused by differences in the work of intercellular adhesion? a critique of the steinberg hypothesis is cell sorting caused by differences in the work of intercellular adhesion? a critique of the steinberg hypothesis is cell sorting caused by differences in the work of intercellular adhesion? a critique of the steinberg hypothesis. *J Theor Biol*, 61(2):267–285, Sep 1976.

[116] R.A. Foty and MS. Steinberg. The differential adhesion hypothesis: a direct evaluation. *Dev Biol*, 278(1):255–63, 2005.

[117] M. Krieg, Y. Arboleda-Estudillo, P.-H. Puech, J. Käfer, F. Graner, D. J. Müller, and C.-P. Heisenberg. Tensile forces govern germ-layer organization in zebrafish. *Nature Cell Biol.*, 10:429–436, March 2008.

[118] M. Lisa Manning, Ramsey A. Foty, Malcolm S. Steinberg, and Eva-Maria Schoetz. Coaction of intercellular adhesion and cortical tension specifies tissue surface tension. *PNAS*, 107(28):12517–12522, June 2010.

[119] Lidia Ceriani and Paolo Verme. *The origins of the Gini index: extracts from Variabilità e Mutabilità (1912) by Corrado Gini*, volume 10. Springer US, 2012.

[120] C. Reichhardt and C.J. Olson Reichhardt. Active matter transport and jamming on disordered landscapes. *arXiv:1402.3260*, Feb 2014.

[121] Anthony Rosato, Katherine J. Strandburg, Friedrich Prinz, and Robert H. Swendsen. Why the brazil nuts are on top: Size segregation of particulate matter by shaking. *Phys. Rev. Lett.*, 58:1038–1040, 1987.

[122] James B. Knight, H. M. Jaeger, and Sidney R. Nagel. Vibration-induced size separation in granular media: The convection connection. *Phys. Rev. Lett.*, 70: 3728–3731, 1993.

[123] J. H. Irving and John G. Kirkwood. The statistical mechanical theory of transport processes. *J. Chem. Phys.*, 18:6, 1949.

[124] Yaouen Fily, Silke Henkes, and M. Cristina Marchetti. Freezing and phase separation of self-propelled disks. *Soft Matter*, 10:2132–2140, 2014.

[125] M. E. Cates. Diffusive transport without detailed balance in motile bacteria: does microbiology need statistical physics? *Rep. Prog. Phys.*, 75:042601 (14pp), 2012.

[126] B. M. Mognetti, A. Šarić, S. Angioletti-Uberti, A. Cacciuto, C. Valeriani, and D. Frenkel. Living clusters and crystals from low-density suspensions of active colloids. *Phys. Rev. Lett.*, 111(24):245702, Dec 2013.

[127] Yaouen Fily, Aparna Baskaran, and Michael F. Hagan. Dynamics of self-propelled particles under strong confinement. *arXiv:1402.5583*, Feb 2014.

[128] Lorenzo Di Michele, Francesco Varrato, Jurij Kotar, Simon H. Nathan, Giuseppe Foffi, and Erika Eiser. Multistep kinetic self-assembly of dna-coated colloids. *Nature Communications*, 4(2007), June 2013.

[129] Sho Asakura and Fumio Oosawa. On interaction between two bodies immersed in a solution of macromolecules. *The Journal of Chemical Physics*, 22(1255), 1954.

[130] Giorgio Cinacchi, Yuri Martínez-Ratón, Luis Mederos, Guillermo Navascués, Alessandro Tani, and Enrique Velasco. Large attractive depletion interactions in soft repulsive–sphere binary mixtures. *The Journal of Chemical Physics*, 127 (214501), 2007.

[131] Zorana Zeravcic, Vinothan N. Manoharan, and Michael P. Brenner. Size limits of self-assembled colloidal structures made using specific interactions. *PNAS*, 111 (45):15918–15923, 2014.

[132] Gabriel S. Redner, Aparna Baskaran, and Michael F. Hagan. Reentrant phase behavior in active colloids with attraction. *Phys. Rev. E*, 88:012305, July 2013.

[133] Joakim Stenhammar, Raphael Wittkowski, Davide Marenduzzo, and Michael E. Cates. Activity-induced phase separation and self-assembly in mixtures of active and passive particles. *Phys. Rev. Lett.*, 114:018301, Jan. 2015.

[134] Ran Ni, Martien A. Cohen Stuart, Marjolein Dijkstra, and Peter G. Bolhuis. Crystallizing hard-sphere glasses by doping with active particles. *Soft Matter*, 10: 6609–6613, 2014.

[135] Harder J, Mallory SA, Tung C, Valeriani C, and Cacciuto A. The role of particle shape in active depletion. *J. Chem. Phys.*, 141(19):194901, 2014.

[136] Chantal Valeriani, Martin Li, John Novosel, Jochen Arlt, and Davide Marenduzzo. Colloids in a bacterial bath: simulations and experiments. *Soft Matter*, 7:5228, April 2011.

[137] Manuel Camargo and Christos N. Likos. Unusual features of depletion interactions in soft polymer-based colloids mixed with linear homopolymers. *Phys. Rev. Lett.*, 104:078301, 2010.

[138] BUY: 28.00$RENT$:4.00 Tyler N. Shendruk, Martin Bertrand, James L. Harden, Gary W. Slater, and Hendrick W. de Haan. Coarse-grained molecular dynamics simulations of depletion-induced interactions for soft matter systems. *J. Chem. Phys.*, 141:244910, 2014.

[139] Lorenzo Rovigatti, Nicoletta Gnan, Alberto Parolad, and Emanuela Zaccarellicb. How soft repulsion enhances the depletion mechanism. *Soft Matter*, 11:692–700, 2015.

Xingbo Yang

Department of Physics
Syracuse University
Syracuse, NY 13244 U.S.A.

Phone: 315-560-3751
Email: xyang14@syr.edu
URL: http://asnews.syr.edu/newsevents_2014/releases/Xingbo_Yang_Profile.html

Education

2010-2015 Ph.D. in Physics, Syracuse University
2007-2010 B.A. in Journalism, Fudan University
2006-2007 Undergraduate in Materials Science, Fudan University

Research Experiences

2010-2015 Ph.D. Candidate in Theoretical Soft Condensed Matter Physics, Syracuse University
Supervisor: M. Cristina Marchetti
Topics: Modeling of Collective Phenomena in Soft Active Matter

2012-2015 Research Associate at Soft Interfaces IGERT, Syracuse University
Topics: Bacterial Mechanosensing of Compressed Hydrogels

Jan-May 2014 Research Affiliate at Kavli Institute for Theoretical Physics, University of California, Santa Barbara
Topics: Active Matter: Cytoskeleton, Cells, Tissues and Flocks

Teaching Employment

Summer 2011 Lecturer of Electromagnetism for undergraduate, Syracuse University
Fall 2010/2012 Lab TA of Major Concepts of Physics for undergraduate, Syracuse University
Spring 2011/Fall 2013 Recitation TA of Classical Mechanics for undergraduate, Syracuse University

Mentoring

2014 Trained a graduate student to perform active molecular dynamics simulation

Fellowships and Grants

Jan-May 2014 Affiliate grant from Kavli Institute for Theoretical Physics, University of California, Santa Barbara

Invited and Contributed Talks, Posters

March 2015 X.Yang, M. Cristina Marchetti, "Hydrodynamics of Turning Flocks", contributed talk at APS March meeting, San Antonio, TX

Dec 2014 X. Yang, "Modeling of Active Systems: from particle-based simulation to continuum theory", invited talk at Max Plank Institute for Physics of Complex Systems, Dresden, Germany

Dec 2014 X.Yang, M. Cristina Marchetti, "Hydrodynamics of Turning Flocks", soundbite at New York Complex Matter Workshop, Ithaca, NY

June 2014 X. Yang, M. Lisa Manning, M. Cristina Marchetti, "Aggregation and segregation of confined active particles", oral presentation at "88th Colloid and Surface Science Symposium", Philadelphia, PA

Mar 2014 X. Yang, M. Lisa Manning, M. Cristina Marchetti, "Aggregation and Segregation of Confined Active Particles", contributed talk at APS March meeting, Denver, CO

Feb 2014 X. Yang, M. Lisa Manning, M. Cristina Marchetti, "Aggregation and segregation of confined self-propelled particles", contributed talk at "KITP conference: Active Processes in Living and Nonliving Matter", Goleta, CA

August 2013 X. Yang, M. Lisa Manning, M. Cristina Marchetti, "Aggregation and Segregation of Confined Active Particles", poster at "Gordon Research Conference: Soft Condensed Matter Physics", New London, NH

Mar 2013 X. Yang, Davide Marenduzzo, M. Cristina Marchetti, "Pattern Formation in Growing Polar Bacteria", contributed talk at APS March meeting, Baltimore, MD

July 2012 X. Yang, Davide Marenduzzo, M. Cristina Marchetti, "Pattern Formation in Growing Polar Bacteria", poster at "Boulder school for condensed matter and materials physics: polymers in soft and biological matter", Boulder, CO

Schools and Workshops

August 2015 Santa Barbara Advanced School of Quantitative Biology: The Course of Cellular Evolution, Santa Barbara, CA

Jul-Aug 2012 Boulder school for condensed matter and materials physics: polymers in soft and biological matter, Boulder, CO

Dec 2011 12th New York Complex Matter Workshop, Ithaca, NY

Service to the profession

August 2013 Co-chair of "Science Session 1: Squishy Materials and Biology" at Gordon Research Seminar on Soft Condensed Matter Physics, New London, NH

2013-2014 Referee of Europhysics Letters and Journal of Statistical Physics

Publications

2014 X. Yang and M. C. Marchetti, "Hydrodynamic of turning flocks", arXiv:1410.1827

2014 Xingbo Yang, M. Lisa Manning, M. Cristina Marchetti, "Aggregation and segregation of confined active particles", Soft Matter, 10, 6477-6484(2014)

2014 X. Yang, D. Marenduzzo, and M. C. Marchetti, "Spiral and never-settling patterns in active systems", Physical Review E, 89, 012711(2014)

Computational skills

Programming languages: C, C++, Cuda, Python, Javascript
Computational softwares: Mathematica, Matlab